Technische Universität München
Institut für Energietechnik

Lehrstuhl für Thermodynamik

Modeling Turbulent Combustion and CO Emissions in Partially-Premixed Conditions Considering Flame Stretch and Heat Loss

Noah Eugen Klarmann

Vollständiger Abdruck der von der Fakultät für Maschinenwesen der Technischen Universität München zur Erlangung des akademischen Grades eines

DOKTOR – INGENIEURS

genehmigten Dissertation.

Vorsitzender:

Prof. Carlo L. Bottasso, Ph.D.

Prüfer der Dissertation:

1. Prof. Dr.-Ing. Thomas Sattelmayer
2. Prof. Antonio Andreini, Ph.D.
   University of Florence, Italy

Die Dissertation wurde am 06.03.2019 bei der Technischen Universität München eingereicht und durch die Fakultät für Maschinenwesen am 05.06.2019 angenommen.

Vorwort

Die vorliegende Arbeit entstand während meiner Tätigkeit am Lehrstuhl für Thermodynamik der Technischen Universität München. Sie wurde vom Bundesministerium für Wirtschaft und Energie (BMWi) sowie von General Electric im Rahmen des deutschen Forschungsverbundes AG Turbo gefördert.

Meinem Doktorvater Herrn Prof. Dr.-Ing. Thomas Sattelmayer bin ich zu großem Dank für die wissenschaftliche Betreuung dieser Arbeit verpflichtet. Die Zusammenarbeit mit ihm hat mich stets inspiriert und maßgeblich die Qualität dieser Arbeit geprägt. Ich bedanke mich auch für die mir gestatteten Freiräume, in denen ich mich während der Promotion weiterentwickeln konnte.

Herrn Prof. Dr. Antonio Andreini danke ich für die Übernahme des Koreferates und Herrn Prof. Dr. Carlo Botasso für den Prüfungsvorsitz.

Auch danke ich Herrn Dr. sc. Benjamin Zoller, welcher dieses Projekt seitens der Industrie betreute. Die fachlichen Diskussionen mit ihm haben sehr zum Gelingen dieser Arbeit beigetragen.

Ich danke allen Studenten, die mich während der Promotion begleitet haben. Besonders hervorheben möchte ich dabei Christoph Wieland, der mich über einen langen Zeitraum sowohl in der Numerik als auch bei den Experimenten tatkräftig unterstützte.

Ich möchte mich bei allen ehemaligen Kollegen für die tolle Atmosphäre am Lehrstuhl bedanken. Hierbei möchte ich Frau Helga Bassett und Frau Sigrid Schulz-Reichwald hervorheben, die mich bei sämtlichen organisatorischen Angelegenheiten geduldig unterstützten. Weiterhin bedanke ich mich bei den Werkstätten für die Fertigung des Prüfstandes sowie allen Kollegen, die mir während der experimentellen Phase mit ihrer Fachkenntnis zur Seite standen: Nicolai Stadlmair, Georg Fink, Stephan Lellek und Michael Betz.

Aus manchen Mitstreitern wurden wertvolle Freunde: Tobias Hummel, Frederik Berger, Ehsan Arabian, Michael Hertweck, Nicolai Stadlmair und Georg Fink. Vielen Dank für die zahlreichen schönen Momente in den letzten Jahren. Ich hoffe wir bleiben noch lange in Kontakt.

Liebe Jelena, Deine Unterstützung in der finalen Phase war beispiellos. Du hast einen großen Beitrag an der erfolgreichen Fertigstellung dieser Arbeit und dafür danke ich Dir von ganzem Herzen.

Liebe Familie, ich bin stolz, mit Euch ein so großartiges Umfeld zu haben. Ihr habt mir über all die Jahre Eure bedingungslose Unterstützung zukommen lassen. Euch habe ich alles zu verdanken.

München, im Juli 2019 Noah Klarmann

Abstract

This study investigates combustion and CO emissions in cold conditions that occur in gas turbines operating at part load conditions. Moreover, the key research findings are used to develop a modeling strategy that is able to predict heat release and CO distributions. The models seek to support the development of new flexible designs and concepts for modern gas turbines that meet the requirements of the imminent new energy age. Combustion is described on the basis of flamelet generated manifolds. Important effects like flame stretch and heat loss are efficiently considered by a novel approach. Validation is performed by comparing the numerically predicted heat release with experimental OH^*. Furthermore, a new CO methodology is proposed. CO is derived from flamelets within the turbulent flame brush. As the flamelet theory is not able to describe the burnout chemistry downstream of the turbulent flame brush, a model is introduced that predicts the transition from the theory of infinitely thin reaction zones to kinetically limited burnouts. Experiments have been conducted in which spatially resolved CO is obtained in order to validate the proposed methodology. Moreover, the validation in two different multi-burner cases is presented to demonstrate the model's capability of predicting CO in various fuel-staging scenarios. In addition, the CO modeling strategy is applied to a novel combustor concept to show basic mechanisms that are relevant in the context of this work.

Kurzfassung

Diese Arbeit untersucht den Verbrennungsvorgang und die damit verbundenen CO-Emissionen in Gasturbinenbrennkammern bei Teillast. In diesem Zusammenhang wird eine neue Modellierungsstrategie präsentiert, mit der sich die räumlichen Verteilungen von Wärmefreisetzung und CO vorhersagen lassen. Diese Modelle können für die Entwicklung moderner Brennkammern und Betriebskonzepte für Gasturbinen eingesetzt werden, die den Anforderungen des bevorstehenden neuen Energiezeitalters entsprechen. Der Verbrennungsvorgang ist auf Basis von eindimensionalen Flammenrechnungen mit detaillierter Chemie unter Berücksichtigung von Flammenstreckung und Wärmeverlusten modelliert. Weiterhin erfolgt die Validierung des Wärmefreisetzungsmodells mit experimentellen OH^*-Verteilungen. Das Verbrennungsmodell kann zudem die CO-Verteilung innerhalb der turbulenten Flammenbürste beschreiben. Da die eindimensionalen Flammen stromab der Wärmefreisetzungszone an Gültigkeit verlieren, wird ein neues Vorgehen für die Beschreibung der chemischen Quellterme im CO-Ausbrand vorgestellt. Atmosphärische Experimente wurden durchgeführt, um lokal aufgelöstes CO zu messen. Neben der Validierung von globalen Emissionen lassen sich so auch die einzelnen Untermodelle auf Gültigkeit überprüfen. Darüber hinaus wird die Validierung von globalem CO in zwei verschiedenen Mehrbrenneranordnungen vorgestellt. Diese Studie demonstriert die Fähigkeit der Modelle CO in verschiedenen Szenarien der Brennstoffstufung vorherzusagen. Am Ende dieser Arbeit werden die Modelle auf ein neuartiges Brennerkonzept angewandt.

Contents

List of Figures

List of Tables

Nomenclature

Latin Characters

A	$[\mathrm{m}^2]$	Surface
A_{freq}	$[(\mathrm{m}^3/\mathrm{kmol})^{i-1}/\mathrm{Ks}]$	Pre-exponential factor
b	[-]	Stoichiometric mass ratio of oxidizer to fuel
$\mathcal{C}$	[-]	Number of atoms
C	[-]	Generic model constant
c	[-]	Reaction progress
c_p	$[\mathrm{kJ}/\mathrm{kgK}]$	Heat capacity
D	$[\mathrm{m}^2/\mathrm{s}]$	Diffusion coefficient
d	[m]	Diameter
E	$[\mathrm{m}^3/\mathrm{s}^2]$	Turbulent kinetic energy in wave number space
E_a	$[\mathrm{kJ}/\mathrm{kmol}]$	Activation energy
F	$[\mathrm{m}/\mathrm{s}^2]$	Force
f	[-]	Mixture fraction
h	$[\mathrm{kJ}/\mathrm{kg}]$	Enthalpy (sum of sensible and chemical enthalpy)
Δh_{form}	$[\mathrm{kJ}/\mathrm{kg}]$	Enthalpy of formation
k	$[\mathrm{m}^2/\mathrm{s}^2]$	Turbulent kinetic energy
k_{arr}	$[(\mathrm{m}^3/\mathrm{kmol})^{i-1}/\mathrm{s}]$	Rate constant
l	[m]	Length
$\mathcal{M}$	[-]	Number of species
m	[kg]	Mass
$m_{\kappa,\psi}$	[-]	Proportionality exponent
$\dot{m}$	$[\mathrm{kg}/\mathrm{s}]$	Mass flow rate
$\mathcal{N}$	[-]	Number of species
n	[-]	Surface orientation factor
P_k	$[\mathrm{kg}/\mathrm{ms}^3]$	Source term for turbulent kinetic energy
p	$[\mathrm{kg}/\mathrm{ms}^2]$	Pressure
q	$[\mathrm{kJ}/\mathrm{m}^2\mathrm{s}]$	Diffusive flux of enthalpy
$\mathcal{R}$	[-]	Number of reactions

R	[kJ/kmolK]	Ideal gas constant
r	[m]	Radius
s	[m/s]	Flame speed
T	[K]	Temperature
t	[s]	Time
u	[m/s]	Velocity
V	[m/s]	Diffusion velocity
W	[kg/kmol]	Molecular mass
w	[1/m]	Wave number
x, y, z	[m]	Spatial coordinates
Y	[-]	Mass fraction

Greek Characters

α	[W/m²K]	Heat transfer coefficient
β	[-]	Temperature exponent
$\Gamma_{\psi,\kappa}$	[-]	Correction factor
γ	[-]	Stoichiometric coefficient
ϵ	[m²/s³]	Eddy dissipation rate
ζ	[-]	Quenching criterion
η	[m]	Kolmogorov length scale
θ	[-]	Generic variable
κ	[1/s]	Flame stretch
λ	[W/mK]	Thermal conductivity
μ	[kg/ms]	Dynamic viscosity
ν	[m²/s]	Kinematic viscosity
ρ	[kg/m³]	Density
$\dot{\varsigma}$	[kmol/m³s]	Molecular source term
σ	[kg/ms²]	Viscous tensor
τ	[s]	Time scale
ϕ	[-]	Equivalence ratio
ψ	[kJ/kg]	Heat loss
$\dot{\omega}$	[kg/m³s]	Mass source term
$\dot{\omega}_T$	[kgK/m³s]	Temperature source term
$\dot{\omega}_h$	[kJ/m³s]	Enthalpy source term

Superscripts

0	Reference conditions
$*$	Stretched and/or non-adiabatic
$\hat{}$	Normalized
$\bar{}$	Ensemble mean
$'$	Fluctuations regarding ensemble mean
$\tilde{}$	Favre mean
$''$	Fluctuations regarding Favre mean

Subscripts

∞	Ambient conditions
$0/1$	Mixture fraction of zero/unity
15	Normalized to 15% dioxygen
ad	Adiabatic
an	Annulus
b	Burnt
$burner$	Burner
c	Fuel consumption
ch	Chemical
cr	Creation
$crit$	Critical
$curv$	Curvature
d	Displacement
$diff$	Diffusion
dry	Does not contain water
$eddy$	Turbulent vortex
eq	Equilibrium
f	Flame
$fuel$	Fuel
fit	Curve fitted
for/rev	Forward/reverse
gen	Generic
ign	Ignition
int	Integral

$iter$	Iteration
l	Laminar
lbo	Lean blowout
max	Maximum
$model$	Modeled
ox	Oxidation
$oxid$	Oxidizer
pri/sec	Primary/secondary
q	Quenched
r	Reactor
$sens$	Sensible
st	Strain
sto	Stoichiometric
t	Turbulent
tfb	Turbulent flame brush
th	Thermal
$trans$	Transition
u	Unburnt
w	Wrinkling
$wall$	Wall

Control Indices

i, j, k	Spatial indices
r	Reaction index
s, t	Species indices

Functions

$\mathcal{I}$	[-]	Intermittent Turbulence Net Flame Stretch
$\mathcal{P}$	[-]	Probability Density Function

Dimensionless Numbers

Da	Damköhler number
Da_t	Turbulent Damköhler number
Ka_t	Turbulent Karlovitz number
Re	Reynolds number
Sc_t	Turbulent Schmidt number

Abbreviation

CFD	Computational Fluid Dynamics
DNS	Direct Numerical Simulation
EBU	Eddy Break Up
EDM	Eddy Dissipation Model
FGM	Flamelet Generated Manifold
FR	Finite Rate
ILDM	Intrinsic Low-Dimensional Manifolds
ITNFS	Intermittent Turbulence Net Flame Stretch
LES	Large Eddy Simulation
ODE	Ordinary Differential Equations
PDF	Probability Density Function
RANS	Reynolds-Averaged Navier-Stokes
RMS	Root Mean Square
TFC	Turbulent Flame Speed Closure

Molecules

CH_4	Carbon tetrahydride (methane)
CO	Carbon monoxide
CO_2	Carbon dioxide
H	Molecular hydrogen
H_2	Dihydrogen
H_2O	Dihydrogen monoxide (water)
HO_2	Dioxidanyl (hydroperoxyl)
N_2	Dinitrogen
N_2O	Dinitrogen monoxide (nitrous oxide)

NO_x	Nitrogen oxides
O	Molecular oxygen
O_2	Dioxygen
OH	Oxidanyl (hydroxyl)

Miscellenous

$\langle\ \rangle$	[-]	Surface averaging
$[\ ]$	$[\mathrm{kmol}/\mathrm{m}^3]$	Molecular concentration
$\aleph$	[-]	Placeholder for chemical symbols
δ	[-]	Kronecker delta

1 Introduction

Human interventions in natural processes have never been more far-reaching than today. The industrialization caused a 40 % increase in carbon dioxide (CO_2), leading to destructive consequences for the ecological balance of the planet according to the INTERGOVERNMENTAL PANEL ON CLIMATE CHANGE [1]. Concentrations of greenhouse gases such as CO_2, methane (CH_4), and nitrous oxide (N_2O) have never been higher in the last million years. The oceans absorbed about 30 % of the anthropogenic CO_2 leading to an ongoing process of seawater acidification that has a drastic impact on marine organisms [1]. Furthermore, the greenhouse effect causes the earth's surface, atmosphere, and oceans to heat up. Consequently, each of the last three decades has been warmer than the previous one as well as warmer than all other decades since 1850 [1]. In addition, the last thirty years have been the hottest in the Northern Hemisphere in at least 1400 years [1]. This rise in temperature leads to multiple side effects that have never been observed in the last millennium. Droughts, storms, and melting of the polar ice caps are just a few of the numerous negative impacts of global warming.

The world's energy demand is predicted to increase approximately by about 30 % between today and 2040 according to the INTERNATIONAL ENERGY AGENCY [2, 3] and BRITISH PETROLEUM [4]. A major societal challenge of the future is to cover the increasing energy demand while to simultaneously reduce greenhouse gases. For this purpose, international conventions have been imposed, notably the PARIS AGREEMENT [5] or the KYOTO PROTOCOL [6]. Due to the global trend of electrification, 70-80 % of the primary energy increase is used for the production of power [2, 4]. It should be noted that energy demand is not only a function of the exponential population growth, but also correlates with the improvement in efficiency, which reduces the energy per human consumption rate. The energy mix for power generation is expected to change drastically in the

near future. Conventional power sources are anticipated to lose relevance due to a significant increase in renewables, but retain its major role in the overall energy mix. Besides advantages for the environment, renewables will also become the best economical choice for most countries. Thus, two thirds of the global investment for power plants is expected to be spent on renewable power production [3]. Furthermore, renewables will account for 40 % of the total increase in primary energy sources [3, 4]. While the proportion of oil and coal is predicted to decline, the use of natural gas is anticipated to increase significantly by 45 % between today and 2040 [3]. In order to meet the increased demand for natural gas, new exploration and production techniques need to be developed [2]. What causes natural gas to gain importance in the next decades? There are numerous obvious reasons such as efficiency and environmental legislations like emission limits[1]. A further reason is that power production by gas turbines plays a key role in the process of implementing a large share of renewables. Especially small- to mid-sized gas turbines are able to quickly change their load as mentioned by Wiedermann [7]. Volatilities of renewable power production cause fluctuations that need to be compensated in order to guarantee a stable public grid frequency. Besides the compensation by changing the load in terms of secondary control, gas turbines also act as primary control systems[2]. Due to these properties, gas turbines are the ideal counterpart to renewables and are thus a sustainable technology as mentioned by Sinn [9]. In order to prepare gas turbines for the challenges of tomorrow, reduction of emissions, increase of flexibility, efficiency, and reliability is of high technical relevance and the subject of numerous research projects nowadays.

Germany has a key role in the new energy age as it aims to become the technology leader in renewable power production to combat climate change. In addition, Germany has the highest capacity and largest market for natural gas in the EUROPEAN UNION and is the most important country for the transit of natural gas according to BUNDESMINISTERIUM FÜR

[1] Note that natural gas usually has a better hydrogen to carbon ratio than other conventional fuels and is hence more efficient in terms of power per CO_2 emissions.

[2] **Primary control:** Automatic frequency response within a time range of 30 s. Note that primary control is passively achieved as the rotor of a gas turbine is a rotating mass that is synchronized with the public power grid according to the UNION FOR THE CO-ORDINATION OF TRANSMISSION OF ELECTRICITY [8]. **Secondary control:** Changing load within minutes [8].

.

WIRTSCHAFT UND ENERGIE [10]. Further expansion of the natural gas infrastructure in Germany is planned for the near future as mentioned by DIE FERNLEITUNGSBETREIBER [11]. For example, gas-based generation capacities with an accumulated power output of 883 MW are currently being built, which is a third of the total amount of new capacities according to the BUNDESNETZAGENTUR [12].

1.1. Load Flexible Gas Turbines

As discussed above, gas turbines may become increasingly crucial to compensate the emerging volatilities of renewables. In order to fulfill this role, modern gas turbines need to be able to perform fast load changes in a large operating window. Load flexibility is hence an essential feature for meeting the requirements of tomorrow and is thus the subject of scientific engineering today. In general, load changes in gas turbines are achieved by adjusting the fuel supply as mentioned by Sattelmayer [13]. A simultaneous reduction of the air mass flow can be accomplished to a certain degree by means of adjusting the compressor's guide vanes as discussed by Möning and Waltke [14]. Once the minimum air mass flow is reached, a further reduction in load leads to a decrease of the global fuel-to-air ratio and colder flames. Figure 1.1 qualitatively illustrates nitrogen oxide (NO_x) and carbon monoxide (CO) emissions as a function of the adiabatic flame temperature T_{ad}. NO_x is mainly a function of temperature according to the Arrhenius law. The key difference between NO_x and CO is that the latter is an intermediate species in the context of hydrocarbon-based combustion. CO usually reaches a maximum within the flame that is by orders of magnitude higher than the limits given by emission legislations. The burnout of CO is hence a crucial process to reduce CO emissions. Consequently, super-equilibrium CO may occur in cold conditions as the temperature-sensitive burnout of CO cannot be completed. Under conditions that show sufficiently high temperatures, the burnout is fast and the reactive flow quickly approaches equilibrium. Below a specific flame temperature $T_{ad,trans}$, the equilibrium state can no longer be reached and CO emissions rise sharply. The lower limit of fuel reduction is given by the lean blowout limit that occurs at an adiabatic temperature denoted as $T_{ad,lbo}$. The contrary trends in CO and NO_x as functions of T_{ad} may lead to

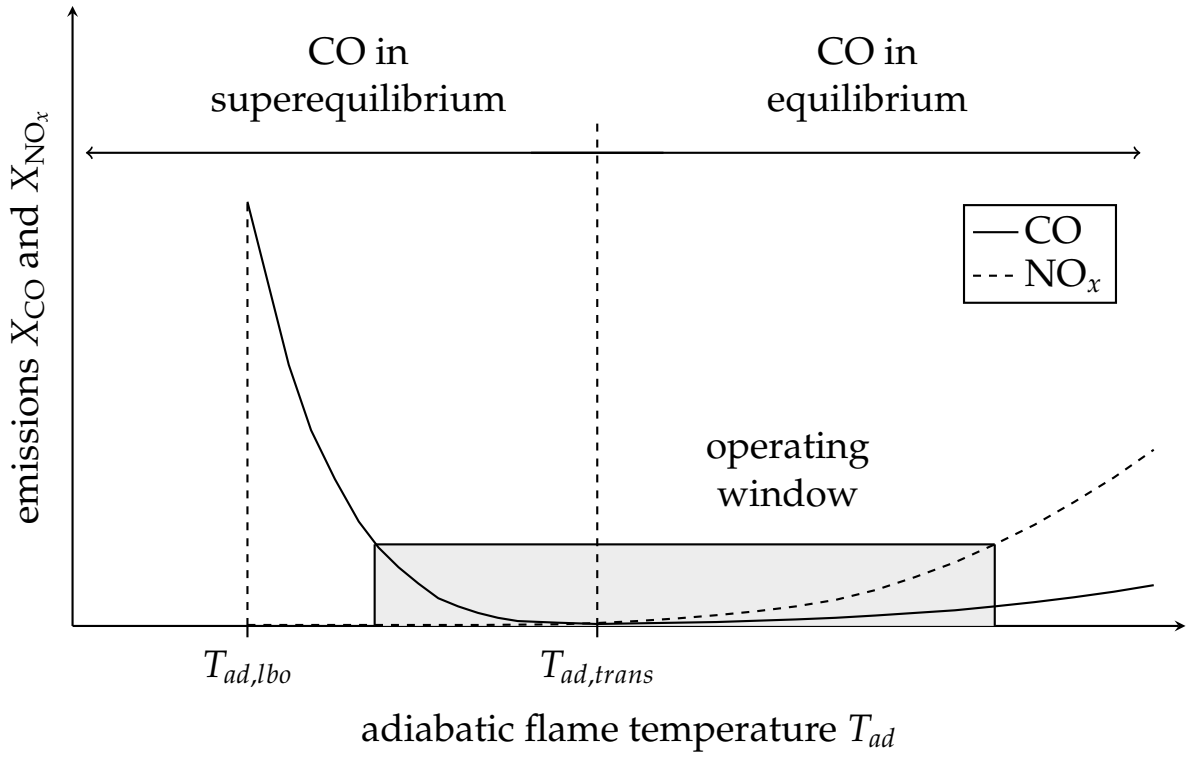

Figure 1.1.: Temperature dependent emissions of a premixed flame (adapted from Steinbach et al. [16]).

a narrow range of possible operating conditions. For example, Lefebvre and Ballal [15] state that flame temperatures between 1670 K and 1900 K should be aimed to obtain NO_x values below 15 ppmv and CO values below 25 ppmv. There are several strategies for augmenting the operating window towards lower loads while keeping CO emissions below a certain threshold. The use of an adjustable combustor geometry can be employed to control the flame temperature by air staging [15]. The strategy is to increase air mass flow at full load to cool the burnout area and prevent the oxidation of Dinitrogen (N_2) to NO_x. At part-load conditions, air is reduced to increase the temperature in order to ensure CO burnout. However, the operation of a variable combustor geometry is complex and its industrial employment is rare [15].

A more practical approach to extend the range of possible operating conditions is to stage fuel instead of air. Fuel staging is the redistribution of fuel supply to exploit various mechanisms for the emission-safe operation of gas turbines at part load. Technical implementations of fuel staging are widely used in industry and are of high relevance for the present work.

Multiple strategies for fuel staging exist that can be characterized as follows [3]:

- **Switching to non-premixed combustion:** In this fuel staging concept, a switch from premixed to non-premixed combustion is conducted when load is decreased to a specific point. Non-premixed combustion features diffusion flames that burn close to stoichiometric conditions, which lead on the one hand to higher reactivity and advantages in terms of burnout. On the other hand, the reaction zones of diffusion flames show higher flame temperatures and thus increased NO_x emissions. High NO_x emissions can be avoided by using solely a fraction of the fuel for the pilot . The remaining fuel is still supplied to the premixed burner leading to a reactive gas that can be below the lean blowout limit and still ignites after mixing with the hot gas from the pilot flame. This is possible as the minimum temperature for self-ignition chemistry is below the lean blowout temperature as stated by Sattelmayer [13].

- **Premixed piloting:** This strategy is based on substituting the non-premixed pilot of the previous concept with a premixed zone. Since only premixed combustion takes place, lower NO_x emissions can be achieved compared to concepts with a non-premixed pilot. Guyot et al. [17] shows an application of this strategy for the staging of a single burner. In the described system, fuel is injected via a lance in the center as well as at the outer slots of a swirler. This configuration leads to two premixed regions with different fuel-to-air ratios as depicted in Figure 1.2. The premixed zone stabilizes in the center and ignites the leaner outer parts.

- **Longitudinal staging:** The idea of longitudinal staging is to obtain a primary combustion zone that is active at each operating point such as start up, part load or full load. A secondary combustion zone is located further downstream. Additional fuel is supplied to the secondary zone that is ignited by the stable primary zone. An example for the application of longitudinal staging in an aircraft engine can be found in Koff [18].

[3] Note that the proposed classification is inspired by Sattelmayer [13] and adapted to fit in the framework of this work.

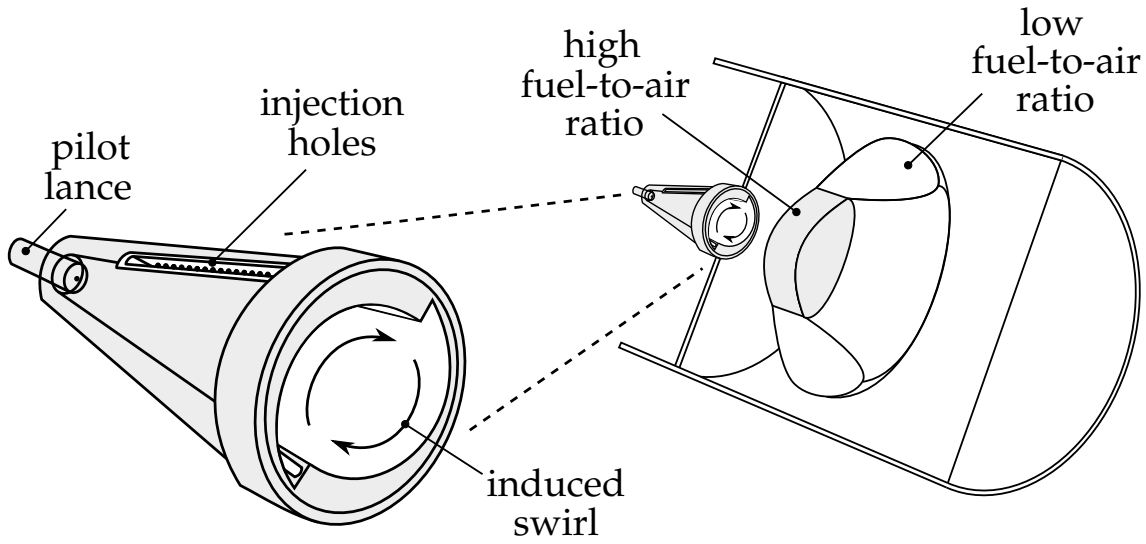

Figure 1.2.: Sketch of a piloted swirl burner (inspired by Guyot et al. [17]).

- **Sequential combustion:** Partial decompression during combustion has thermodynamic advantages such as lower flame temperatures and higher efficiencies. This principle is exploited in sequential combustion as fuel is supplied to multiple combustion chambers at different levels of pressure. Technical implementations of this concept can be found by Döbbeling et al. [19], by Hiddemann et al. [20] or by Güthe et al. [21].

- **Fuel staging in multi-burner systems:** The previous fuel staging concepts do not take advantage of the fact that gas turbines usually employ multiple burners. Examples for burner arrangements in multi-burner systems are illustrated in Figure 1.3. There is on the one hand the option of implementing the aforementioned concepts for each burner individually. On the other hand, multi-burner systems open up the possibility of exploiting the interaction between adjacent burners to apply further fuel staging strategies. Multi-burner fuel staging concepts usually have multiple stages. At each stage, a predefined group of burners is switched off. There are two different paradigms in the way fuel is decreased before the switch-off events occur:

  – In the first concept, fuel supply of all active burners is evenly decreased before a group of burners is switched off. By deactivating a group of burners, the fuel surplus needs to be redistributed to

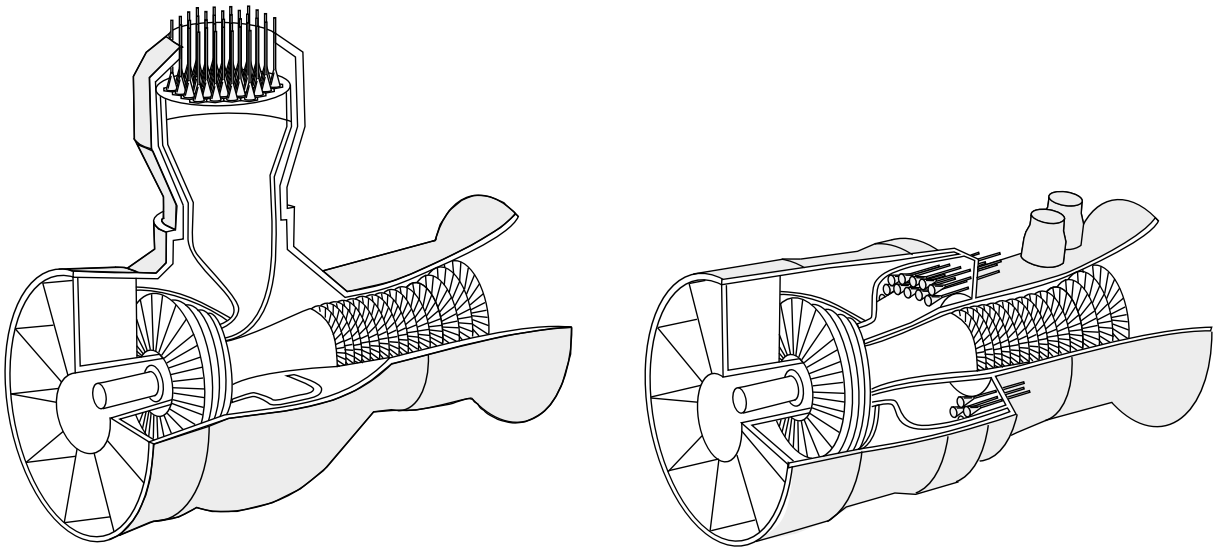

Figure 1.3.: Illustration of a gas turbine with silo combustion chamber on the left (inspired by Vorontsov et al. [22]) and an annular combustion chamber on the right (inspired by Tripod et al. [23]).

the remaining group of active burners. Note that this can be done by operating all active burners above the lean blow out limit at any time.

– The second concept is different as solely the fuel supply of the group of burners that is intended to be switched off is reduced. All remaining burners continue to operate at reference fuel supply. Note that the burners that are intended to be switched off are traversed from reference conditions to pure air.

Both concepts are of technical relevance and covered separately in different validation cases in this work.

1.2. Goals of this Work and Previous Research

After discussing the importance of extending the operating window to achieve lower loads, the question arises how scientific research can support the development of new gas turbine combustors. Numerical methods are gaining in importance in all industrial sectors due to the sharply increasing computing power that is described by Moore [24]. This trend

disrupts conventional development processes, as costly experiments can be partially replaced by simulations. Note that this applies in particular to the development of complex systems such as gas turbine combustors that are operated at high-pressure conditions. Hence, interest in the numerically supported design of new combustors and operating concepts is steadily increasing as inefficient design-built-measurement cycles can be avoided.

The aim of this work is to develop a modeling strategy that is capable of accurately predicting combustion and the corresponding CO emissions in gas turbines that operate at part-load conditions. Computational Fluid Dynamics (CFD) is well suited in order to achieve the specified goals. In CFD, governing equations are employed, which are able to describe quantities continuously in space. Note that the consideration of local effects is crucial for this work. For instances, the above introduced concepts of fuel staging are based on numerous local effects that cannot be covered by integral approaches. In general, CFD is able to describe flow, combustion and emissions in an exact[4] way. However, the direct solution is resource intense as vast grids are necessary to resolve all turbulent structures. Thus, modeling is necessary to drastically reduce the computational effort. The models of the present work seek to support the development of new gas turbine combustion systems. In order to create an approach that is able to be applied in industry, different requirements have to be met. All models should work under pressure conditions that range from atmospheric pressure[5] to the full range of high-pressure conditions of modern gas turbines. The modeling strategy must be able to cover the situation of pilot operation where a stable reaction zone ignites gases that are below the lean blowout limit. In addition, a possible implementation of the proposed models in industrial processes requires high precision[6] at low computational costs.

[4] It should be noted that the governing equations are actually derived with simplifications. However, the direct solution of the governing equations is sufficiently accurate in a way that is relevant for technical applications.

[5] The model validity at atmospheric conditions is necessary as validation data may be measured in atmospheric test rigs.

[6] A precise model implies the ability to accurately predict physicochemical quantities without model tuning.

One may ask why existing, widely used combustion models are not able to achieve the objectives of the present work. An often used simplification of standard combustion models is the assumption that a turbulent flame brush can be described by a set of laminar flamelets (referred to as the flamelet assumption). Flamelets are thin reaction zones that divide unburnt from burnt material. The oxidation of CO in flamelets is fast due to the availability of a stable radical pool and CO always reaches equilibrium in short length and time scales. In contrast to the flamelet assumption, part-load combustion in gas turbines usually features super-equilibrium CO in the exhaust gas far behind the heat release zone. A flamelet-based combustion model can only predict elevated CO emissions at the outlet when flamelets fluctuate through the whole combustion chamber. The occurrence of flamelets in the exhaust gas is not realistic as the flame usually anchors close to the burner exit. Nevertheless, the prediction of CO using the popular Flamelet Generated Manifold (FGM) model can be found by Goldin et al. [25,26]. Here, tuning of a semi-empirical closure is necessary to achieve a reasonable prediction of CO. The authors conclude that FGM drastically overestimates the source terms of CO oxidation. Another attempt to numerically predict CO using CFD can be found by Wegner et al. [27]. In the described approach, CO is determined by an own transport equation. Within the turbulent flame brush, CO is initialized with its peak value at a predefined reaction progress. The peak value of CO is determined by one-dimensional simulations based on detailed chemistry. The approach by Wegner et al. [27] has several simplifications that are not accurate as argued later.

Based on literature research and the industrial requirements specified above, the following requirements for the CFD-based modeling approach are identified:

- **Momentum:** The technical relevance of this work requires to focus on efficient models. Hence, the proposed modeling strategy is based on averaged equations that neglect all turbulent structures.

- **Mass and Species:** The combustion time scales are orders of magnitude smaller than the time scales of the late CO burnout. Thus, a divide and conquer approach is reasonable: Two different models

are developed, covering combustion on the one hand and the late CO burnout on the other hand. It is worth noting that the CO model depends on the combustion model but not vice versa.

  - **Combustion:** The simulation of combustion in gas turbines at part load requires an advanced modeling strategy. Combustion in cold conditions is demonstrated to be in particularly susceptible for flame stretch and heat loss. Hence, a combustion model is proposed that takes both effects into account. Furthermore, the combustion model is able to consider partially-premixed combustion in order to cover quenching effects due to secondary air or the effect of poor mixing quality.

  - **CO model**: The aforementioned separation of time scales is crucial for the successful modeling of CO. Hence, CO is described independently from the combustion model. Within the turbulent flame brush, CO is modeled on the basis of flamelets. Downstream of the turbulent flame brush, the burnout of CO is dominated by chemical time scales and is thus described by chemical models.

- **Energy:** Heat loss may significantly effect both combustion and CO especially in cold conditions. This is why the temperature drop due to non-adiabatic effects must be taken into account. For this reason, the proposed modeling strategy is able to consider heat loss.

1.3. Thesis Structure

In the following, the structure of the thesis is presented. Chapter 2 introduces the theoretical fundamentals that are relevant for this work. Chapter 3 shows the combustion model that covers important effects, which are relevant for cold conditions. An application of the combustion model to an atmospheric single-burner test rig is shown. Numerical results are compared to experimental OH^*[7] in order to qualitatively evaluate the model's performance. In addition, a comparison of the proposed mod-

[7] OH^* is an excited hydroxyl molecule that can be used to indicate heat release distributions.

eling strategy with standard, widely used combustion models is shown. Chapter 4 presents the CO model that consists of several submodels. Locally resolved measurements of CO emissions are crucial for the validation of the individual parts of the CO model. For this reason, experiments to measure CO distributions within the combustion chamber have been conducted. Validation of the CO model in various fuel-staging scenarios is shown in two different multi-burner cases. Furthermore, the models are applied to an advanced combustor design. This work is finalized with Chapter 5 where the content of this work is recapitulated.

2 Fundamentals of Turbulent Combustion

This chapter introduces the fundamentals of turbulent, reactive flows that are relevant for the present work. Section 2.1 presents a set of governing equations for reactive flows. In addition, the modeling of turbulence is addressed in Section 2.2. The last Section 2.3 covers turbulent combustion.

2.1. Governing Equations for Reactive Flows

The decisive difference between the mathematical description of reactive and non-reactive flows is that the conversion of species requires to view the gas as a mixture that may significantly change its composition over time. This leads to three challenges in formulating governing equations for reactive flows as stated by Poinsot and Veynante [28]:

- Reactions are able to change the species composition of the fluid. This usually leads to a tremendous change of the thermodynamic properties. Thus, all species must be tracked in order to evaluate quantities like temperature, density, and heat capacity.
- The source term of each species must be closed. Hence, knowledge of the combustion chemistry is required.
- Multi-component diffusion of momentum, species, and energy is of high complexity and requires modeling.

In the following, a brief introduction of the governing equations for non-isothermal, reactive flows is given. The continuous description of momentum, mass, and energy forms the basis to numerically solve combustion problems. A more detailed view on this set of equations is given by

Kuo [29], by Williams [30], and in a more compact form by Poinsot and Veynante [28] as well as by Peters [31].

2.1.1. Mass

As combustion is mass conservative, the classical form of the continuity equation can be used for the description of reactive flows:

$$\frac{\partial \rho}{\partial t} + \frac{\partial \rho u_i}{\partial x_i} = 0\,. \tag{2.1}$$

This equation states that the local rate of mass change in a control volume is solely caused by convective mass exchange with the environment.

2.1.2. Momentum

Momentum can be described by

$$\frac{\partial \rho u_j}{\partial t} + \frac{\partial \rho u_i u_j}{\partial x_i} = -\frac{\partial p}{\partial x_j} + \rho \sum_{s=1}^{\mathcal{N}} Y_s F_{s,j} + \frac{\partial \sigma_{ij}}{\partial x_i}\,. \tag{2.2}$$

The left hand side consists of the local rate of momentum change and a convective term. On the right hand side, momentum changes due to pressure effects is described by the first term. Moreover, the second term specifies the influence of volume forces $F_{s,j}$ on momentum. Here, $F_{s,j}$ acts solely on the fraction of mass that corresponds to species s. Thus, $F_{s,j}$ must be multiplied by the species mass fraction Y_s that reads

$$Y_s = \frac{m_s}{m}\,. \tag{2.3}$$

In addition, the third term of Equation 2.2 tracks momentum changes due to viscous dissipation in which σ_{ij} is the viscous tensor:

$$\sigma_{ij} = -\frac{2}{3}\mu \frac{\partial u_k}{\partial x_k}\delta_{ij} + \mu\left(\frac{\partial u_i}{\partial x_j} + \frac{\partial u_j}{\partial x_i}\right)\,. \tag{2.4}$$

Here, μ denotes the dynamic viscosity and δ_{ij} the Kronecker delta. Note that Equation 2.2 does not feature additional terms to consider charac-

teristics from reactive flows. Nevertheless, combustion is implicitly captured as viscosity and density change significantly.

In order to describe the coupling between velocity and pressure, two different paradigms exist. In density-based approaches, the density field is calculated by the continuity equation and pressure subsequently by the ideal gas law. Pressure-based methods calculate pressure using algebraic models on the basis of the velocity field in a way that continuity is satisfied. The CFD code that is used in this work employs a pressure-based scheme by Patankar [32] called SIMPLE.

2.1.3. Species

As mentioned before, species must be tracked in order to derive the thermodynamic state of the flow. The transport equation for species s reads

$$\frac{\partial \rho Y_s}{\partial t} + \frac{\partial \rho u_i Y_s}{\partial x_i} = -\frac{\partial \rho V_{s,i} Y_s}{\partial x_i} + \dot{\omega}_s \, . \tag{2.5}$$

Species diffusion is described by the first term on the right hand side in which $V_{s,i}$ is the diffusion velocity of species s in i-th direction. As demonstrated by Williams [30], an analytical solution to multi-component species diffusion exists. However, implementations of the proposed governing equations usually employ diffusion models in order to keep the numerical effort low. In this work, the one-dimensional flamelet simulations model diffusion by employing a first-order approximation of the Chapman-Enskog theory by Chapman et al. [33]. Note that the Chapman-Enskog theory considers multi-component diffusion instead of using mixture-averaged diffusion coefficients.

The second term on the right hand side of Equation 2.5 describes the source term of species due to chemical reactions. As mentioned before, chemical source terms are unknown and require modeling that is presented in the following.

A generic reaction r specifies the reorganization of atoms in molecules:

$$\sum_{s=1}^{\mathcal{N}} \gamma_{for,r,s}\, \aleph_s \rightleftharpoons \sum_{t=1}^{\mathcal{M}} \gamma_{rev,r,t}\, \aleph_t \,. \tag{2.6}$$

$\aleph$ denotes a placeholder for species names and γ the corresponding stoichiometric coefficients for each species. A set of $\mathcal{R}$ reactions contributes to the source term of species s:

$$\dot{\omega}_s = \sum_{r=1}^{\mathcal{R}} \dot{\omega}_{s,r} = W_s \sum_{r=1}^{\mathcal{R}} (\gamma_{rev,s,r} - \gamma_{for,s,r}) \dot{\varsigma}_r \,. \tag{2.7}$$

W_s is the molecular mass and $\dot{\varsigma}_r$ the molecular reaction rate. The latter can be calculated using the product of the rate constant k_{arr} multiplied with the corresponding species concentration $[\aleph]$:

$$\dot{\varsigma}_r = k_{arr,for,r} \prod_{s=1}^{\mathcal{N}} [\aleph_s]^{\gamma_{for,s,r}} - k_{arr,rev,r} \prod_{t=1}^{\mathcal{M}} [\aleph_t]^{\gamma_{rev,t,r}} \,. \tag{2.8}$$

The forward rates of reaction r are obtained by the Arrhenius law:

$$k_{arr,for,r} = A_{freq,r} T^{\beta_r} \exp\left(-\frac{E_{a,r}}{RT}\right) \,. \tag{2.9}$$

Note that reverse rates are derived from the equilibrium constants and the forward rates.

Based on the specified set of equations, the closure of the species source term $\dot{\omega}_s$ requires knowledge of all occurring chemical reactions with the corresponding Arrhenius parameters ($A_{freq,r}$, β_r, and $E_{a,r}$). For this purpose, chemical descriptions called kinetic mechanisms are frequently published. A selection of kinetics for the combustion of hydrocarbons can be found in Table 2.1. For each kinetic mechanisms, the number of species ($\mathcal{N}$), the number of reactions ($\mathcal{R}$) , as well as the highest number of carbons that occur in molecules ($\mathcal{C}_{carbon,max}$) are specified. Moreover, the average time to calculate a single time step in a transient, zero-dimensional simulation of a constant pressure reactor is shown. As one can see, the calculation times ($\hat{t}_{iter}$) differ significantly for each kinetic and correlate with the corresponding number of species ($\mathcal{N}$) and reactions ($\mathcal{R}$). Choos-

Table 2.1.: A selection of kinetic mechanisms for the combustion of hydrocarbons (t_{iter} is determined from a constant pressure reactor at $T = 512\,\mathrm{K}$, $p = 10\,\mathrm{bar}$ and $\phi = 0.75$, calculated using CANTERA [34]).

	$\mathcal{N}$ (species)	$\mathcal{R}$ (reactions)	$\mathcal{C}_{carbon,max}$	t_{iter} in s
DRM 19 [35]	21	84	2	1.67e-3
DRM 22 [36]	24	104	2	2.13e-3
GRI 3.0 [37]	53	325	3	1.09e-2
GALWAY 1.3 [38]	253	1542	4	3.44e-2
GALWAY 2.0 [39]	493	2716	8	3.2e-1

ing the right kinetic for a specific problem is not only a trade-off between complexity and efficiency. More importantly, it is good practice to review the range of validity in terms of pressure and fuel.

2.1.4. Energy

The energy equation appears in different forms. A possible choice is to transport h that is defined as the sum of sensible and chemical enthalpy:

$$h = \underbrace{\int_{T^0}^{T} c_p(T)dT}_{h_{sens}} + \underbrace{\sum_{s=1}^{\mathcal{N}} \Delta h^0_{form,s} Y_s}_{h_{ch}} \,. \tag{2.10}$$

The energy equation for h reads

$$\rho \frac{Dh}{Dt} = \frac{Dp}{Dt} - \frac{\partial q_i}{\partial x_i} + \sigma_{ij}\frac{\partial u_i}{\partial x_j} + \rho \sum_{s=1}^{\mathcal{N}} Y_s F_{s,i} V_{s,i} + \dot{\omega}_{h,gen} \tag{2.11}$$

with

$$\rho \frac{D\theta}{Dt} = \rho \left(\frac{\partial \theta}{\partial t} + u_i \frac{\partial \theta}{\partial x_i} \right) = \frac{\partial \rho \theta}{\partial t} + \frac{\partial \rho u_i \theta}{\partial x_i} \,. \tag{2.12}$$

The first term on the right hand side of Equation 2.11 describes enthalpy changes due to the temporal change of pressure. The second term expresses enthalpy changes due to diffusion of heat or species with different enthalpies. Heating due to viscous effects is expressed by the third term. Moreover, the fourth term on the right hand side describes enthalpy changes due to volume forces. The last term $\dot{\omega}_{h,gen}$ denotes generic sources like the absorption of radiation energy. Note that Equation 2.11 has no source term due to chemical rates as h is conservative[1] in combustion. A source term describing the heat release due to combustion appears in the sensible enthalpy form of the energy equation:

$$\begin{aligned}\rho\frac{Dh_{sens}}{Dt} =& \frac{Dp}{Dt} - \frac{\partial q_i}{\partial x_i} + -\frac{\partial}{\partial x_i}\left(\rho\sum_{s=1}^{\mathcal{N}} h_{sens,s}Y_sV_{s,i}\right) \\ &+ \sigma_{ij}\frac{\partial u_i}{\partial x_j} + \rho\sum_{s=1}^{\mathcal{N}} Y_sF_{s,i}V_{s,i} + \dot{\omega}_{h,ch} + \dot{\omega}_{h,gen}\end{aligned} \tag{2.13}$$

with

$$\dot{\omega}_{h,ch} = -\sum_{s=1}^{\mathcal{N}} \Delta h^0_{form,s}\dot{\omega}_s\,. \tag{2.14}$$

2.2. Modeling Turbulence

In the following, a method is presented that drastically reduces the numerical effort by averaging transient turbulent structures. The section begins with an introduction to turbulence whereat useful quantities are defined. Section 2.2.2 presents a set of ensemble-averaged governing equations. Here, unclosed quantities called Reynolds-stresses need to be closed by turbulence models, which is the subject of Section 2.2.2.1.

2.2.1. Scales in Turbulent Flows

Turbulent flows feature transient, irregular and seemingly random or chaotic fluid motions as mentioned by Pope [40]. The transition from a

[1] In a combustion process, chemical enthalpy is converted to sensible enthalpy. Hence, the sum of both is conservative during the combustion process.

laminar flow to a turbulent state takes place when inertial forces dominate viscous forces. Turbulent flows show rotating structures denoted as eddies occurring in a broad range of length scales. Technically relevant properties of the flow are significantly impacted by turbulent structures. For instance, the mixing of two components occurs significantly slower in laminar conditions. Unfortunately, turbulence itself is far from being understood and mathematical descriptions often have a semi-empirical character. The Eddy Cascade Hypotheses by Richardson [41] (and contributions by Kolmogorov [42]) is a theory that describes the interaction of eddies occuring in a broad spectrum of length scales. Richardson's model leads to various useful quantities that are introduced in the following. The turbulent kinetic energy k is defined by the square of the eddies circumferential speed u':

$$k = u'^2(r)\,. \tag{2.15}$$

Dissipation ϵ can be estimated by dividing k with the eddy's circumferential time:

$$\epsilon = \frac{u'^2(r)}{\tau_{eddy}(r)} = \frac{u'^3(r)}{r}\,. \tag{2.16}$$

In order to categorize eddies by length and energy, further quantities are introduced in the following. The wave number w is the inverse of the eddies diameter l_{eddy}. Furthermore, the density of turbulent kinetic energy in wave number space reads

$$E = \frac{dk}{dw}\,. \tag{2.17}$$

E and w are plotted in Figure 2.1. Eddies that are in the large scale region are dominated by instabilities that do not have an universal character, but are rather geometry-dependent. The logarithm of E increases in the large scale region with a power law between w^2 and w^4 with increasing logarithmic wave number w as mentioned by Peters [31]. Moreover, the kinetic energy of eddies has a maximum at the integral length scale l_{int}. After the maximum is reached, E decreases with a power law of $w^{-\frac{5}{3}}$ in the inertial subrange according to Peters [31]. The end of the inertial sub-

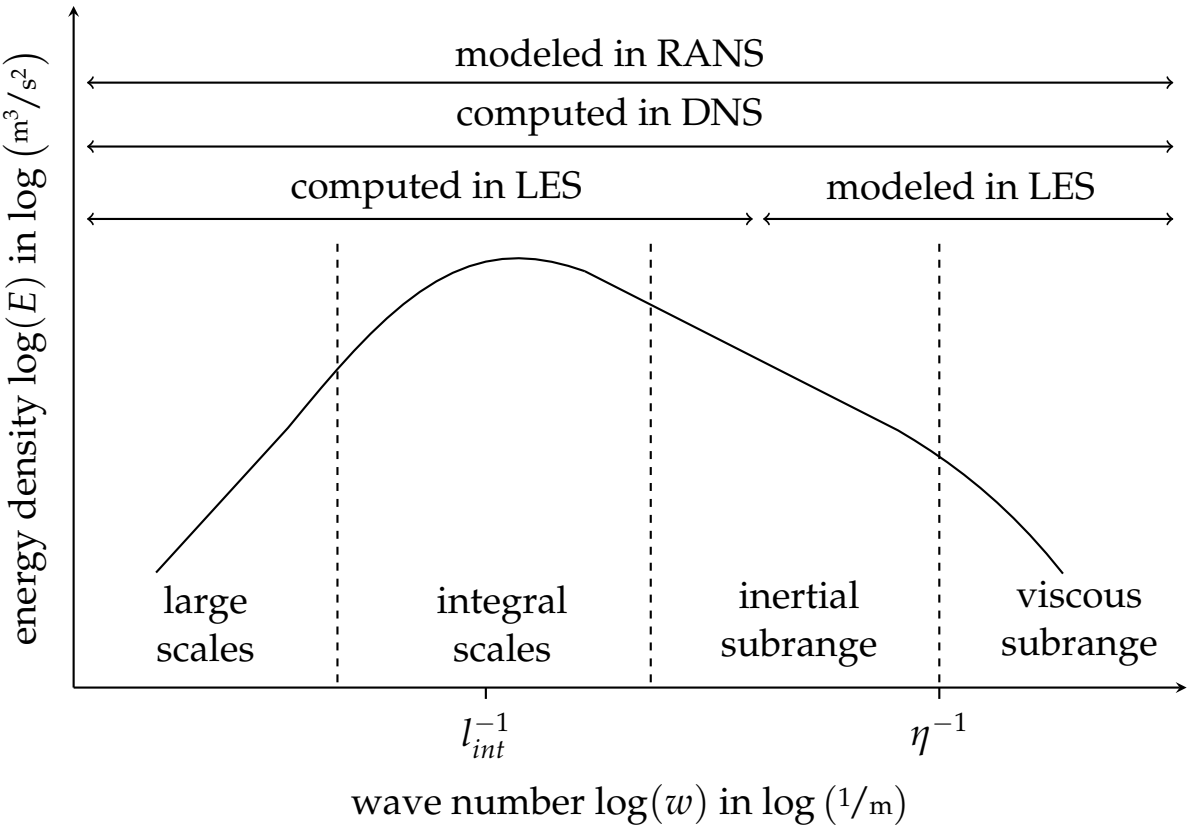

Figure 2.1.: Turbulence energy spectrum (adapted from Peters [31] as well as from Poinsot and Veynante [28]).

range is marked by the Kolmogorov scale η. Smaller eddies are in the viscous subrange in which the eddy's energy decreases exponentially due to viscous effects. In order to derive an expression for the Kolmogorov length η, the Reynolds number Re is introduced that quantifies the ratio of inertial to viscous forces in a dimensionless way:

$$Re(r) = \frac{u'(r)r}{\nu}\,. \tag{2.18}$$

The following expression to evaluate the Kolmogorov length η is derived by assuming that the viscous subrange starts when viscous forces equal inertial forces:

$$Re(\eta) = \frac{u'(\eta)\eta}{\nu} = 1 \longrightarrow \eta = \frac{\nu}{u'(\eta)}\,. \tag{2.19}$$

2.2.2. Reynolds-Averaged Governing Equations for Reactive Flows

Solving the instantaneous governing equations of Section 2.1 is denoted as Direct Numerical Simulation (DNS). DNS resolves even the smallest turbulent structures that requires vast computational grids leading to high computational effort. Thus, DNS is up to now limited to few academic resource activities, small geometries, and low Reynolds numbers. In Large Eddy Simulations (LES), only the turbulent structures that are above a specified threshold are resolved. Below this limit, the averaged values are determined by subgrid models. A third approach called Reynolds-Averaged Navier-Stokes (RANS) solves solely the mean values of all turbulent structures. This leads to a significant reduction of calculation time and makes it furthermore possible to employ two-dimensional geometries and symmetric or periodic boundary conditions. A further advantage of RANS is the possibility to evaluate a single stationary state instead of solving a time series. Note that all methods developed in this work are based on RANS, which is introduced in the following. Ensemble averaging denotes the split of an arbitrary quantity θ into a mean and a fluctuating part:

$$\theta = \overline{\theta} + \theta' \,. \tag{2.20}$$

Using the standard RANS equations based on ensemble averaging lead to specific challenges in flows of non-constant density. Hence, solvers usually employ the mass-weighted mean introduced by Favre [43]. A Favre-averaged generic variable is defined by

$$\tilde{\theta} = \frac{\overline{\rho\theta}}{\overline{\rho}} \,. \tag{2.21}$$

In addition, fluctuations of θ are separated:

$$\theta = \tilde{\theta} + \theta'' \text{ with } \tilde{\theta''} = 0 \,. \tag{2.22}$$

The Favre-averaged governing equations for mass, momentum, species, and energy read[2]

$$\frac{\partial \overline{\rho}}{\partial t} + \frac{\partial \overline{\rho}\tilde{u}_i}{\partial x_i} = 0\,, \tag{2.23}$$

$$\frac{\partial \overline{\rho}\tilde{u}_j}{\partial t} + \frac{\partial \overline{\rho}\tilde{u}_i\tilde{u}_j}{\partial x_i} + \frac{\partial \overline{p}}{\partial x_j} = \frac{\partial}{\partial x_i}\left(\overline{\sigma}_{ij} - \overline{\rho}\widetilde{u_i'' u_j''}\right)\,, \tag{2.24}$$

$$\frac{\partial \overline{\rho}\tilde{Y}_s}{\partial t} + \frac{\partial \overline{\rho}\tilde{u}_i\tilde{Y}_s}{\partial x_i} = -\frac{\partial}{\partial x_i}\overline{\rho}\left(\widetilde{u_i'' Y_s''} + \overline{V_{s,i}Y_s}\right) + \overline{\dot{\omega}}_s\,, \tag{2.25}$$

$$\begin{aligned} &\text{and}\quad \frac{\partial \overline{\rho}\tilde{h}_{sens}}{\partial t} + \frac{\partial \overline{\rho}\tilde{u}_i\tilde{h}_{sens}}{\partial x_i} = \overline{\frac{Dp}{Dt}} \\ &- \frac{\partial}{\partial x_i}\left(\overline{\rho u_i'' h_{sens}''} + \overline{\rho\sum_{s=1}^{N} h_{sens,s}V_{s,i}Y_s} - \overline{q_i}\right) \\ &+ \overline{\sigma_{ij}\frac{\partial u_i}{\partial x_j}} + \overline{\dot{\omega}}_{h,ch} + \overline{\dot{\omega}}_{h,gen} \end{aligned} \tag{2.26}$$

with

$$\overline{\frac{Dp}{Dt}} = \frac{\partial \overline{p}}{\partial t} + \tilde{u}_i\frac{\partial \overline{p}}{\partial x_i} + \overline{u_i''\frac{\partial p}{\partial x_i}}\,. \tag{2.27}$$

Here, several unclosed terms appear: Reynolds-stresses $\widetilde{u_i'' u_j''}$, turbulent mass fluxes $\widetilde{u_i'' Y_s''}$, and turbulent enthalpy flux $\widetilde{u_i'' h_{sens}''}$. The modeling of these terms is introduced in the following. Furthermore, the ensemble-averaged species source term $\overline{\dot{\omega}}_s$ is closed by combustion models, which is the subject of Section 2.3. A further unclosed term is the ensemble-averaged product of velocity fluctuation and spatial pressure gradient $\overline{u_i''\partial p/\partial x_i}$ appearing in Equation 2.27. This term is usually small and often neglected as mentioned by Poinsot and Veynante [28].

[2] Volume forces have been neglected for the sake of clarity.

2.2.2.1. Modeling Reynolds Stresses

The Reynolds stresses are closed by turbulence models that are often based on the approximation by Boussinesq [44]:

$$\overline{\rho u_i'' u_j''} \approx \overline{\rho}\widetilde{u_i'' u_j''} \approx -\mu_t \left(\frac{\partial \tilde{u}_i}{\partial x_j} + \frac{\partial \tilde{u}_j}{\partial x_i} - \frac{2}{3}\delta_{ij}\frac{\partial \tilde{u}_k}{\partial x_k} \right) + \frac{2}{3}\overline{\rho}k \,. \tag{2.28}$$

Here, the turbulent dynamic viscosity μ_t appears and requires closure. Due to the technical relevance, a variety of semi-empirical models have been published. The popular k-ϵ by Jones and Launder [45] is introduced in the following. The k-ϵ model uses two transport equations to determine k and ϵ. With the knowledge of both quantities, μ_t can be estimated using the following approximation:

$$\mu_t = \overline{\rho} C_\mu \frac{k^2}{\epsilon} \tag{2.29}$$

$$\frac{\partial \overline{\rho} k}{\partial t} + \frac{\partial \overline{\rho} \tilde{u}_i k}{\partial x_i} = \frac{\partial}{\partial x_i}\left(\frac{\partial k}{\partial x_i}\left(\mu + \frac{\mu_t}{C_\sigma} \right) \right) + P_k - \overline{\rho}\epsilon \tag{2.30}$$

$$\frac{\partial \overline{\rho} \epsilon}{\partial t} + \frac{\partial \overline{\rho} \tilde{u}_i \epsilon}{\partial x_i} = \frac{\partial}{\partial x_i}\left(\frac{\partial \epsilon}{\partial x_i}\left(\mu + \frac{\mu_t}{C_\epsilon} \right) \right) + C_{\epsilon,1}\frac{\epsilon}{k}P_k - C_{\epsilon,2}\overline{\rho}\frac{\epsilon^2}{k} \,. \tag{2.31}$$

C_μ, C_ϵ, $C_{\epsilon,1}$, $C_{\epsilon,2}$, C_σ are model constants. Moreover, P_k reads

$$P_k = -\underbrace{\overline{\rho}\widetilde{u_i'' u_j''}}_{Boussinesq} \frac{\partial \tilde{u}_i}{\partial \tilde{x}_j} \,. \tag{2.32}$$

2.2.2.2. Modeling Fluxes

As discussed above, simulations based on RANS do not resolve turbulent structures. Thus, turbulent fluxes are unknown and require modeling. These terms appear in Equation 2.25 and 2.26 in the form of $\widetilde{u_i'' Y_s''}$ and $\widetilde{u_i'' h_{sens}''}$.

A popular way to treat turbulent fluxes of an arbitrary scalar θ is to use the gradient assumption:

$$\widetilde{\overline{\rho} u_i'' \theta''} = -\frac{\mu_t}{Sc_{t,\theta}} \frac{\partial \tilde{\theta}}{\partial x_i} \,. \tag{2.33}$$

Here, the turbulent Schmidt number appears that reads

$$Sc_{t,\theta} = \frac{\mu_t}{D_{t,\theta}} \,. \tag{2.34}$$

$D_{t,\theta}$ can be interpreted as a mass diffusion coefficient of θ due to turbulence. In the present work, a constant Schmidt number of 0.7 is used. The potential significance of this simplification is discussed by Veynante et al. [46].

Note that molecular diffusion is usually significantly smaller than turbulent fluxes and hence often neglected.

2.3. Modeling Combustion

In the following, the theoretical fundamentals of turbulent (partially) premixed combustion are covered. The first section shows a freely-propagating flamelet[3]. Furthermore, the mechanisms of stretched flames propagating in moving flows are presented in Section 2.3.2. Section 2.3.3 discusses flames in turbulent environments and introduces a method to classify turbulent premixed combustion regarding the turbulence-chemistry interaction. In Section 2.3.4, a selection of standard combustion models is introduced.

2.3.1. Freely-Propagating Flames

Premixed combustion requires fuel and oxidizer to be perfectly mixed on the molecular level prior to combustion. In contrast to diffusion flames, the reaction rate is not limited by the molecular transport of fuel and oxi-

[3] The term freely propagating indicates that there is no aerodynamic interaction between combustion and flow. in order to introduce basic principles of combustion.

dizer. The global fuel to oxidizer ratio can be defined by the equivalence ratio ϕ, which reads

$$\phi = b\frac{Y_{fuel}}{Y_{oxid}} \quad \text{with} \quad b = \left.\frac{Y_{oxid}}{Y_{fuel}}\right|_{sto} . \tag{2.35}$$

Note that this definition cannot be evaluated in the exhaust gas. For a globally valid evaluation, a combustion conservative definition is needed. A popular choice is the mixture fraction f, which reads

$$f = \frac{bY_{fuel} - Y_{oxid} + Y_{oxid,u}}{bY_{fuel,u} + Y_{oxid,u}} . \tag{2.36}$$

Once the homogenous charge is ignited, a thin flame front develops and propagates towards the unburnt mixture. The one-dimensional simulation of a freely-propagating flamelet at constant f is shown in Figure 2.2. Mass flow at the inlet is iterated until the flame position is spatially stationary. The velocity of the unburnt gas mixture approaching the reaction zone is called the laminar flame velocity s_l and defines the propagation speed of a flame front in a quiescent environment. The laminar flame velocity can be evaluated at the inlet $x = 0$ as plotted in Figure 2.2 (—).

Another scale for the classification of premixed combustion is the flame front thickness. Using scaling laws, a characteristic flame thickness based on the laminar flame speed s_l and the thermal diffusivity D_{th} can be derived that reads

$$l_{diff} = \frac{\lambda_u}{\rho_u c_p s_l} = \frac{D_{th}}{s_l} . \tag{2.37}$$

This quantity is not precise and often too small as discussed by Poinsot and Veynante [28]. A more useful definition can be derived from the spatial temperature distribution as shown in Figure 2.2. It can be evaluated using:

$$l_f = \frac{\hat{T}_b - \hat{T}_u}{max\left(\left|\frac{\partial \hat{T}}{\partial x}\right|\right)} . \tag{2.38}$$

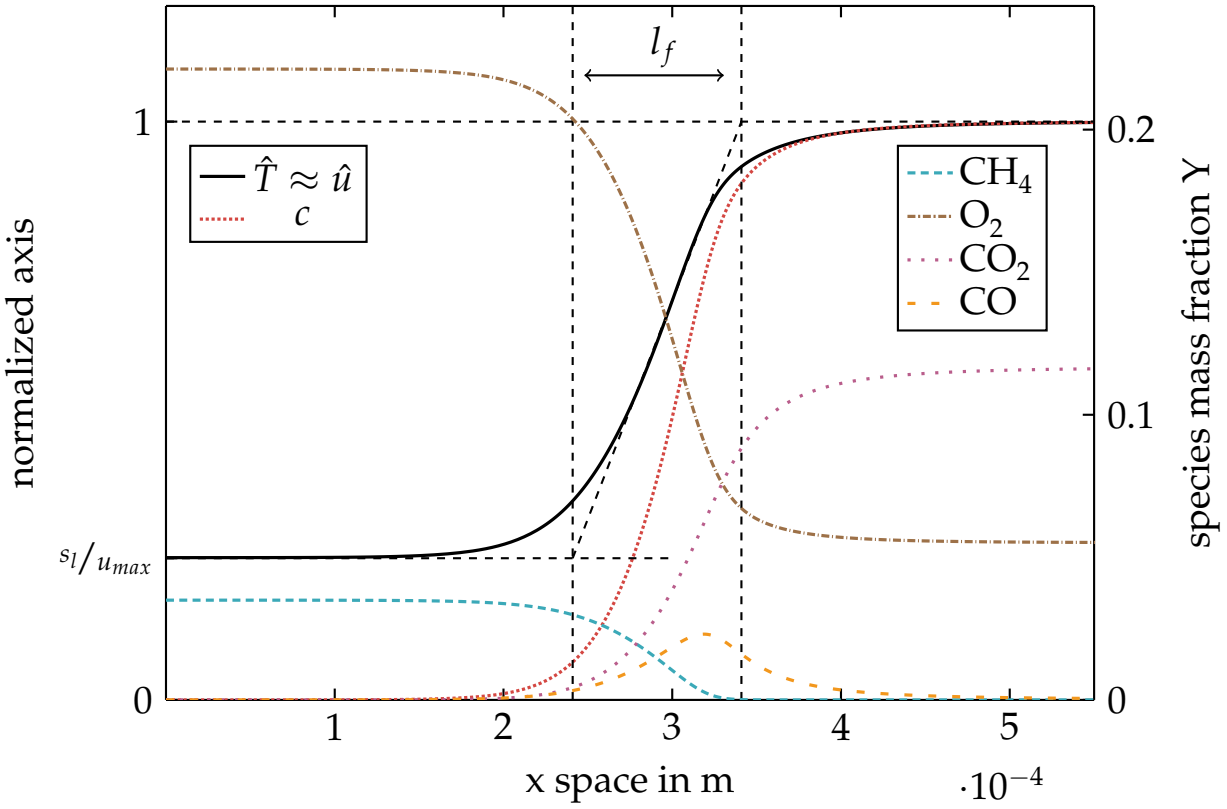

Figure 2.2.: Spatial profiles of selected quantities (freely-propagating at $T = 512\,\mathrm{K}$, $p = 10\,\mathrm{bar}$ and $\phi = 0.75$, calculated using GALWAY 1.3 [38] and CANTERA [34]).

Furthermore, the reaction progress c is plotted in Figure 2.2 (⋯). c determines the progress of the combustion process from zero to unity. The following definition for c can be employed for the combustion of hydrocarbons:

$$c = \frac{\left(Y_{\mathrm{CO}} - Y_{\mathrm{CO},u}\right) + \left(Y_{\mathrm{CO}_2} - Y_{\mathrm{CO},u}\right)}{\left(Y_{\mathrm{CO},eq} - Y_{\mathrm{CO},u}\right) + \left(Y_{\mathrm{CO}_2,eq} - Y_{\mathrm{CO},u}\right)} \,. \tag{2.39}$$

The second y-axis of Figure 2.2 represents the mass fraction of four selected species. Fuel consists of pure CH_4 (- - -) and the oxidizer is dioxygen (O_2, -·-·-). Both species decrease over the reaction zone as they convert to species of lower energetic level by releasing heat. The carbon atoms take various paths and pass numerous intermediate species before they eventually react to CO_2 (⋯) . Since almost every C-atom has to pass CO (⋯), a maximum develops within the flame.

2.3.2. Stretched Flames in Moving Environments

The flame shown in Figure 2.2 propagates in a quiescent environment (freely propagating). In reality, flames are usually exposed to multidimensional velocity fields. The aerodynamic effect of a moving flow on the flame is called flame stretch. It is defined by the temporal change of a flame surface element A_f:

$$\kappa = \frac{1}{A_f}\frac{dA_f}{dt} \ . \tag{2.40}$$

Stretching a flame leads to steeper gradients that may significantly impact the flame speed due to the following mechanisms:

- Feeding the flame with more fuel, causing the flame speed to increase.
- Cooling the flame as the diffusion of heat towards the unburnt material is increased, leading to a decrease in flame speed.

Note that both mechanisms are superimposed. Hence, the effect of stretch on flame speed is ambiguous as acceleration or deceleration is possible. A general expression for flame stretch κ can be derived from Equation 2.40 by using Reynold's transport theorem as shown by Poinsot and Veynante [28]. Flame stretch in index notation reads

$$\kappa = \underbrace{(\delta_{ij} - n_i n_j)\frac{\partial u_i}{\partial x_j}}_{\kappa_{st}} + \underbrace{s_d \frac{\partial n_i}{\partial x_i}}_{\kappa_{curv}} \ . \tag{2.41}$$

It is useful to write this equation without indices. For this purpose, a local coordinate system that is normal to the flame surface is introduced. Flame stretch then reads

$$\kappa = \underbrace{\nabla \cdot \underline{u} - (\underline{n} \otimes \underline{n}) : \nabla \underline{u}}_{\kappa_{st}} + \underbrace{s_d \nabla \cdot \underline{n}}_{\kappa_{curv}} \ . \tag{2.42}$$

The displacement speed s_d defines the flame front velocity relative to the flow in normal direction ($\underline{n}$). The first two terms on the right hand side

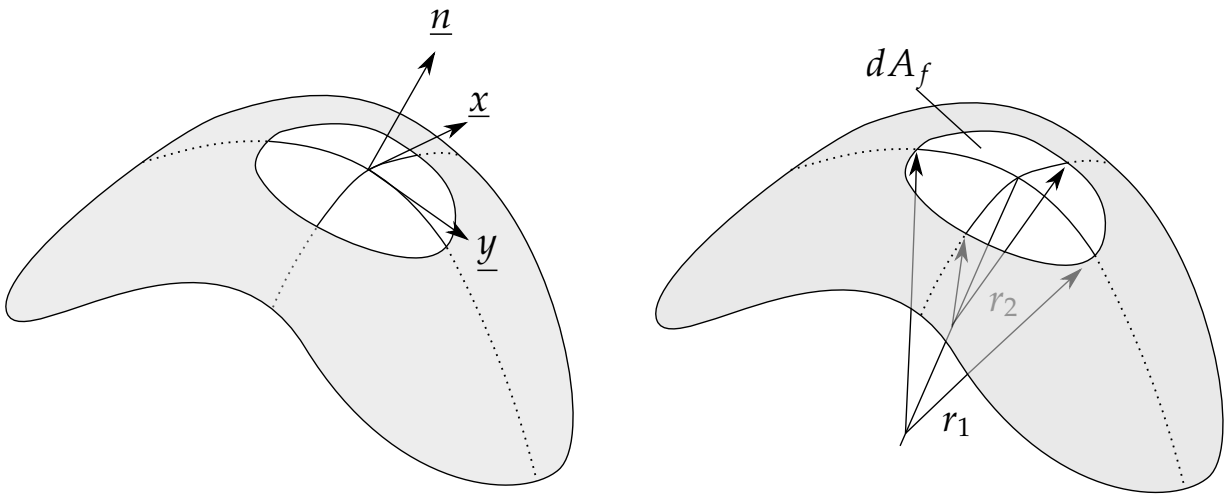

Figure 2.3.: Visualization of the local orthonormal basis on the left hand side and two radii describing curvature on the right hand side.

of Equation 2.42 express strain. Strain is defined as the volume change of a fluid element minus the part that is normal to the surface and can be interpreted as the flow acceleration in a plane that is parallel to the flame surface. The plane can be defined by two vectors $\underline{x}$ and $\underline{y}$ as shown in Figure 2.3. Equation 2.42 can then be rewritten:

$$\kappa = (\underline{x} \otimes \underline{x} + \underline{y} \otimes \underline{y}) : \nabla \underline{u} + s_d \nabla \cdot \underline{n} \ . \tag{2.43}$$

As depicted on the right hand side of Figure 2.3, curvature of the flame front can be described by two radii:

$$\kappa = (\underline{x} \otimes \underline{x} + \underline{y} \otimes \underline{y}) : \nabla \underline{u} - s_d \left(\frac{1}{r_1} + \frac{1}{r_2} \right) \ . \tag{2.44}$$

2.3.3. Premixed Flames in Turbulent Conditions

As mentioned before, turbulence itself is complex, difficult to model and still not fully understood. This naturally also applies to the interaction of turbulence with chemistry in turbulent combustion. A prerequisite of combustion is mixing on the molecular level of unburnt and burnt material for premixed combustion or fuel and oxidizer for non-premixed combustion. The general understanding is that this mixing process oc-

curs at the interface of the smallest eddies. Between two eddies, steep species gradients occur leading to fast molecular diffusion. The question arises whether turbulence models that are developed for non-reactive conditions can be used to describe the turbulent mixing in reactive flows. Fortunately, experimental observations evidence the validity of classical scaling laws on which turbulence models are based, as stated by Peters [31]. Besides the turbulent mixing process, one may ask how the combustion process is altered by turbulence. In other words, how does chemistry in laminar combustion differ from chemistry in turbulent combustion. In order to answer this question, a closer look to the range of possible time scales occurring in combustion is useful. A well-stirred reactor is supplied by an unburnt combustible gas. The residence time can be adjusted by changing the reactor's volume in order to specify the degree of burnout at the reactor's outlet. In Figure 2.4, the reactor's temperature T_r is plotted as a function of the ratio between the reactor's residence time τ_r and the chemical time scale τ_{ch}:

$$Da_r = \frac{\tau_r}{\tau_{ch}} \tag{2.45}$$

Three branches indicate possible states of the reactor. At the lower branch, the system is prior to ignition and chemical time scales are vast as all reaction rates are close to zero. For increasing residence times or decreasing chemical time scales, the reactor's temperature slowly increases to the ignition temperature. After the ignition event, chemical time scales are shorter than the residence time and the reactor's temperature is immediately approaching the upper branch. This is based on the mechanism that the combustion chemistry and the corresponding temperature accelerate each other and states between ignition and quenching become unstable (·····). Time scales of turbulence are usually located between the slow times scales before ignition and the fast time scales of combustion (upper branch). Thus, overlapping of the time scales of combustion and turbulence is rare and the separation is reasonable, as discussed by Peters [31]. Almost all combustion models are based on this assumption as they implicitly or explicitly assume length and time scale separation in the inertial subrange. In other words, chemistry in laminar combustion usually does not differ from chemistry in turbulent combustion. In order to prove the validity of the proposed time scale separation, the Borghi

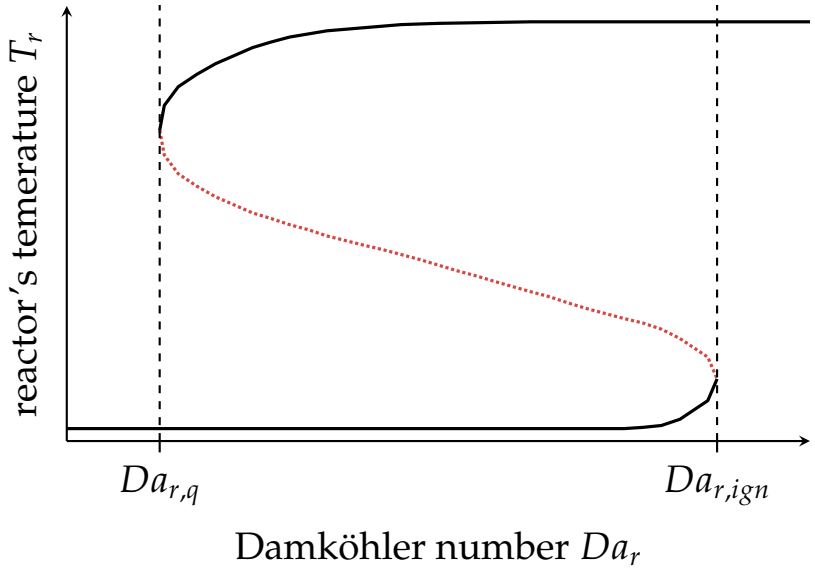

Figure 2.4.: Temperature in a well-stirred reactor as a function of Damköhler number (adapted from Peters [31]).

diagram [47] is introduced that is shown in Figure 2.5. It characterizes turbulence-chemistry interaction by comparing integral scales of turbulence and combustion. The x-axis measures the ratio of integral length scale l_{int} to flame thickness l_f. Furthermore, the y-axis represents the ratio of laminar flame velocity s_l to the root-mean-square (RMS) velocity u'.

A first characterization is done by the Reynolds number Re:

$$Re = \frac{u' l_{int}}{\nu} \ . \tag{2.46}$$

The laminar region in the lower left corner is defined by $Re < 1.0$ and is not of particular interest since most technical applications are turbulent.

As already mentioned, combustion usually takes place at fast time scales leading to thin reaction zones that are usually smaller than all turbulent scales. In order to determine if this statement is valid, the turbulent Karlovitz number Ka_t is a useful quantity. It compares the laminar flame thickness l_f with the diameter of the smallest eddies η:

$$Ka_t = \frac{l_f^2}{\eta^2} \ . \tag{2.47}$$

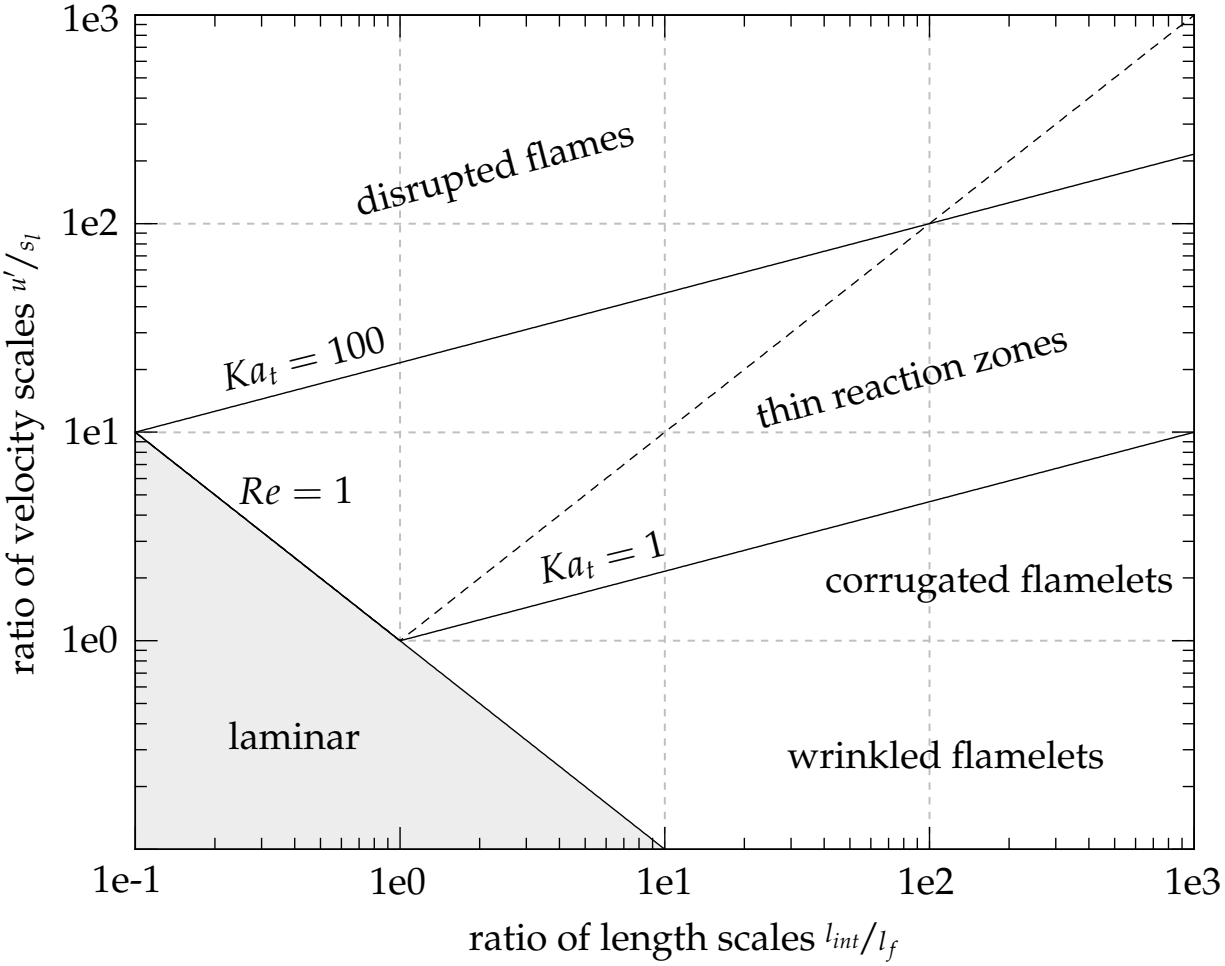

Figure 2.5.: Classification of turbulence-chemistry interaction in the Borghi diagram (adapted from Peters [31] as well as Poinsot and Veynante [28]).

The idea behind this comparison is illustrated in Figure 2.6. Based on Ka_t, three regions in the Borghi diagram are identified:

- **Corrugated and wrinkled flamelets:** If Ka_t is below unity, the smallest eddies do not penetrate the flamelets. Nevertheless, aerodynamic interactions may occur, leading to wrinkling and stretching of the flame sheet.

- **Thin reaction zones:** For values of Ka_t that are above unity, eddies penetrate the flame and interact with the preheat zone. As a consequence, the flame front is thickened. Note that the criterion $Ka_t > 1$

does not mean that eddies penetrate the reaction layer that is usually much smaller than the flame thickness. As long as the smallest eddies do not penetrate the reaction layer, the flame trajectories of temperature and species retain their laminar character.

- **Disrupted Flame:** Eddies are small enough to penetrate the reaction layer for Karlovitz numbers that are greater than 100. The reaction layer looses its laminar character and cannot be described by laminar flamelets anymore[4].

After discussing the influence of turbulence on combustion, it is worth noting that combustion also impacts the turbulent state of the flow. For example, the density drop due to combustion leads to an acceleration that generates turbulence.

2.3.4. Premixed Combustion Models

This section discusses the modeling of premixed combustion. A great number of combustion models exists that cannot be holistically covered in the scope of this work. In general, combustion modeling greatly depends on the way turbulence is modeled. A full resolution of all turbulent scales (DNS) in combination with the transport of all species with detailed chemistry, would not require to model combustion as the interaction of chemistry and turbulence is fully described. However, DNS in general is resource intense and the combination with detailed chemistry significantly increase computational costs. The use of reactive DNS is hence limited to few academic cases.

In the context of RANS and LES, the smallest scales are not resolved and the interaction with chemistry needs to be modeled. This section focuses on concepts that are formulated for RANS but can also be used in LES by considering minor modifications. More details regarding the characteristics of combustion modeling in the context of LES can be found by Poinsot and Veynante [28].

[4] The value of 100 is based on the assumption that the reaction layer thickness is one tenth of the total flame thickness.

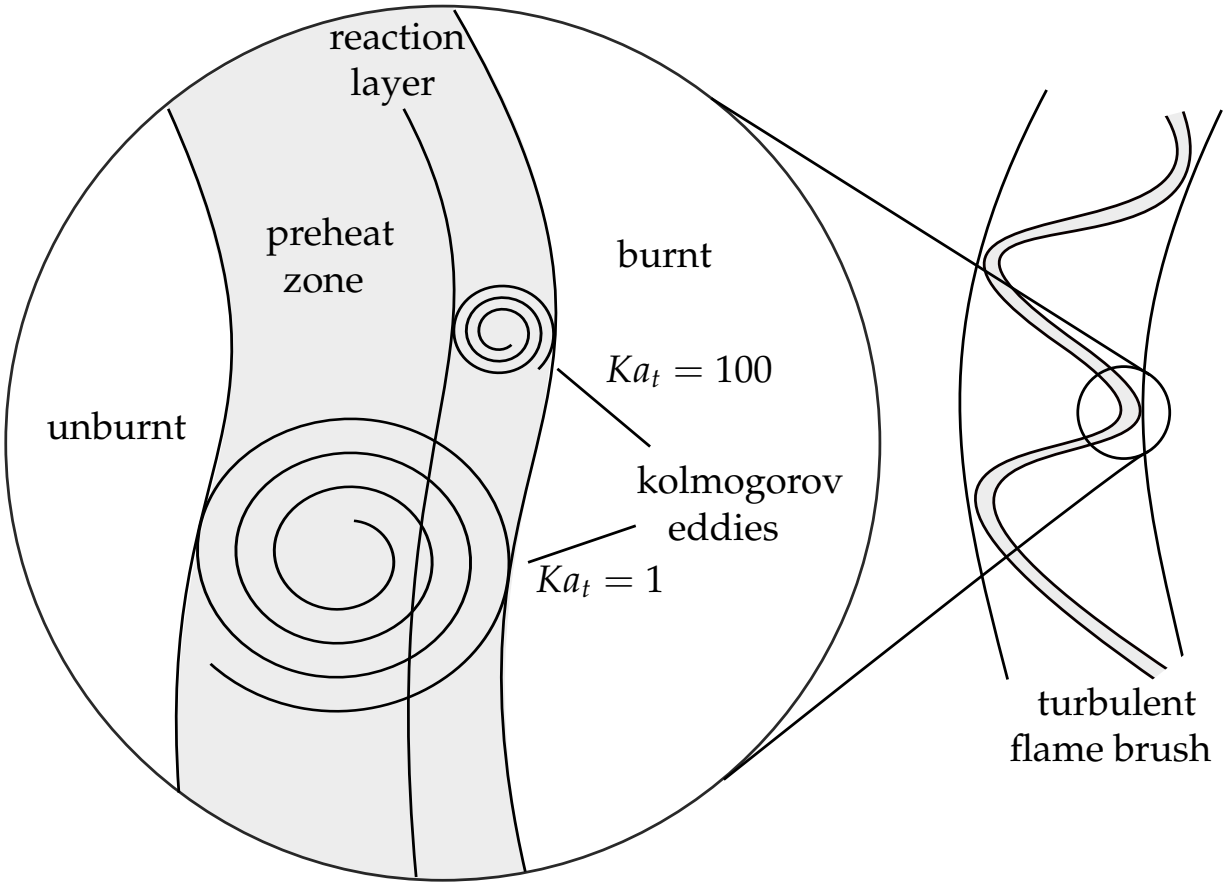

Figure 2.6.: Visualization of the interaction of eddies with a flame front.

In the following, a selection of three different combustion models are introduced. The first two models are based on the transport of species and differ significantly in the way the species source terms are closed. While the first model assumes that only chemical finite rates (FR) are the limiting factor, the second model states that turbulent mixing is always slower than all chemical scales. Furthermore, the Turbulent Flame Speed Closure (TFC) is introduced that is based on the transport of control variables instead of species. Note that the first model (FR) is introduced for didactic reasons only while the second and third model are used to benchmark the in Chapter 3 introduced combustion modeling strategy.

Note that some popular models are not covered in this section. For instance, the concept of Probability Density Functions (PDF) to describe the distribution of species and/or reaction progress is subject of Chapter 3. Two other worth mentioning models are the Bray Moss Libby concept

and the Flame Surface Density Model. An introduction to these models can be found by Poinsot and Veynante [28].

2.3.4.1. Finite Rate

Assuming that chemistry is the limiting rate, the most intuitive approach would be to close the ensemble-averaged species source term $\overline{\dot{\omega}_s}$ by summing up all corresponding reactions:

$$\overline{\dot{\omega}_s} = \sum_{r=1}^{\mathcal{R}} \dot{\omega}_{r,s} \tag{2.48}$$

The problem with this closure is not easy to grasp but important to note in the scope of the present work. Equation 2.48 closes the ensemble-averaged species source term by a chemical model that does not consider any fluctuations of temperature and species. Mean values, like the Favre-averaged temperature, represent a variety of different instantaneous physicochemical states. In specific situations, high variances may even indicate that the statistical probability for the mean value is close to zero. It is hence questionable to calculate a species source term with averaged quantities in a model that requires instantaneous values. The evaluation of the source term would only be valid if one or both of the following conditions are true:

1. The source term as a function of temperature and species have a linear character.

2. Fluctuations are close to zero.

Both conditions are usually not present in turbulent combustion processes.

2.3.4.2. Eddy Break-Up Model

The Eddy Break-Up (EBU) model published by Spalding [48, 49] states that combustion is solely a function of turbulence for the often valid assumption of high Reynolds and Damköhler numbers. The idea is that

turbulent eddies transport either burnt or unburnt gases and that mixing of both materials solely scales with the time scales of turbulent mixing. The source term for a product species s reads

$$\overline{\dot{\omega}_s} = \overline{\rho} C_{ebu} \frac{\epsilon}{k} \sqrt{\overline{Y_s''^2}} \ . \tag{2.49}$$

The EBU model is popular due to its simplicity and often leads to more accurate results than the FR model, as mentioned by Poinsot and Veynante [28]. However, Peters [31] states that the use of EBU often requires excessive model tuning to achieve accurate heat release distributions. Due to the negligence of possible finite rate limitations, EBU is not able to consider the impact of various equivalence ratios ϕ or different fuel compositions. It is evident that the prediction of the critical equivalence ratio for lean blowout by EBU is not advisable.

A qualitative comparison of the ensemble-averaged reaction rate predicted by EBU (—) and FR (·····) can be found in Figure 2.7. The intense peak from the FR model is characteristic due to the previously discussed self-accelerating character of combustion after the temperature has reached a critical value. Moreover, EBU solely scales with the fluctuation of the product mass fraction that has a maximum when the Favre-averaged temperature is increased by 50 % of the total temperature elevation.

The Eddy Dissipation Model (EDM) is an improved version of EBU by Magnussen and Hjertager [50]. In EDM, the variance $\overline{Y_s''^2}$ is replaced by the mean species mass fraction in order to consider the influence of equivalence ratio.

2.3.4.3. Turbulent Flame Speed Closure

The flamelet theory assumes that chemistry is fast leading to infinitely thin reaction zones. Furthermore, the flamelet is fluctuating in a zone that is called the turbulent flame brush as illustrated in Figure 2.6. Note that the flamelet fluctuations are transient and depend on turbulent structures that are not resolved in RANS simulations. RANS do rather resolve the statistical mean of the reaction progress in order to determine the position

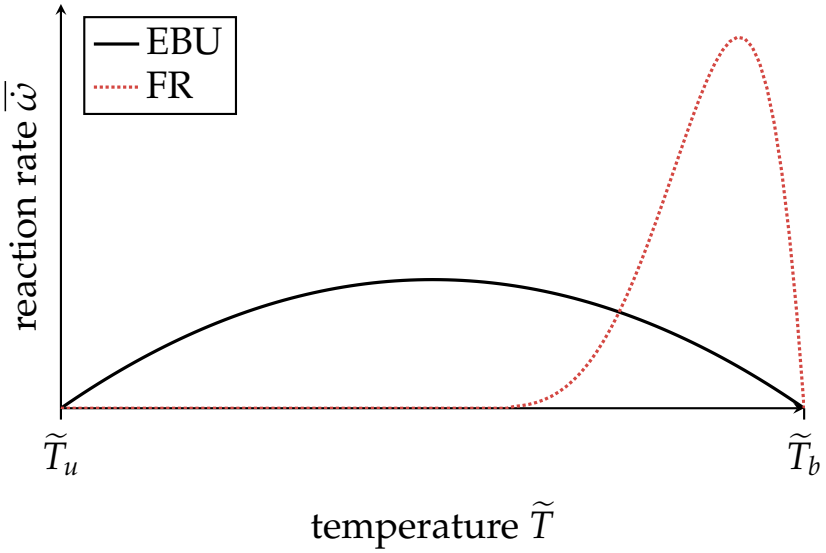

Figure 2.7.: Demonstration of typical reaction rate profiles by FR and EBU (adapted from Poinsot and Veynante [28]).

of the turbulent flame brush. Control variables like the reaction progress are generally evaluated by transport equations. The transport equation of the Favre-averaged reaction progress in the context of RANS reads

$$\frac{\partial \overline{\rho}\widetilde{c}}{\partial t} + \frac{\partial \overline{\rho}\tilde{u}_i\widetilde{c}}{\partial x_i} = \frac{\partial}{\partial x_i}\left(\frac{\mu_t}{Sc_t}\frac{\partial \widetilde{c}}{\partial x_i}\right) + \overline{\dot{\omega}_c} \ . \tag{2.50}$$

$\overline{\dot{\omega}_c}$ can be closed by TFC as introduced in the following. Figure 2.8 illustrates the wrinkling of a flame sheet that propagates with the laminar flame speed s_l. In addition, the statistical mean of the flame front is depicted that propagates with the turbulent flame speed s_t and can be evaluated using

$$\frac{s_t}{s_l} = \frac{A_t}{A_l} \ . \tag{2.51}$$

The turbulent flame speed s_t can be interpreted as the speed of the turbulent flame brush that is defined by the reaction progress variable c. Thus, s_t can be employed to close the ensemble-averaged reaction progress source term $\overline{\dot{\omega}_c}$:

$$\overline{\dot{\omega}_c} = \rho_u s_t \frac{\partial \tilde{c}}{\partial x_i} \ . \tag{2.52}$$

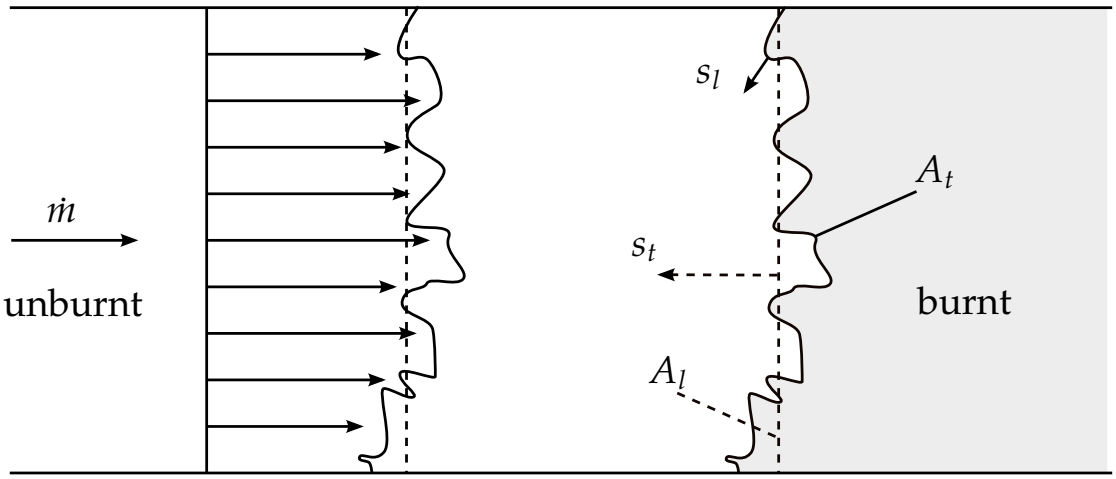

Figure 2.8.: Visualization of the turbulent flame velocity (adapted from Peters [31]).

Furthermore, Zimont et al. [51,52] suggests to close s_t using the following equation:

$$s_t = C_{tfc} \frac{u'^{\frac{3}{4}} s_l^{\frac{1}{2}} l_{int}^{\frac{1}{4}}}{D_{th}^{\frac{1}{4}}} \ . \tag{2.53}$$

The question arises how the knowledge of the averaged reaction progress variable $\tilde{c}$ can be used to evaluate the physicochemical state of the flow. A possible solution is to simply interpolate quantities between the unburnt and burnt state. This approach is only valid for quantities that feature a linear trajectory over the reaction progress. Most technically important quantities like temperature or the mass fractions of fuel and oxidizer can be assumed to have a linear profile over the reaction progress. However, linear interpolation cannot be used for intermediate species like CO that take values of zero in the unburnt state, equilibrium in the burnt state, and a high peak value during combustion as it was shown in Figure 2.2. Exact trajectories of intermediate species are of great importance for this work. Hence, the next chapter presents a combustion model that is capable of retrieving quantities from one-dimensional flamelets.

3 Modeling Combustion

A combustion model is presented in this chapter that is designed to feature high accuracy in cold conditions. The modeling strategy is based on FGM that was initially proposed by van Oijen et al. [53, 54]. An introduction to FGM for the application in turbulent, partially-premixed conditions is given in the first section of this chapter. Moreover, Section 3.2 presents a novel approach to efficiently consider flame stretch and heat loss. In Section 3.3, the developed models are applied to an atmospheric single-burner test rig in order to validate the numerically predicted heat release distribution. The chapter concludes with Section 3.4 in which standard combustion models are compared with the proposed modeling strategy.

3.1. Flamelet Generated Manifolds

The basic principle of FGM is to look up physicochemical quantities in tables that are generated by one-dimensional flamelet simulations based on detailed chemistry and advanced diffusion models. The tables are parametrized by control variables that must be evaluated by additional transport equations. FGM has advantages in comparison to other chemistry reduction methods like the Intrinsic Low-Dimensional Manifolds (ILDM) model by Maas and Pope [55] as stated by van Oijen [54]. ILDM uses the steady-state assumption for fast reactions and can thus be inaccurate in cold regions that are limited by slow chemistry. Furthermore, a decisive advantage of FGM is that species trajectories are accurately described by the flamelet-generated manifolds. This is of great importance for this work, as the modeling of CO is based on the correct representation of intermediate species within the turbulent flame brush. An application of FGM to partially-premixed combustion can be found by Ramaekers et al. [56]. In partially-premixed combustion with binary mixtures, the com-

bination of the reaction progress variable c and the mixture fraction f is a reasonable choice. In general, a Favre-averaged control variable $\widetilde{\theta}$ can be transported using

$$\frac{\partial \overline{\rho}\widetilde{\theta}}{\partial t} + \frac{\partial \overline{\rho}\tilde{u}_i\widetilde{\theta}}{\partial x_i} = \frac{\partial}{\partial x_i}\left(\frac{\mu_t}{Sc_t}\frac{\partial \widetilde{\theta}}{\partial x_i}\right) + \overline{\dot{\omega}_\theta} \ . \tag{3.1}$$

As mentioned before, the transport of the reaction progress $\tilde{c}$ requires modeling of the source term $\overline{\dot{\omega}_c}$. In the context of FGM, $\overline{\dot{\omega}_c}$ is retrieved from manifolds. The look up of tabulated quantities by solely using Favre-averaged control variables would be inaccurate due to the non-linear character of combustion chemistry as discussed in Section 2.3.4.1. The turbulent fluctuations of the control variables require to consider every possible state with its respective probability. For this purpose, PDFs $\mathcal{P}$ are used to describe the statistical distribution of the control variables. The statistical mean of a looked-up quantity results from the integration of the product of the scalar and its statistical distribution:

$$\overline{\dot{\omega}_c^0} = \iint \dot{\omega}_c^0(c,f)\mathcal{P}(c,f)\,dc\,df \ . \tag{3.2}$$

Joint PDFs of statistically independent control variables can be calculated by multiplying the corresponding marginal PDFs. A marginal PDF is the distribution of a single control variable. Assuming that c and f are independent, the joint PDF can be calculated using:

$$\mathcal{P}(c,f) = \mathcal{P}(c)\mathcal{P}(f) \ . \tag{3.3}$$

Various strategies for determining marginal PDF shapes for scalars in turbulent flows have been published. One option is to presume a specific function for the PDF. The shape of this function can be modeled using the mean and the variance of the control variable (first two conditional moments):

$$\overline{\dot{\omega}_c^0}(\tilde{c},c'',\tilde{f},f'') = \iint \dot{\omega}_c^0(c,f)\mathcal{P}(c,\tilde{c},c'')\mathcal{P}(f,\tilde{f},f'')\,dc\,df \ . \tag{3.4}$$

The variances c'' and f'' are usually evaluated by additional transport equations. It is important to note that presumed PDFs are a significant simplification since the actual distribution may substantially differ from

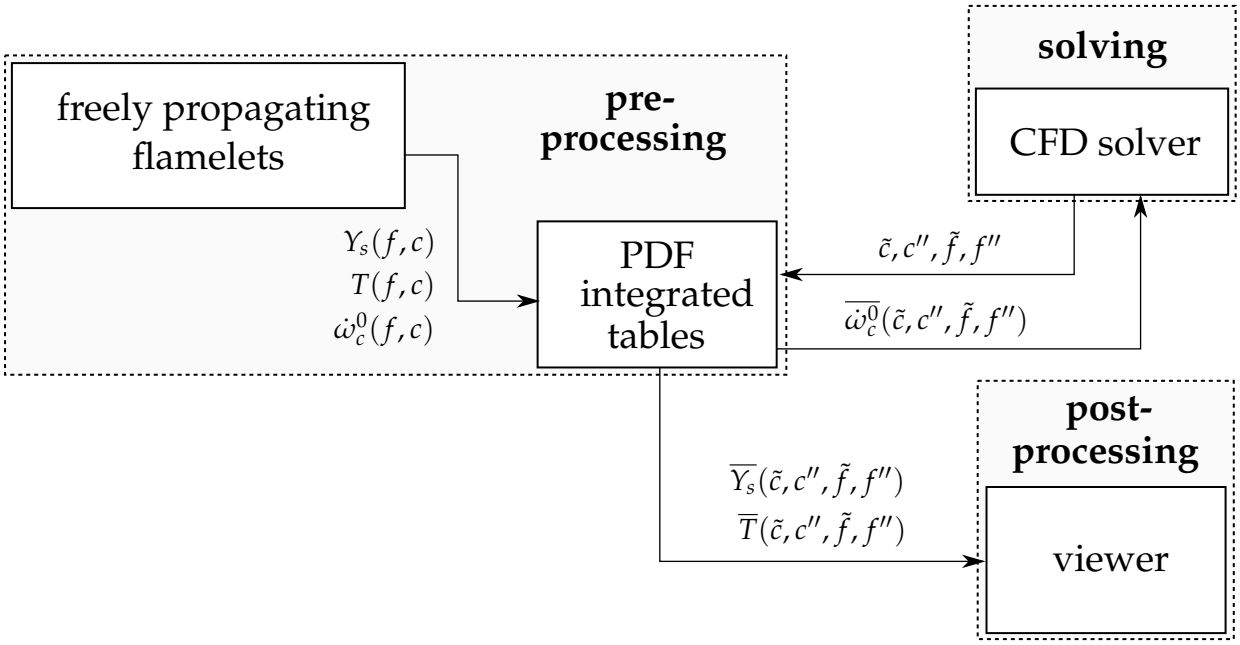

Figure 3.1.: Simplified overview of the classical FGM.

the presumed shape as mentioned by Poinsot and Veynante [28]. In the present work, Eulerian beta functions are employed to model the shape of PDFs. Beta functions feature asymmetrical, parabolic shapes as well as potential singularities[1] at the boundaries for high variances or at the mean value for low variances.

An overview of the flow of information in the classical FGM is given in Figure 3.1. Prior to the solving process, freely propagating flamelets are used to evaluate species mass fractions Y_s, temperature T, and the reaction progress term $\dot{\omega}_c^0$ as a function of reaction progress c for a predefined set of mixture fractions f. Moreover, the profiles are PDF integrated (Equation 3.4) and stored in tables. During runtime, the solver looks up the required averaged reaction progress source term $\overline{\dot{\omega}_c^0}$ on the basis of the first two conditional moments of both control variables $(\tilde{c}, c'', \tilde{f}, f'')$.

In the following, the applicability of FGM in the context of gas turbines is discussed. FGM is based on the assumption that physicochemical trajectories of freely-propagating flamelets are equal to flamelets that propagate in turbulent flows. This assumption is only justified when the

[1] One may ask how the integration of a function that features singularities is possible. A comprehensive study of an approximate method to integrate Eulerian beta functions can be found by Liu et al. [57].

smallest turbulent scales are larger than the reaction layer. In order to test the validity of this assumption, gas turbines and the employed validation case by Marosky [58] are investigated using the Borghi diagram. This approach requires the estimation of scales that describe combustion and turbulence. Velocity and thicknesses of flamelets are obtained from one-dimensional calculations. Furthermore, turbulent scales are determined in a CFD simulation of the validation case. Note that the burner size and flow velocity of Marosky's validation case is comparable to real gas turbine combustors. It is hence reasonable to assume that similar integral length scales and RMS velocities occur in gas turbines. In this study, gas turbines are considered to operate in a range of equivalence ratios between $\phi = 0.5$ to $\phi = 0.8$ and pressures between $p = 15\,\text{bar}$ to $p = 30\,\text{bar}$. Furthermore, the ranges of pressure and equivalence ratio are each discretized by four points resulting in a grid of 16 operating points. The estimated scales are summarized in Table 3.1 and plotted in Figure 3.2. The atmospheric validation case is located in the thin reaction zones regime. Peters [31] states that the one-dimensional laminar character of the flamelet is not altered in the thin reaction zones regime. This is due to the fact that eddies are too large to penetrate the reaction layer. Moreover, the specified operational window of gas turbines is almost entirely in the thin reaction zones regime and solely crosses the $Ka_t = 100$ limit in lean conditions at low pressure, as depicted in Figure 3.2. Note that the $Ka_t = 100$ line should not be seen as a strict criterion for flamelet disruption as mentioned by Peters [59]. It can be concluded that the use of flamelets to describe combustion is valid for the investigated conditions.

3.2. Modeling Flame Stretch and Heat Loss

The classic way of employing freely-propagating flamelets for the generation of manifolds may be problematic when it comes to flame stretch as mentioned by van Oijen and de Goey [60]. Furthermore, non-adiabatic effects may also have a significant impact on the combustion process. Both effects are not considered in the original formulation of FGM. Donini et al. [61, 62] present an example for the extension of the look up table to take heat loss into account. Unfortunately, the addition of further dimensions

Table 3.1.: Overview of estimated scales that occur in gas turbines and in Marosky's [58] validation case.

	$\phi = 0.5$		$\phi = 0.8$			
	s_l in cm/s	l_f in µm	s_l in cm/s	l_f in µm	l_{int}	u'
validation case at 1 bar	57	560	-	-	7.1 mm	13.3 m/s
gas turbine at 15 bar	15	130	52	49		
gas turbine at 30 bar	22	69	68	24		

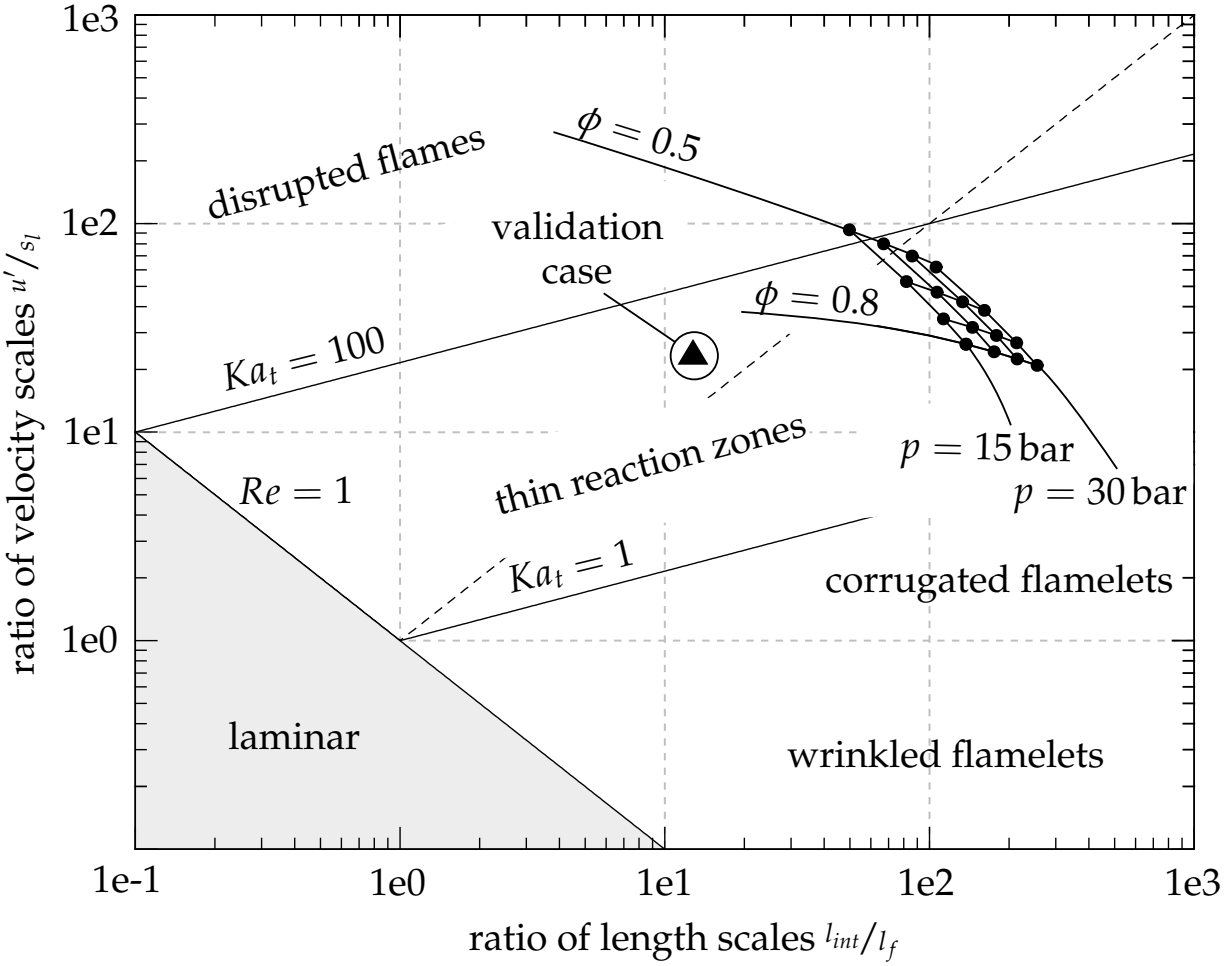

Figure 3.2.: Justifying the flamelet theory for Marosky's [58] validation case as well as for gas turbines (Borghi diagram adapted from Peters [31] and from Poinsot and Veynante [28]).

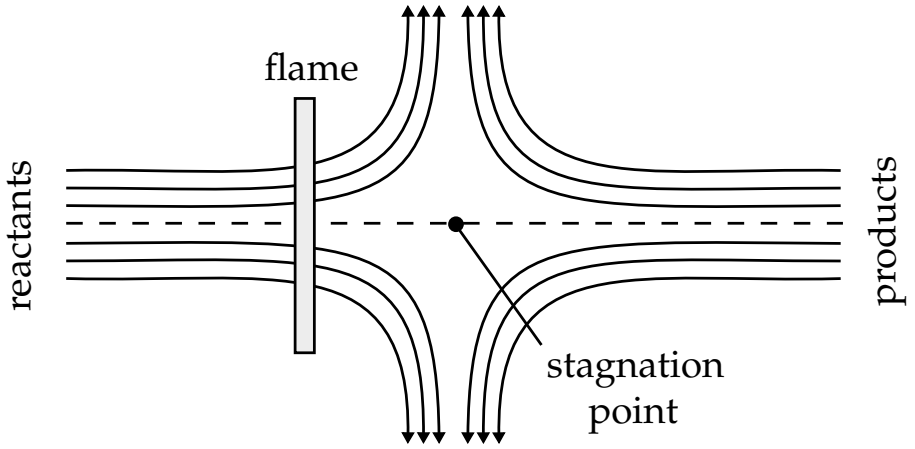

Figure 3.3.: Illustration of a premixed counterflow flame.

to the tabulation process leads to a significant increase in table size, which severely limits the practical usability. Hence, a new method to efficiently consider flame stretch and heat loss using two manifolds instead of one is introduced in the following. In order to manipulate the unstretched, adiabatic closure of the classic FGM, a correction factor Γ that is a function of the fuel consumption speed s_c is introduced:

$$\overline{\dot{\omega}_c^*} = \Gamma_{\kappa,\psi}(\kappa, \psi, \tilde{f}) \iint \dot{\omega}_c^0(c, f)\mathcal{P}(c, \tilde{c}, c'')\mathcal{P}(f, \tilde{f}, f'')\, dc\, df\,. \tag{3.5}$$

The modeling of Γ on the basis of fuel consumption speeds s_c, is inspired by a methodology that was published by Tay et al. [63–65]. In the described approach, the laminar flame speed of a TFC closure is simply replaced by the fuel consumption speed s_c of a premixed counterflow flame. Note that s_c is the fuel consumption speed that is defined by the following equation (cf. Poinsot and Veynante [28]):

$$s_c = \frac{-1}{\rho_u Y_{fuel,u}} \int_{-\infty}^{+\infty} \dot{\omega}_{fuel}\, dx\,. \tag{3.6}$$

In order to evaluate the influence of strain on the fuel consumption speed s_c, one-dimensional premixed counterflow flamelets are usually employed. The premixed counterflow flamelet configuration has two opposed flows of an unburnt and a burnt flow as illustrated in Figure 3.3.

Equilibration[2] of the reactants is accomplished in order to determine the thermodynamic state of the burnt gas. The laminar flame speed s_l equals the fuel consumption speed s_c for zero strain rates and without heat loss. A decisive advantage of s_c over s_l is that s_c can be evaluated in premixed counterflow flames at elevated stretch rates while s_l is ambiguous in premixed counterflow flames. This is due to the fact that s_l is defined as the flow velocity that approaches the flame front (as described in Section 2.3.1) which cannot be evaluated in premixed counterflow flamelets as the approaching flow is not constant in terms of velocity. In this work, simulations of premixed counterflow simulations are performed with the open-source software CANTERA by Goodwin et al. [34]. Note, that CANTERA employs SUNDIALS by Hindmarsh et al. [66], which is a solver for Ordinary Differential Equations (ODE). In freely propagating flamelets, the velocity is constant as long as the density is not decreased by the heat release as depicted in Figure 2.2. In contrast to a freely propagating flamelet, the velocity profile in a counterflow configuration is ambiguous (even before the heat release zone) and the evaluation of s_l hence not possible.

The idea of modeling Γ on the basis of s_c is to divide the reaction progress source term by the unstretched, adiabatic flame speed s_c^0 and to multiply the stretched, non-adiabatic flame speed s_c^*:

$$\Gamma_{\kappa,\psi}(\kappa,\psi,\tilde{f}) = \left(\frac{s_c^*\left(\kappa,\psi,\tilde{f}\right)}{s_c^0\left(\tilde{f}\right)} \right)^{m_{\kappa,\psi}} . \tag{3.7}$$

The superscript * denotes the stretched, non-adiabatic state, while ^{0} denotes the reference state without flame stretch or heat loss. s_c^* deviates[3] from the laminar flame speed, as flame stretch has an impact on molecular diffusion. This is caused by strain that steepens the profiles of temperature and species in the flame front. On the one hand, reactivity increases due to higher fuel diffusion from the unburnt mixture towards the flame front. On the other hand, the temperature of the reaction layer decreases as more heat diffuses towards the cold, unburnt material that leads to a

[2] The combustion process in gas turbine combustors can be assumed to occur at constant pressure. Hence, the equilibrium is determined by assuming an isobaric transition at constant enthalpy.

[3] Note that there are situations in which flame stretch does not lead to an alteration of the flame speed when thermal cooling of the flame front cancel outs the accelerating effect due to increased fuel diffusion.

reduction of the fuel consumption speed. This mechanism is implicitly expressed by the exponent $m_{\kappa,\psi}$ in Equation 3.7. $m_{\kappa,\psi}$ describes the proportionality between the fuel consumption speed s_c^* and the ensemble-averaged reaction progress source term $\overline{\dot{\omega}}_c^*$ for variable flame stretch rates and heat losses:

$$s_c^*(\kappa,\psi,\tilde{f})^{m_{\kappa,\psi}} \propto \overline{\dot{\omega}_c^*}(\kappa,\psi,\tilde{f},f'',\tilde{c},c'') \,. \tag{3.8}$$

This proportionality is complex and difficult to model. Thus, the simplification is introduced that $m_{\kappa,\psi}$ can be determined by assuming proportionality between s_c^* and the peak value of the reaction progress source term $\dot{\omega}_{c,max}^*$ before PDF integration is performed:

$$\begin{aligned} s_c^*(\kappa,\psi,\tilde{f})^{m_{\kappa,\psi}} &\propto \dot{\omega}_{c,max}^*(\kappa,\psi,\tilde{f}) \\ \rightarrow m_{\kappa,\psi} &\propto \frac{\log(\dot{\omega}_{c,max}^*(\kappa,\psi,\tilde{f}))}{\log(s_c^*(\kappa,\psi,\tilde{f}))} \,. \end{aligned} \tag{3.9}$$

The logarithm of the maximum value of the reaction progress source term is plotted versus the logarithm of the fuel consumption speed in Figure 3.4. The data points are determined by a set of premixed counterflow flamelets that equal in reactants temperature T_u, pressure p, and equivalence ratio ϕ and solely differ in strain that can be adjusted by varying the velocity of educts and products. The used boundary conditions of the flamelets are based on values that are averaged over the turbulent flame brush in a simulation of Maroskys test rig that is used for validation purposes below in Section 3.3 and 3.4. Note that the conclusions that are derived in the following, are not limited to the employed conditions but are valid for all validation cases that are shown in this work. An import finding is that the connection of $\log(\dot{\omega}_{c,max}^*)$ as a function of $\log(s_c^*)$ has a linear character and $m_{\kappa,\psi}$ is hence constant for varying strain rates. After showing that $m_{\kappa,\psi}$ does not depend on strain rates, the question arises whether $m_{\kappa,\psi}$ varies for different heat losses ψ or equivalence ratios ϕ. Figure 3.5 provides an answer by showing a plot of $m_{\kappa,\psi}$ over ϕ for different heat losses. Note that $m_{\kappa,\psi}$ is evaluated for each data point by a set of flamelets at different strain rates at the specified heat loss ψ and equivalence ratio ϕ. As one can see, the profiles of $m_{\kappa,\psi}$ diverge for mixture fractions below $\phi = 0.26$. The scatter of $m_{\kappa,\psi}$ only occurs for reactivities that are close to zero and are hence not relevant for the combustion model. Reactivity

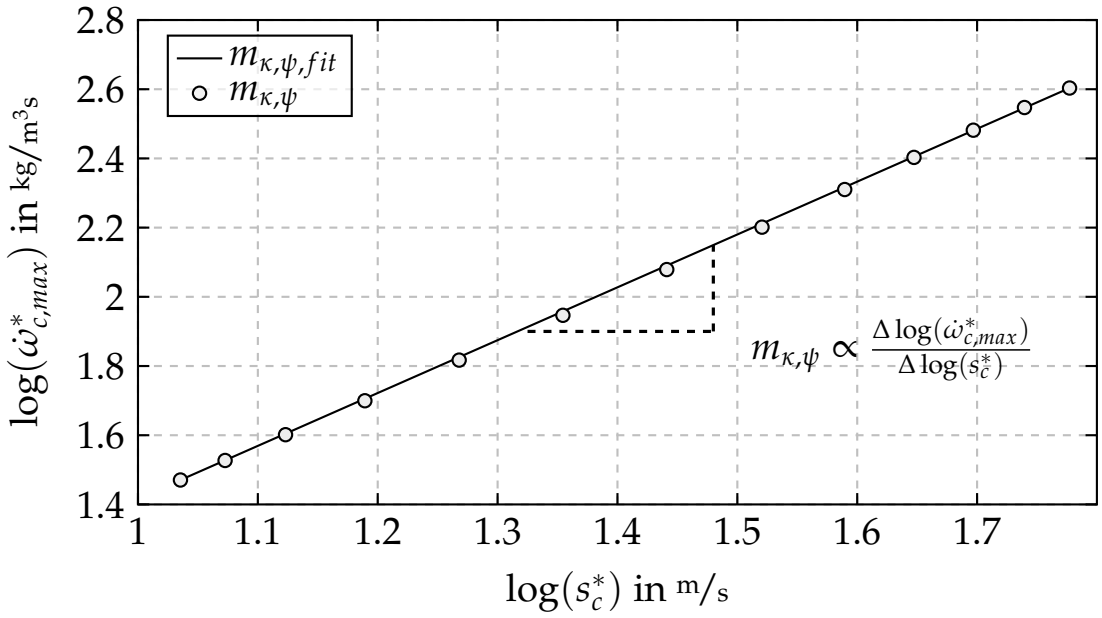

Figure 3.4.: Demonstration of the constant character of $m_{\kappa,\psi}$.

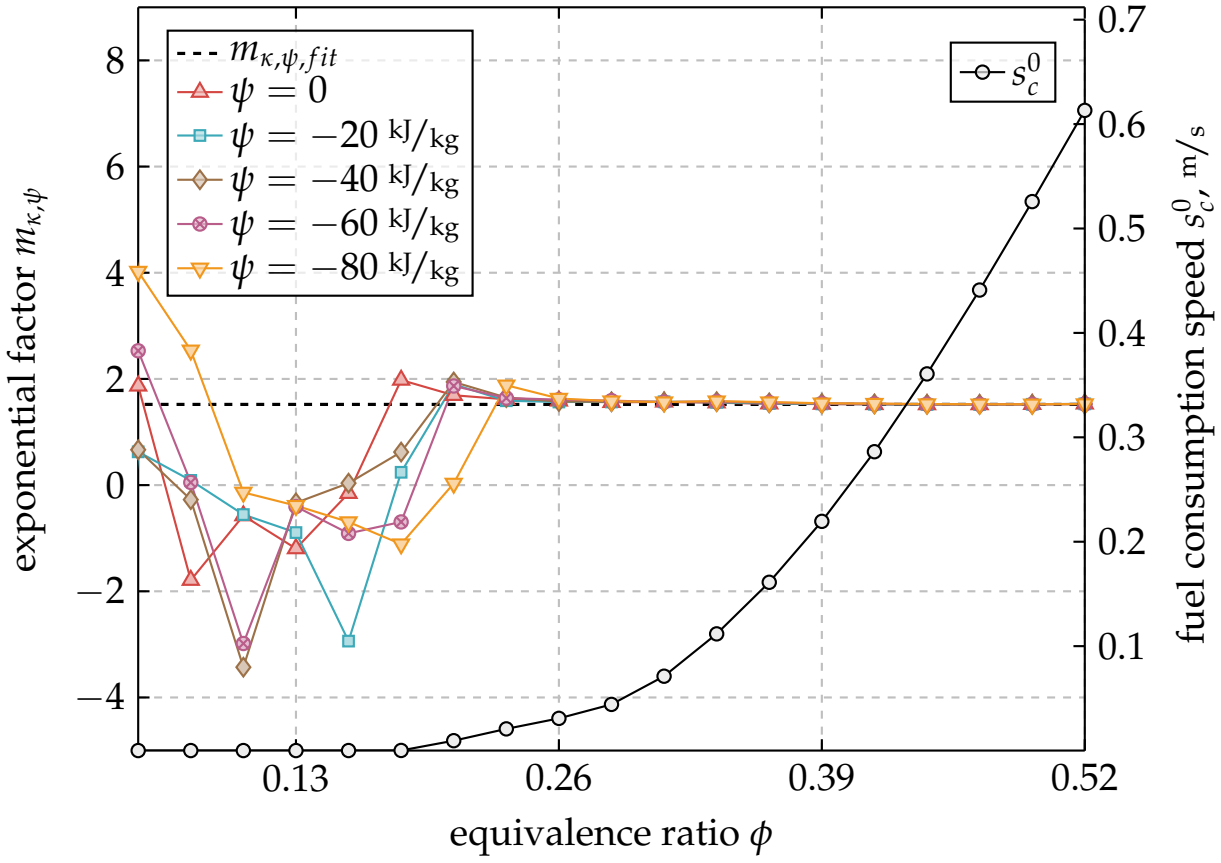

Figure 3.5.: Demonstration of the independence of $m_{\kappa,\psi}$ from equivalence ratio ϕ and heat loss.

is indicated by the fuel consumption speed s_c, which is plotted using a second y-axis.

Based on the conclusions that are derived from Figure 3.4 and Figure 3.5, a constant value for the proportionality exponent $m_{\kappa,\psi}$ can be considered. The assumption of using a constant proportionality exponent $m_{\kappa,\psi}$ has a great advantage, as a further tabulation strategy for $m_{\kappa,\psi}$ as a function of mixture fraction f and heat loss ψ is not necessary. The proportionality exponent $m_{\kappa,\psi}$ is determined once at an arbitrary mixture fraction and heat loss (within the flammability limits) as the gradient of a fitted linear equation. The resulting flow of information for the described model is given in Figure 3.6. During run time, the code looks up unstretched, adiabatic fuel consumption speeds s_c^0 as well as stretched, non-adiabatic fuel consumption speeds s_c^*. Significant heat losses and elevated flame stretch rates cause the fuel consumption speed s_c^* to deviate from s_c^0. This results in a change of the correction factor Γ that implicitly affects the reaction progress source term and the shape of the turbulent flame brush. Differences in comparison to the original FGM, which is depicted in Figure 3.1, are as follows:

- PDF integrated tables that provide mass fractions Y_s, temperature T and the reaction progress source term $\overline{\dot{\omega}_c^0}$ are based on counterflow flamelets at negligible stretch and adiabatic conditions instead of freely propagating flamelets.

- Further tables are required that store the fuel consumption speeds s_c^0 and s_c^* as well as the proportionality factor $m^{\kappa,\psi}$. During run time, the code looks up correction factors as a function of mixture fraction f, stretch κ, and heat loss ψ.

The introduced FGM model extension requires to evaluate stretch and heat loss in premixed counterflow flamelets, which is discussed in the next Section 3.2.1. In addition, the determination of heat loss in CFD is discussed in Section 3.2.2 and the determination of stretch in the scope of RANS is discussed in Section 3.2.3.

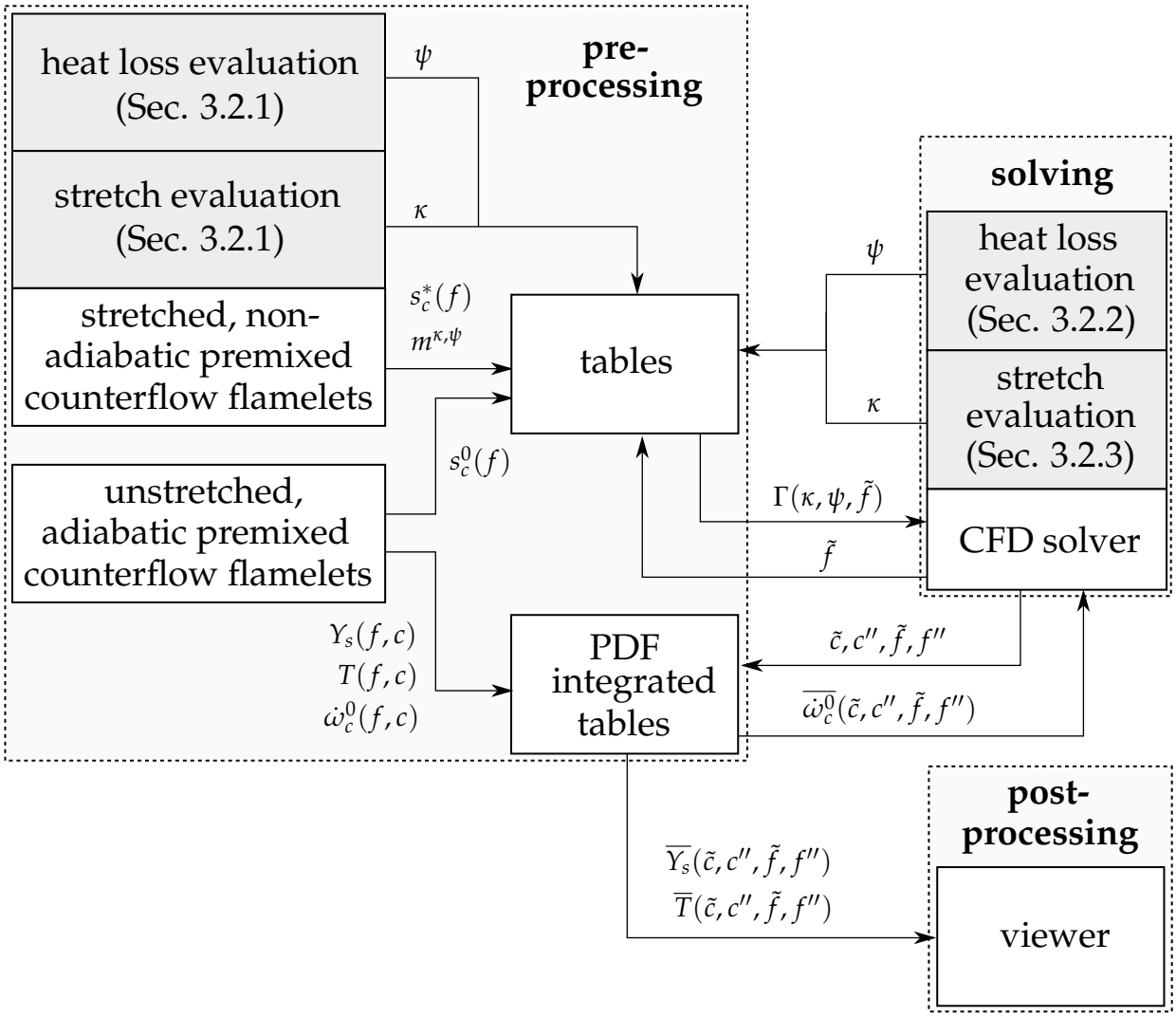

Figure 3.6.: Simplified overview of FGM that considers stretch and heat loss.

3.2.1. Determination of Stretch and Heat Loss in Premixed Counterflow Flames

As discussed in Section 2.3.2, flame stretch consists of strain and curvature. Unfortunately, premixed counterflow flamelets can only be simulated at elevated strain rates as curvature is not achievable due to the one-dimensional character of the flame. Thus, the tabulation of flamelets at various flame stretch rates is not possible. As stated by Poinsot et al. [28, 67], strain and curvature have a similar impact on the physicochemical properties of the flame, at least for small flame stretch rates. This hypotheses is exploited, as the tables for fuel consumption rates s_c are

parametrized with strain from the one-dimensional flamelet calculations and looked up with flame stretch (strain + curvature) that is evaluated in the context of RANS. Strain can be obtained from the one-dimensional velocity field using

$$\kappa_{st} = -\frac{\partial u_x}{\partial x} \ , \tag{3.10}$$

which is valid for incompressible flows due to the following relation:

$$0 = \frac{\partial u_x}{\partial x} + \underbrace{\frac{\partial u_y}{\partial y} + \frac{\partial u_z}{\partial z}}_{\kappa_{st}} \ . \tag{3.11}$$

The velocity profile in a premixed counterflow flamelet is not linear over space and strain differs for each location. Consequently, the location at which strain should be evaluated must be defined. Flame stretch alters the flame velocity by changing the diffusive heat and species exchange between the flame front and the unburnt material. It is thus reasonable to determine strain at the interface between reactants and flame front. This position is evaluated by identifying the grid point that is located right before the flow accelerates due to the expansion of gas caused by the density drop.

In order to determine the influence of heat loss, the manifolds must be parametrized by different levels of enthalpy. A non-adiabatic simulation would usually indicate that there is a source term in the energy equation that covers heat losses. Unfortunately, this would lead to several difficulties. For instance, the heat loss could not be defined but would result from the solution. Hence, the flamelet simulations are performed at a set of predefined enthalpy levels. A reduced enthalpy corresponds to heat loss and is obtained by changing the reactants temperature. Further information on the approach of employing flamelets at different enthalpy levels for non-adiabatic simulations is discussed by Fiorina et al. [68].

3.2.2. Modeling Heat Loss in the Context of CFD

Non-adiabatic effects are evaluated by a transport equation for energy. As mentioned before, different forms of the energy equation exists. Equation

2.11 is employed in the present work that transports the sum of chemical and sensible enthalpy (denoted as h). This form has the advantage to be conservative during the combustion process. Changes in the chemically-bonded enthalpy are fully converted into sensible enthalpy. Furthermore, heat loss ψ is the distance of the non-adiabatic enthalpy h to the adiabatic enthalpy h_{ad}:

$$\psi = h - h_{ad} \ . \tag{3.12}$$

Similar approaches can be found by Wetzel et al. [69] and by Frank et al. [70]. Adiabatic enthalpy needs to be determined as a function of mixture fraction. Enthalpy depends linearly on mixture fraction and can be evaluated using:

$$h_{ad} = h_1 f + h_0(1 - f) \ . \tag{3.13}$$

The indices $_1$ and $_0$ corresponds to a mixture fraction of unity (fuel) and zero (oxidizer).

3.2.3. Modeling Flame Stretch Rates in the Context of RANS

The fundamentals of flame stretch can be found in Section 2.3.2 in which the following equation is stated:

$$\langle \kappa_{st} \rangle = \underbrace{\nabla \cdot \underline{u} - \langle \underline{n} \otimes \underline{n} \rangle : \nabla \underline{u}}_{\kappa_{st}} + \underbrace{\langle s_d \nabla \cdot \underline{n} \rangle}_{\kappa_{curv}} \ . \tag{3.14}$$

Flame stretch is a continuous field and differs for each position of the flame front. Hence, the discrete flame surface that is located within a cell has a variety of different flame stretch rates. The models that are introduced in the following, determine cell-averaged flame stretch rates, which is indicated by $\langle\ \rangle$. Equation 3.14 shows the two parts flame stretch consists of. In the context of RANS, only the Favre-averaged velocity is known. Thus, it is reasonable to divide the strain term in order to model the first two conditional moments of velocity separately:

$$\langle \kappa_{st} \rangle = \underbrace{\nabla \cdot \underline{\tilde{u}} - \langle \underline{n} \otimes \underline{n} \rangle : \nabla \underline{\tilde{u}}}_{\tilde{\kappa}_{st}} + \underbrace{\langle \nabla \cdot \underline{u}'' - \langle \underline{n} \otimes \underline{n} \rangle : \nabla \underline{u}'' \rangle}_{\kappa''_{st}} + \underbrace{\langle s_d \nabla \cdot \underline{n} \rangle}_{\kappa_{curv}} \ . \tag{3.15}$$

In the next three sections, the modeling of each term is presented.

3.2.3.1. Modeling Mean Flame Stretch Rates

The mean flame stretch rate

$$\langle \tilde{\kappa}_{st} \rangle = \nabla \cdot \underline{\tilde{u}} - \langle \underline{n} \otimes \underline{n} \rangle : \nabla \underline{\tilde{u}} \tag{3.16}$$

in index notation reads

$$\langle \tilde{\kappa}_{st} \rangle = \left(\delta_{ij} - \langle n_i n_j \rangle \right) \frac{\partial \tilde{u}_i}{\partial x_j} \ . \tag{3.17}$$

The orientation factors $n_i n_j$ are unknown and require modeling. Veynante et al. [71,72] observed the following relationship between orientation factors and Reynolds stresses in a two-dimensional, V-shaped flame[4]:

$$\langle n_i n_{j=i} \rangle = \frac{\sum_{k \neq i} \tilde{u}_k''^2}{4k} \quad \text{and} \quad \langle n_i n_{j \neq i} \rangle = \frac{\widetilde{u_i'' u_j''}}{2k} \ . \tag{3.18}$$

The turbulent kinetic energy k can be retrieved from the turbulence model. Furthermore, the Reynolds stresses are estimated using the approximation by Boussinesq (cf. Equation 2.28).

3.2.3.2. Modeling Turbulent Flame Stretch Rates

$$\langle \kappa_{st}'' \rangle = \langle \nabla \cdot u'' - n \otimes n : \nabla u'' \rangle \tag{3.19}$$

Strain due to turbulent fluctuations is determined using the Intermittent Turbulence Net Flame Stretch (ITNFS) model proposed by Meneveau and Poinsot [74] on the basis of chemical and turbulent time and length scales:

$$\langle \kappa_{st}'' \rangle = \mathcal{I} \left(\frac{u'}{s_l}, \frac{l_{int}}{l_f} \right) \frac{\epsilon}{k} \ . \tag{3.20}$$

The function $\mathcal{I}$ is derived from a DNS in which the interaction of counter-rotating pairs with flame fronts is analyzed. An advantage over other

[4] Note that this model is also valid in three dimensions as demonstrated in a DNS by Katragadda et al. [73].

models is that ITNFS considers eddies of all turbulent scales. Moreover, ITNFS employs a model that describes the intermittent character of eddies to consider the probability distribution for the circumferential speed of an eddy of a specific size.

3.2.3.3. Modeling Flame Stretch Rates due to Curvature

Flame stretch due to curvature is defined by

$$\langle \kappa_{curv} \rangle = \langle s_d \nabla \cdot \underline{n} \rangle \quad . \tag{3.21}$$

The displacement speed s_d measures the speed of the flame front towards the reactants in normal direction $\underline{n}$. A commonly used approach is to replace the displacement speed s_d with the laminar flame velocity s_l:

$$\langle s_d \nabla \cdot \underline{n} \rangle \approx \langle s_l \nabla \cdot \underline{n} \rangle \approx \langle s_c^0 \nabla \cdot \underline{n} \rangle \quad . \tag{3.22}$$

Veynante et al. [72] proposes a model to evaluate $\nabla \cdot \underline{n}$ that is adopted in the present work:

$$\langle \nabla \cdot \underline{n} \rangle \approx \frac{\frac{1}{2} - \overline{c}}{l_w} \quad . \tag{3.23}$$

l_w measures the wave length of a flame front which wrinkles within the turbulent flame brush. Bray [75] introduced the following model to describe l_w:

$$l_w = C_l l_{int} \left(\frac{s_l}{u'} \right)^{C_w} \quad . \tag{3.24}$$

The exponent C_w as well as the coefficient C_l are model input parameters. Both are set to unity in the present work, as it is suggested by Bray [75]. Note that $\overline{c}$ is the ensemble-averaged reaction progress variable. $\overline{c}$ is calculated with the following equation from Veynante and Vervisch [76]:

$$\overline{c} = \tilde{c} \frac{\left(1 + \left({}^{T_b}/_{T_u} - 1\right)\right)}{\left(1 + \tilde{c}\left({}^{T_b}/_{T_u} - 1\right)\right)} \quad . \tag{3.25}$$

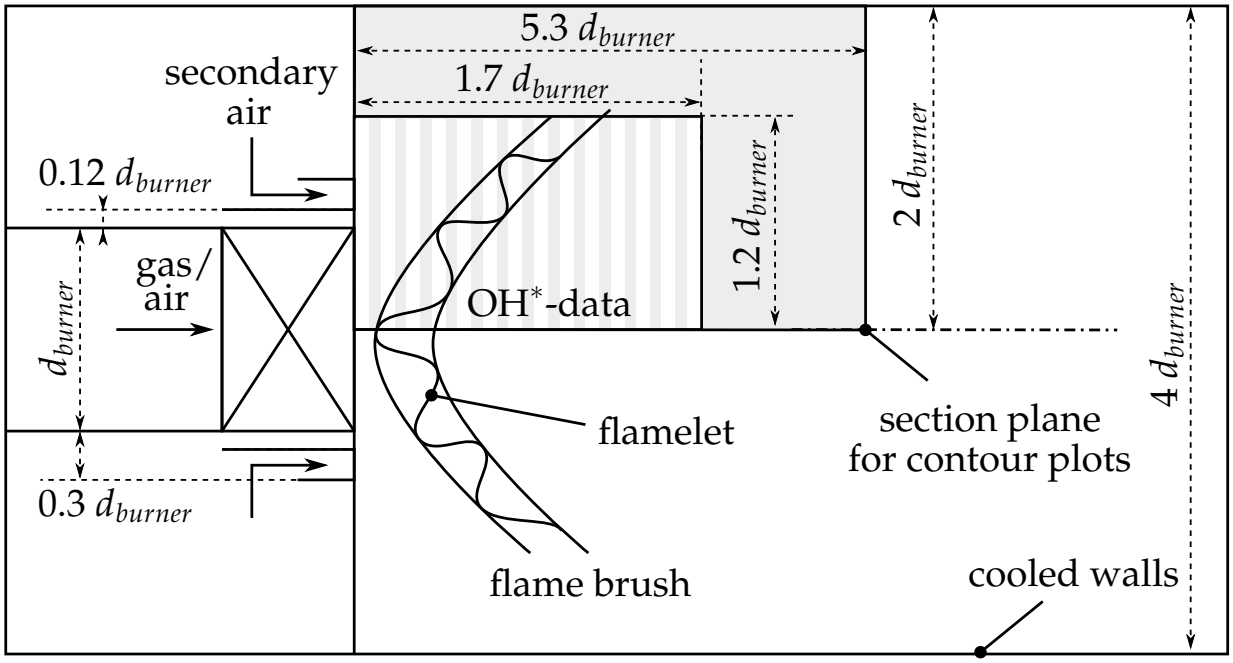

Figure 3.7.: Illustration of Marosky's [58] validation case.

3.3. Application and Validation

The proposed combustion modeling strategy is implemented in FLUENT [77] by extending the functionality of the original FGM infrastructure. Moreover, a software is developed that automatically generates the tables on the basis of premixed counterflow flamelets. Details to the software implementation can be found in Appendix A. Note that the software includes both the combustion and the CO modeling that is introduced in the next chapter. Computational overhead caused by the model extension is negligibly small. The introduced modeling approach is applied to an atmospheric single-burner test rig from Marosky [58], which is illustrated in Figure 3.7. A mixture of air and natural gas is preheated to 673.15 K and enters the combustion chamber through the A_2EV[5] burner. The swirling flow breaks down in the combustion chamber and provides a stagnation point near the burner exit at which the combustion stabilizes. 3 % of the total amount of preheated air flows through a perforated front plate into the combustion chamber near to the burner exit. Fuel mass flow is adjusted to achieve a global equivalence ratio of $\phi = 0.5$. The validation case features considerable heat loss over the cooled walls. Figure 3.7

[5] Details regarding the A_2EV burner can be found in Sangl [78] and Mayer [79].

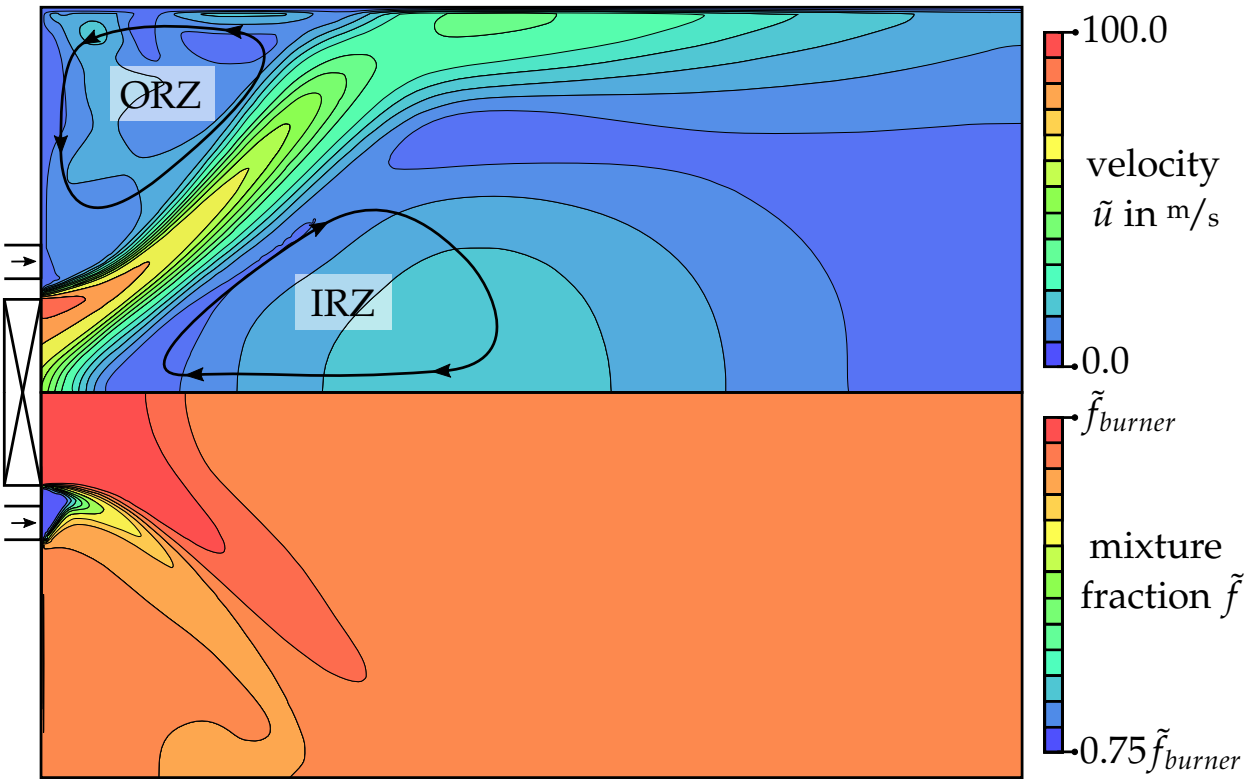

Figure 3.8.: Distributions of velocity (upper half) and mixture fraction (lower half) of Marosky's [58] validation case.

shows an area that is marked by white stripes in which OH^*-emissivity data is available.

The domain is discretized by employing a block structured grid. A mesh independence analysis in a way proposed by Ferziger and Peric [80] is conducted in order to guarantee a mesh independent solution. In Marosky's experiment, the outer shell of the wall is cooled by impinging air. As the CFD simulation does not include the environment, an energetic boundary condition needs to be modeled in order to cover the significant heat losses. For this purpose, a thermal boundary condition is used that calculates the heat flux on the basis of the heat transfer coefficient α and the difference between wall temperature and the ambient temperature. Unfortunately, the heat transfer coefficient α is unknown and needs to be estimated. For this purpose, the highest experimental wall temperature is estimated by the brightest color of the glowing steel that has been experimentally observed. Moreover, α is automatically iterated in the simulation until the wall temperature in the simulations meet the estimated

wall temperature of the experiments. An overview of all conditions and models of the numerical set up is given in Table 3.2.

In the upper half of Figure 3.8 the corresponding velocity field is shown. The swirled flow leaves the burner exit at an velocity that is close to $100\,\mathrm{m/s}$. A stagnation point is located on the central axis close to the burner exit. As indicated in Figure 3.8 , the flow topology causes an inner and outer recirculation zone, which are important to stabilize lean combustion as burnt material ignites the unburnt main flow at the stagnation point. The velocity of the secondary air jet is low and can hence not be identified in Figure 3.8. Furthermore, mixture fraction f is shown in the lower half of Figure 3.8. Note that the mixture fraction at the burner outlet $\tilde{f}_{burner}$ corresponds to an equivalence ratio of $\phi = 0.513$. The dilution process of the main flow due to the secondary air is evident as the mixture fraction $\tilde{f}$ is highest in the main flow and lowest for the secondary air.

In the first contour plot of Figure 3.9, the distribution of total flame stretch $\langle \kappa \rangle$ is shown. In addition, the three different parts that flame stretch consists of are presented below. The second and the third contour plots show the distribution of mean and turbulent strain. Furthermore, curvature is plotted at the bottom. Values of the individual parts of flame stretch are tabulated in Table 3.3. Strain due to turbulent fluctuations is the dominating part as mean strain, and curvature are significantly smaller. The distribution of total flame stretch (first contour plot of Figure 3.9) features two maxima that occur in the shear layers between the main flow and the outer and inner recirculation zones. Both maxima are based on high values of turbulent strain $\langle \kappa_{st,t} \rangle$ but occur for different reasons. The maximum in the outer shear layer results from short turbulent times (k/ϵ in Equation 3.20). Moreover, the maximum in the inner shear layer is mainly based on high values of u' that lead to a sharp increase of the $\mathcal{I}$-function. Note that mean strain and curvature have their maximum close to the burner exit where the velocity gradient $\partial \tilde{u}_i / \partial x_j$ (cf. Equation 3.17) and the RMS velocity u' (cf. Equation 3.24) are highest.

Figure 3.10 shows the distribution of heat loss ψ. Flow that leaves the burner does not show any heat loss and ψ is zero. Significant heat losses occur at the non-adiabatic walls. Cooled material circulates in the inner

Table 3.2.: Summary of the numerical setup for Marosky's [58] test rig.

boundary conditions:	
T_∞	300 K
T_u	673.15 K
α_{wall}	50 $^{W}/_{m^2K}$
$\dot{m}_0$ (air)	400 $^{g}/_{s}$
$\dot{m}_{0,sec}$ (air)	3 % of $\dot{m}_0$
ϕ	0.5
CFD:	
CFD software	FLUENT v18.0 [77]
turbulence model	k-ω SST
Sc_t	0.7
mesh type	hexahedral (block structured)
mesh size (without burner)	1.7e6 cells
flamelet generation:	
kinetic	GRI 3.0 [37]
discrete points of $c/f/\psi/\kappa$	232/21/21/$\approx$19
$m_{\kappa,\psi}$	1.49

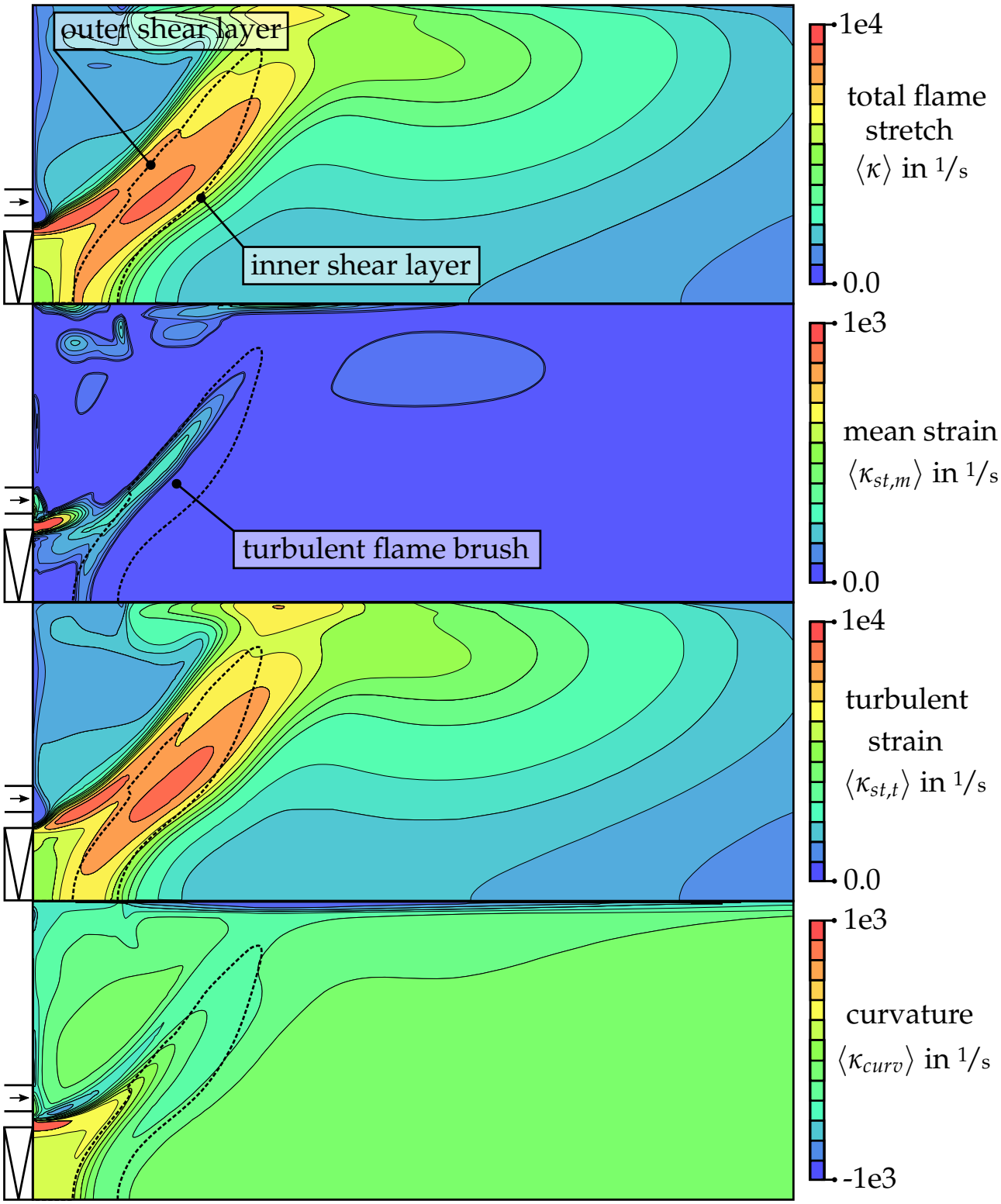

Figure 3.9.: Distributions of flame stretch, mean strain, turbulent strain, and curvature of Marosky's [58] validation case..

Table 3.3.: Strain and curvature averaged over the turbulent flame brush.

total flame stretch $\langle \kappa \rangle_{tfb}$	7603 $^1/_s$
mean strain $\langle \kappa_{st,m} \rangle_{tfb}$	54 $^1/_s$
turbulent strain $\langle \kappa_{st,t} \rangle_{tfb}$	7690 $^1/_s$
curvature $\langle \kappa_{curv} \rangle_{tfb}$	-141 $^1/_s$

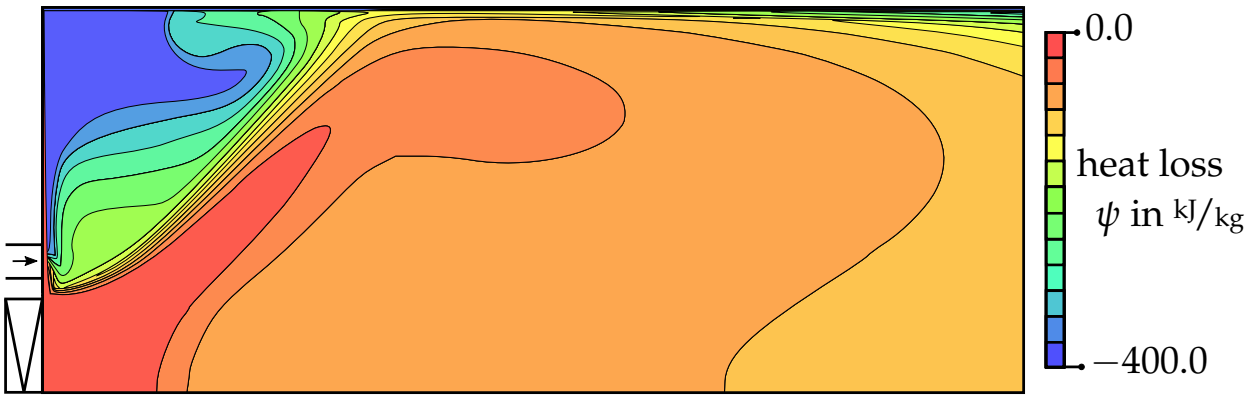

Figure 3.10.: Distribution of heat loss ψ of Marosky's [58] validation case.

and outer recirculation zone. The outer recirculation zone shows significantly higher heat losses than the inner recirculation zone as the velocity in the outer recirculation zone is low and the residence time is hence increased. The high heat losses in the outer recirculation zone lead to low enthalpies in the outer shear layer causing a significant reduction of reactivity in this region. Figure 3.11 shows the distributions of reference fuel consumption speed s_c^0 and the non-adiabatic, strained fuel consumption speed s_c^*. s_c^0 is solely a function of the mixture fraction. It approaches zero for pure air at the secondary air inlet and reaches its maximum at the burner outlet where the mixture is not yet diluted by the secondary air injector. Flame stretch and heat loss have a substantial impact on the flame speed as shown in the lower half of Figure 3.11. The fuel consumption speed approaches zero in the outer recirculation zone due to the substantial heat loss in this region. Moreover, high flame stretch rates occur in the inner shear layer causing a local minimum of the fuel consumption speed s_c^*.

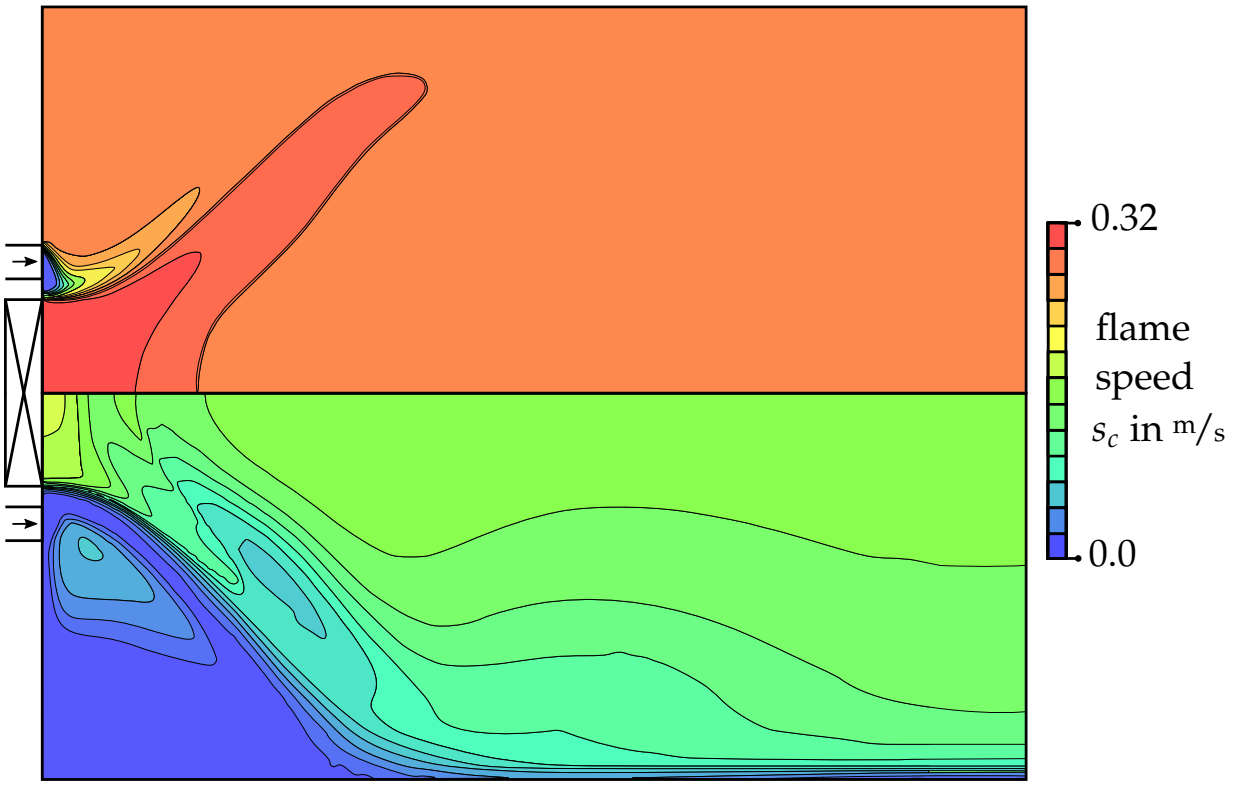

Figure 3.11.: Reference fuel consumption speed s_c^0 (upper half) and the non-adiabatic, strained fuel consumption speed s_c^* (lower half) of Marosky's [58] validation case.

Figure 3.12 demonstrates the impact of the proposed modeling strategy on combustion. For this purpose, the influence of flame stretch and heat loss on fuel consumption speed is plotted at constant mixture fraction. Furthermore, a path indicates the fuel consumption speed reduction that results from heat loss and flame stretch. Note that the values of flame stretch, heat loss, and the mixture fraction are volume-averaged over a numerically predicted turbulent flame brush of Marosky's validation case. Fuel consumption speed s_c is reduced by about 62 % when heat loss and flame stretch are considered. This results in a correction of the reaction progress variable by about 24 % ($m_{\kappa,\psi} = 1.48$). It can be concluded that the source term of the PDF-integrated reaction progress variable substantially decreases when elevated flame stretch rates and heat loss are considered by the introduced model extension for FGM. The impact on the turbulent flame brush is shown in Figure 3.13. Experimentally obtained OH^* emissivity data is shown at the top. The experimental shape of the flame brush is indicated by a white line in all contour plots to sim-

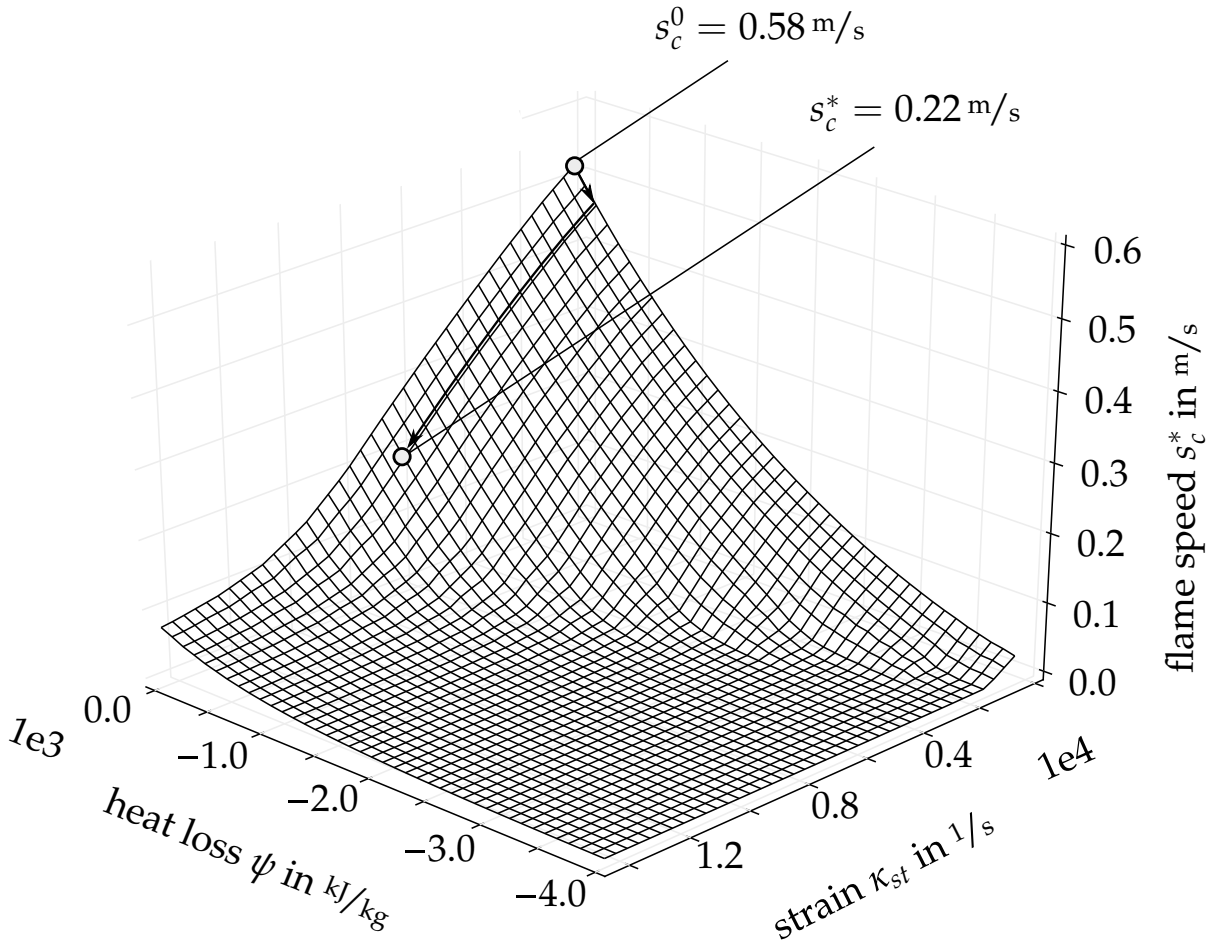

Figure 3.12.: Demonstration of the influence of flame stretch and heat loss on flame speed. The corresponding values are volume-averaged over a numerically predicted turbulent flame brush of Marosky's validation case (cf. Table 3.2 and 3.3).

plify comparison. In the top left corner, the distribution of the unmodified reaction progress source term ($\Gamma = 1.0$) is shown. The numerically predicted heat release distribution of the original FGM deviates significantly from the experimental flame shape: Reactivity is overestimated in the outer shear layer, the flame brush thickness is too thin, and the flame stabilizes near the burner outlet. No major improvement can be achieved when solely heat loss is taken into account as shown in the top right corner. It can be concluded that the prediction of the heat release distribution of Marosky's [58] validation case is not significantly getting improved by considering heat loss only. The contour plot in the bottom left corner shows the heat release distribution when solely flame stretch

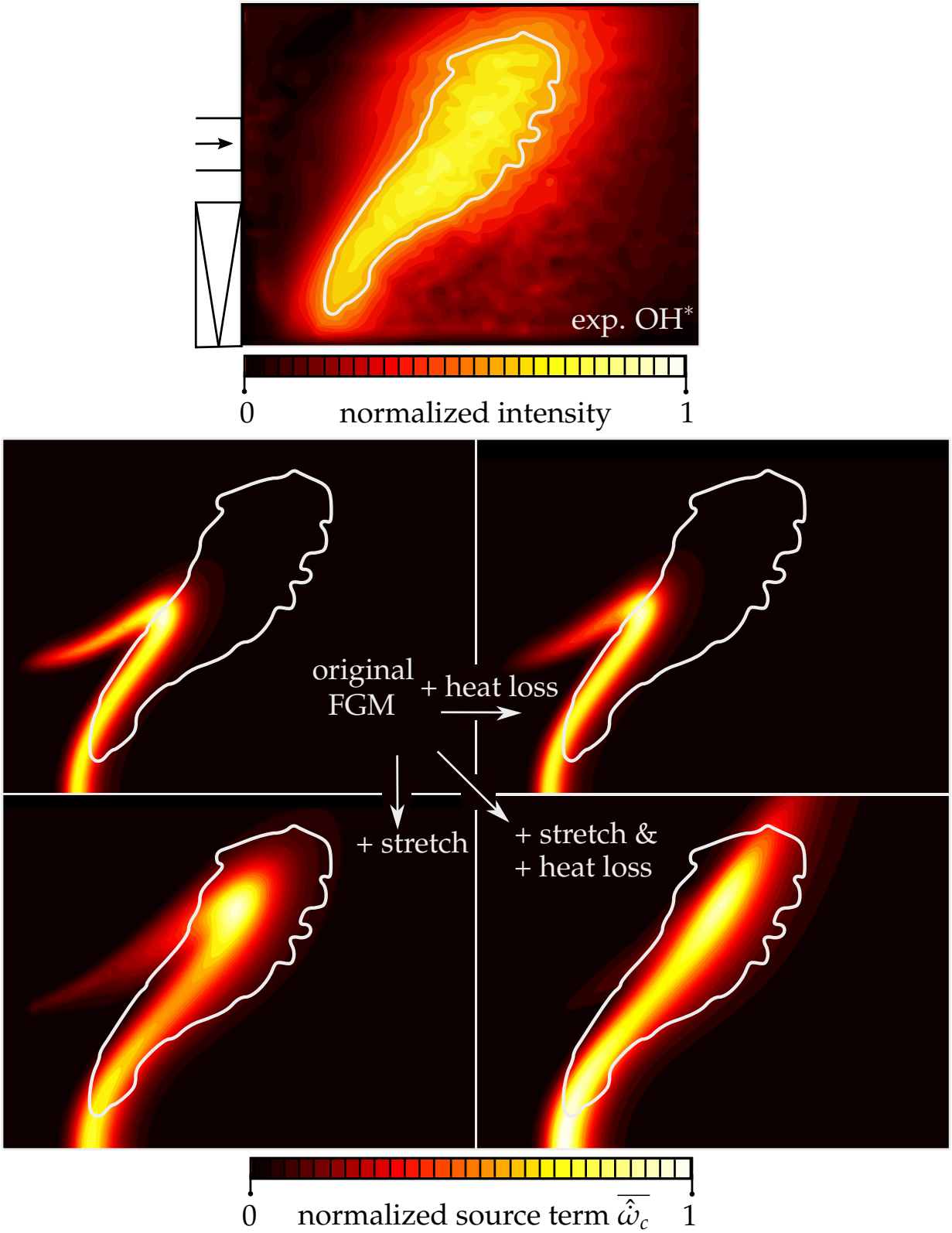

Figure 3.13.: Comparison of numerically predicted heat release with experimental OH^* emissivity data of Marosky's [58] validation case.

is considered. Flame stretch has a major impact and leads to a substantial improvement regarding position and shape of the turbulent flame brush. Nevertheless, the outer shear layer still exhibits minor heat release that is not in accordance with the experiments. The final model is shown in the bottom right corner. Reaction rates in the outer shear layer disappears and the numerically predicted turbulent flame brush is in good agreement with the experimental shape.

3.4. Model Comparison

Finally, a qualitative comparison of standard combustion models is performed and benchmarked using the experimental data by Marosky [58]. A short introduction to the models was provided in Section 2.3.4. Further information regarding the model implementations can be found in ANSYS [81].

The heat release prediction by EDM is shown in the lop left corner of Figure 3.14. As stated by Poinsot and Veynante [28], combustion models that are based on the EBU theory often overestimate the reaction rates when the characteristic turbulent time scale k/ϵ becomes large. This criticism is justified by the incorrectly predicted heat release distribution resulting from the use of EDM. Combustion is drastically overestimated in the shear layer to the outer recirculation zone. High strain rates occur in this region leading to significant damping of the reaction rates that is not considered by EDM. The strategy of adding a kinetic limitation to the species source terms in EDM is presented in the top right corner of Figure 3.14. No significant improvement is achieved as the flame brush becomes longer but no quenching of the outer shear layer occurs. Note that the EDM/FR model formulation implicitly accounts for heat loss since the decreased temperature influences the finite rate that is calculated by the Arrhenius law. A similar issue occurs by employing the TFC closure by Zimont et al. [51,52] as shown in the middle left. Furthermore, the middle right of Figure 3.14 shows the TFC model with a flame stretch correction that was proposed by Zimont et al. [52]. A substantial improvement by using the flame stretch correction is evident. The flame length fits the experimental shape but combustion still takes place in the shear layer that

is between the main flow of the burner and the outer recirculation zone. Significant improvement by considering flame stretch is evident and in agreement with the observations that have been made in the previous section. In addition, the original implementation of FGM and the proposed modeling strategy are shown in the bottom of Figure 3.14.

It is important to note that FGM is the only combustion model in this comparison that is able to accurately describe intermediate species. Realistic species trajectories within the turbulent flame brush are of great importance for CO modeling as demonstrated in the next chapter.

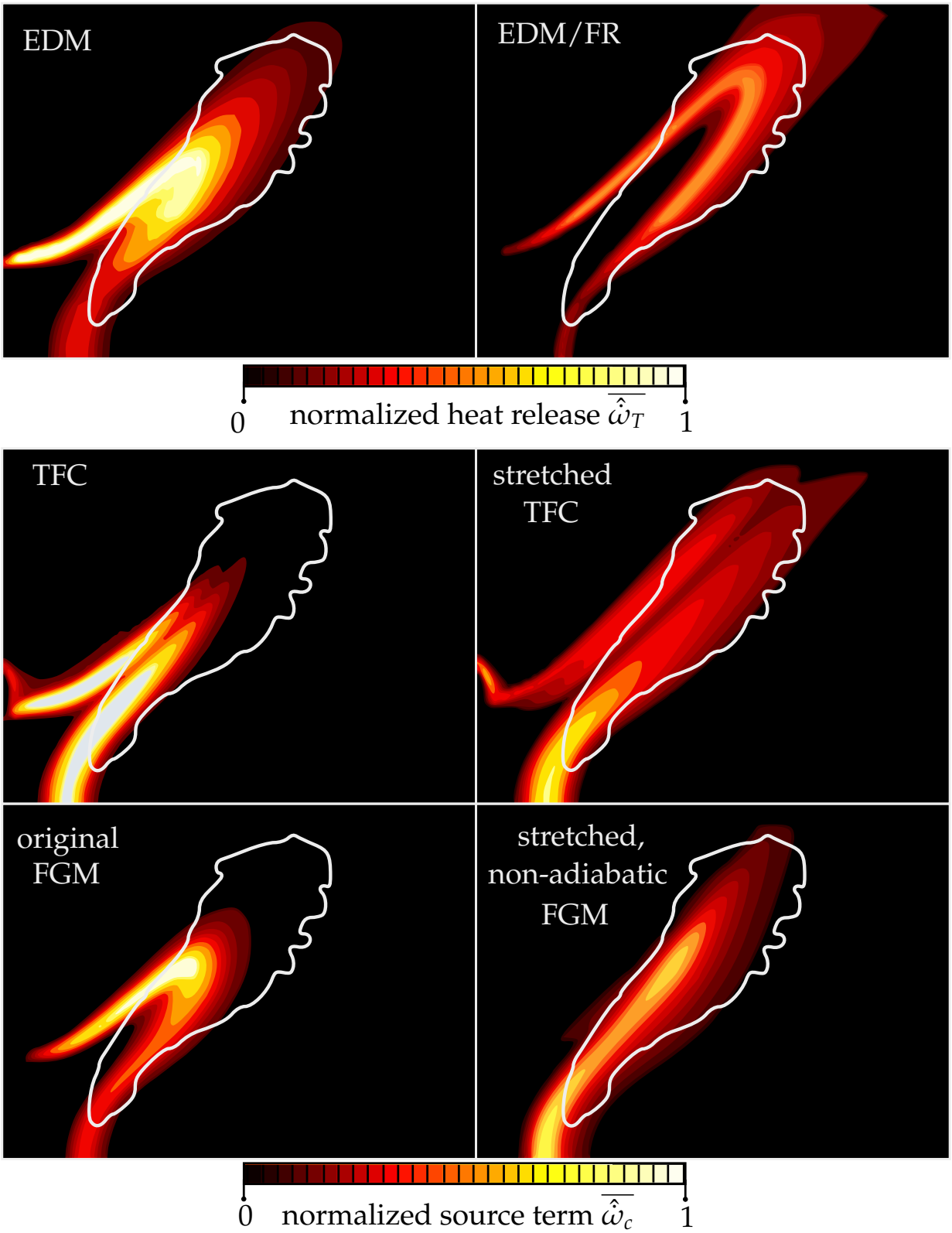

Figure 3.14.: Qualitative comparison of different standard combustion models.

4 Modeling CO

Flamelet-based approaches are able to accurately predict heat release distributions in cold conditions in a way that was demonstrated in Chapter 3. The question arises whether flamelets are also capable of describing CO emissions. As mentioned before, the typical thickness of a flamelet is usually several orders of magnitude smaller than the usual length of gas turbine combustors. The existence of CO emissions in the exhaust gas indicates that the CO burnout time is longer than the residence time in the combustion chamber. Predicting global CO with FGM would hence require flamelets to fluctuate through the whole gas turbine. This is unlikely as the turbulent flame brush stabilizes at the stagnation point that is provided by the vortex breakdown near the burner exit. It can be concluded that the successful modeling of CO emissions requires to perform a paradigm shift to describe the burnout region in which the flamelet assumption is not valid anymore. For this purpose, an approach that is capable of modeling the transition from flamelets to the kinetically limited burnout is presented in this chapter. In the first section, the basic idea of dividing the domain into several subregions is presented. Each sub region requires a specific modeling strategy that is covered by the Sections 4.2, 4.3, 4.4, and 4.5. Moreover, Section 4.6 shows the application of the proposed modeling strategy. Three different validation cases are employed in order to assess the model performance. In addition, the model is applied to an advanced combustor concept.

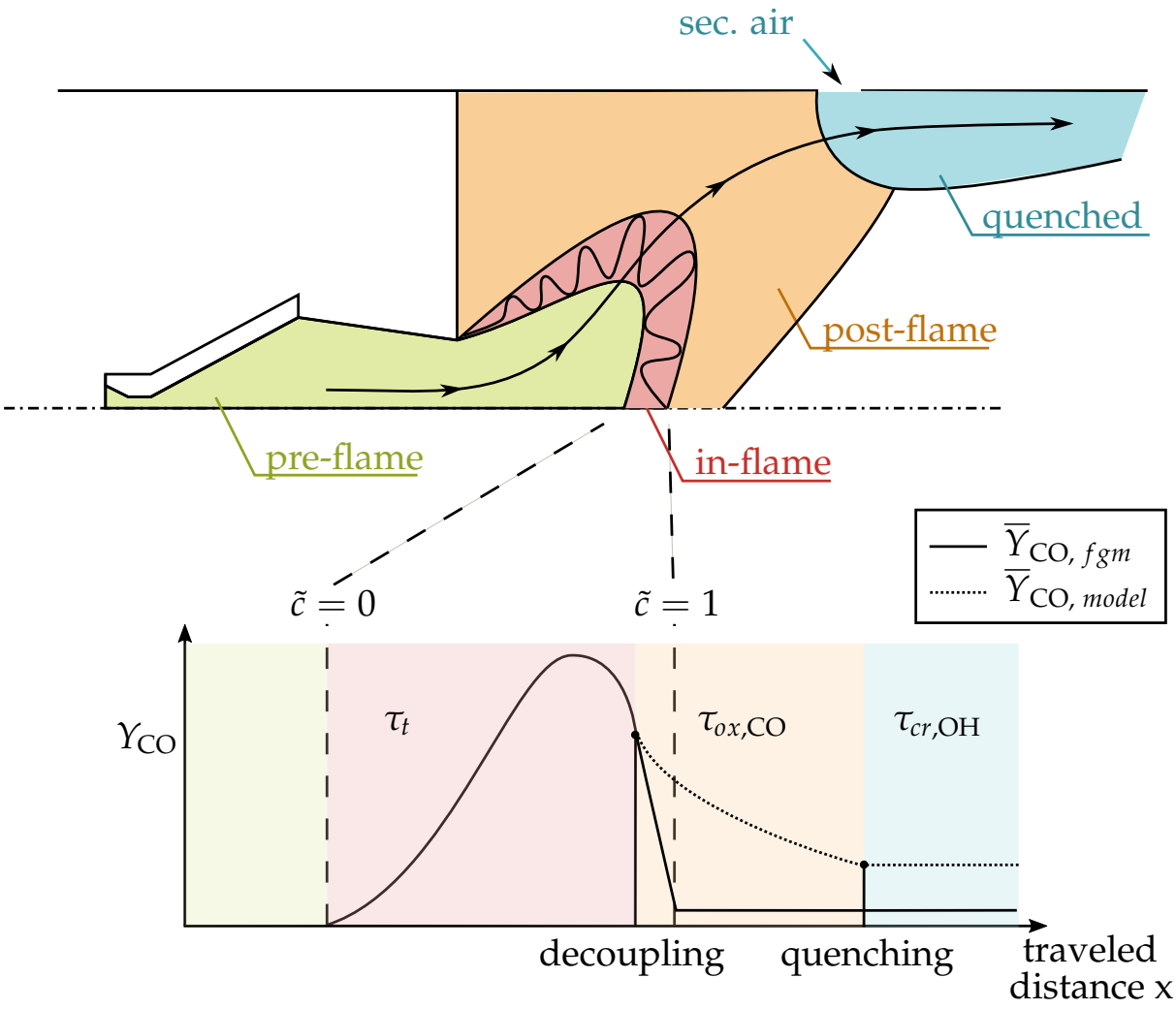

Figure 4.1.: Illustration of the domain partitioning that identifies the zones of different CO modeling.

4.1. Separating Time Scales

In order to describe CO separately from the combustion model, an additional transport equation is required:

$$\frac{\partial \overline{\rho}\widetilde{Y}_{CO}}{\partial t} + \frac{\partial \overline{\rho}\tilde{u}_i\widetilde{Y}_{CO}}{\partial x_i} = \frac{\partial}{\partial x_i}\left(\frac{\mu_t}{Sc_t}\frac{\partial \widetilde{Y}_{CO}}{\partial x_i}\right) + \overline{\dot{\omega}_{CO}} \ . \tag{4.1}$$

The strategy for closing this equation is based on the spatial division into multiple zones in a way that is illustrated in Figure 4.1. A Lagrangian observer is shown that travels on a trajectory through a combustor and

passes several regions. The observer's position determines the employed submodel for CO. In the lower half of Figure 4.1, a qualitative profile of CO as a function of the Lagrangian observer's traveled distance is shown. The first profile (—) represents CO predicted by the combustion model. As the Favre-averaged reaction progress $\tilde{c}$ reaches unity, the probability of flamelets is zero and CO is by definition in its equilibrium state. A second profile (·····) shows the prediction by the CO model that is introduced in the present chapter. CO is described by the combustion model only up to a certain point, which is denoted as the decoupling event. The decoupling event marks the point at which the burnout chemistry cannot be described by flamelets anymore. After CO left the flamelet-based species trajectories, CO oxidation becomes slower due to the absence of the flamelet's radical pool. Moreover, the post-flame model presented in this work looses its validity in situation in which the equivalence ratio is significantly decreased. In summary, four different regions of different modeling are defined:

- **pre-flame zone (□):** The source terms for CO are negligibly small before the chain-branching chemistry starts. Thereby, this zone does not require modeling.

- **in-flame zone (□):** This region is dominated by the time scales of turbulent mixing. Combustion chemistry is fast and can be described by flamelets. Hence, CO is derived from the combustion model in the way that is presented in Section 4.2.

- **post-flame zone (□):** Behind the turbulent flame brush, super-equilibrium species may occur like elevated CO. In this region, chemical time scales are usually small as the in-flame radical pool is not available anymore. The modeling approach for the post-flame region is introduced in Section 4.3. Furthermore, Section 4.4 presents a model for predicting the transition from the in- to the post-flame zone.

- **quenched zone (□):** In the potential situation of lean quenching, the equivalence ratio is low and the chemical rates are negligibly small. As argued in Section 4.5, this region is dominated by the creation time scale of OH.

4.2. Modeling In-Flame CO

Within the turbulent flame brush, CO is tabulated on the basis of PDF-integrated profiles of flamelets. The previously introduced combustion model modifies the reaction progress source term in order to take flame stretch and heat loss into account. The question arises whether the tabulated CO profiles also need correction in terms of flame stretch and heat loss. Figure 4.2 gives an answer by showing CO profiles at various flame stretch rates. Flame stretch alters the molecular diffusion of heat and species within the flamelet. Adding flame stretch and heat loss as further dimensions to the tabulation process would significantly increase the numerical effort. A reasonable alternative is thus to tabulate the unstretched, adiabatic mass fraction of CO and to model the influence of flame stretch and heat loss. Note that this approach is similar to the concept of the correction factor $\Gamma_{\kappa,\psi}$ that was introduced in the previous chapter in Equation 3.5. The tabulation of CO on the basis of freely-propagating flamelets (unstretched and adiabatic) reads

$$\overline{Y^0_{CO}} = \iint Y^0_{CO}\,(c,f)\,\mathcal{P}(c,\tilde{c},c'')\mathcal{P}(f,\tilde{f},f'')dcdf\ . \tag{4.2}$$

The question arises whether the correction factor $\Gamma_{\kappa,\psi}$ can be employed to modify $\overline{Y^0_{CO}}$ in the same way it is used to correct $\overline{\dot{\omega}^0_c}$ in Equation 3.5. In the proposed combustion modeling strategy, the correction factor $\Gamma_{\kappa,\psi}$ was modeled in Equation 3.7 without differentiating whether the reduction in fuel consumption speed s_c is due to flame stretch κ or heat loss ψ. An interpretation of this assumption is that s_c and the reaction progress source term $\dot{\omega}_c$ are both quantities describing reactivity. Hence, changing s_c has a direct effect on the reaction progress source term $\dot{\omega}_c$, regardless whether the reduction in reactivity is based on flame stretch or heat loss. Unfortunately, this assumption does not apply for the connection between fuel consumption speed s_c and CO. It can be shown that flame stretch κ often has a significant influence on CO while the impact of heat loss ψ is moderate. Thus, flame stretch and heat loss need to be considered independently from each other by introducing two isolated correction factors:

$$\overline{Y^*_{\mathrm{CO}}} = \Gamma_{\psi,\mathrm{CO}}\Gamma_{\kappa,\mathrm{CO}} \iint Y^0_{\mathrm{CO}}\,(c,f)\,\mathcal{P}(c,\tilde{c},c'')\mathcal{P}(f,\tilde{f},f'')dcdf\ . \tag{4.3}$$

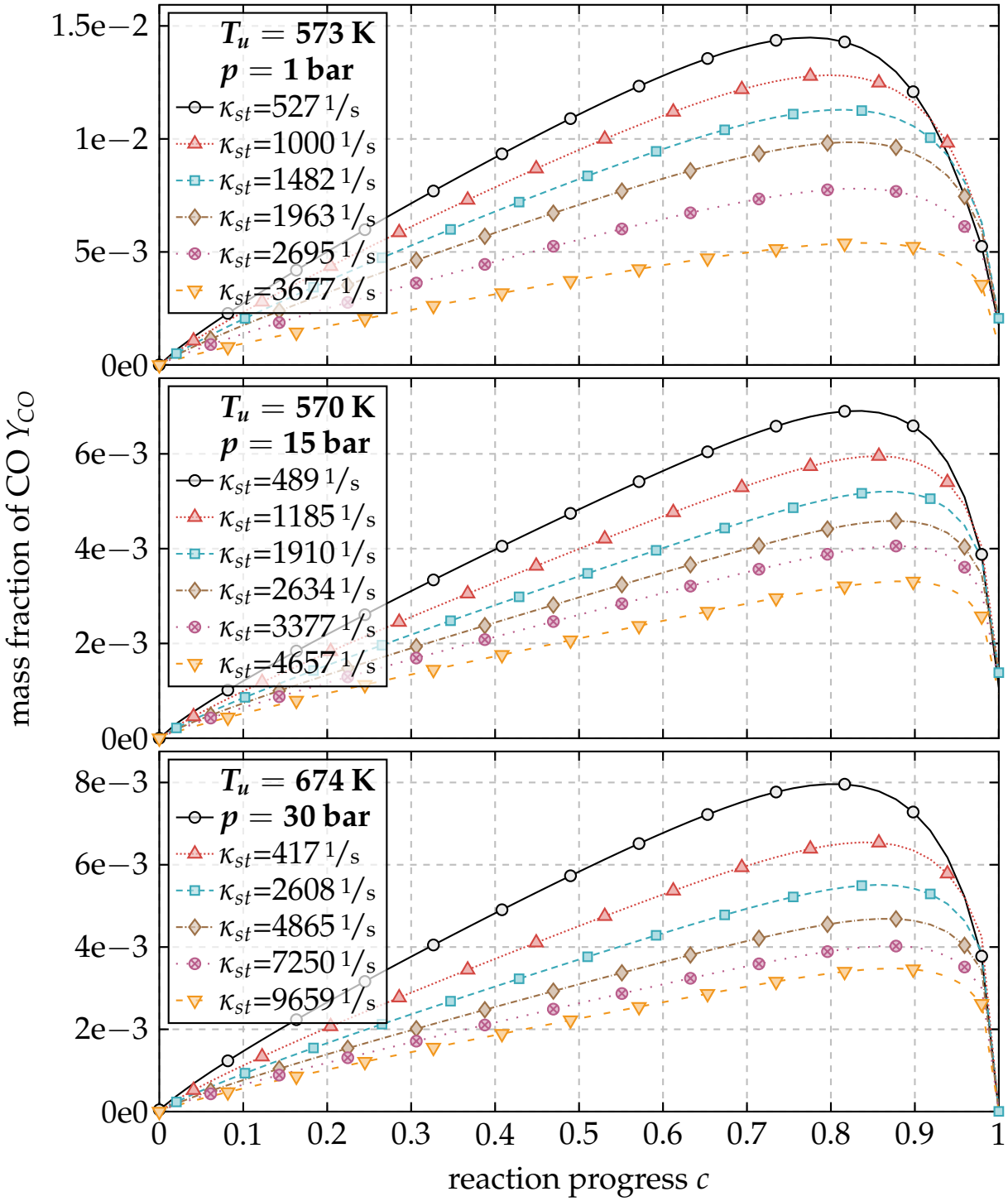

Figure 4.2.: Flame stretch dependency of CO demonstrated at three pressure levels (premixed counterflow flamelets at $\phi = 0.5$, and $T_u = 573.15\,\mathrm{K}$ calculated using GRI 3.0 [37] and CANTERA [34]).

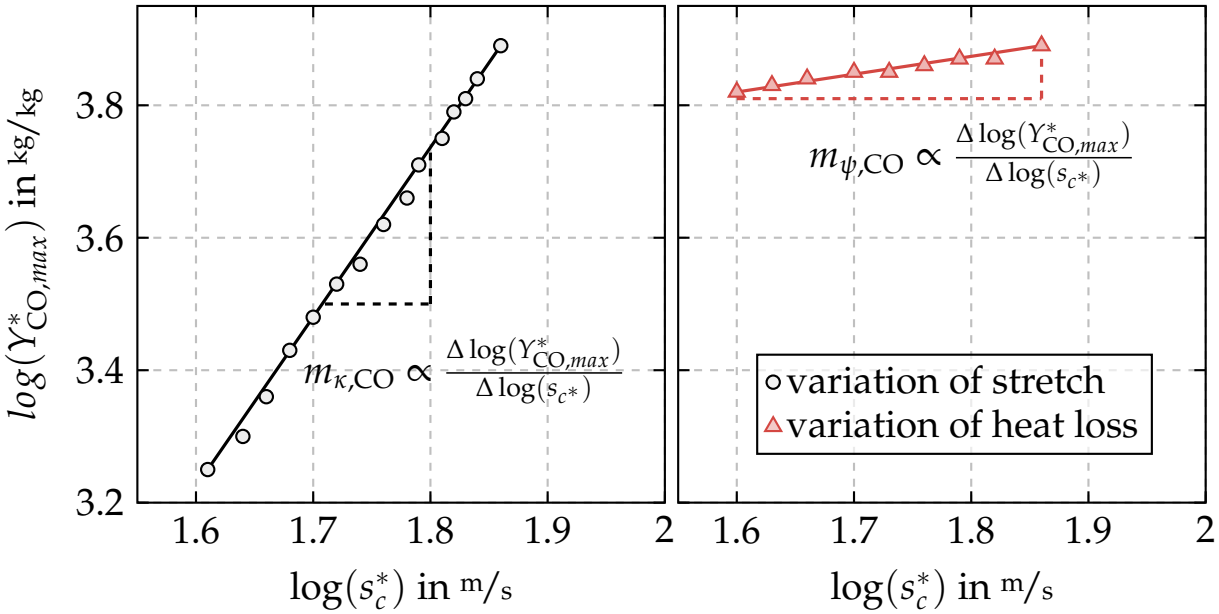

Figure 4.3.: Demonstration of the constant character of the proportionality exponents $m_{\kappa,CO}$ and $m_{\psi,CO}$.

Furthermore, the correction factors read

$$\Gamma_{\psi,CO}\left(\kappa^0, \psi, \tilde{f}\right) = \left(\frac{s_c^*\left(\kappa^0, \psi, \tilde{f}\right)}{s_c^0\left(\tilde{f}\right)}\right)^{m_{\psi,CO}} \tag{4.4}$$

$$\text{and} \quad \Gamma_{\kappa,CO}\left(\kappa, \psi^0, \tilde{f}\right) = \left(\frac{s_c^*\left(\kappa, \psi^0, \tilde{f}\right)}{s_c^0\left(\tilde{f}\right)}\right)^{m_{\kappa,CO}} . \tag{4.5}$$

Both relations are analytically correct if

$$s_c^*\left(\kappa^0, \psi, \tilde{f}\right)^{m_{\psi,CO}} \sim \overline{Y^*_{CO}}\left(\kappa^0, \psi, \tilde{f}, \tilde{c}\right) \tag{4.6}$$

$$\text{and} \quad s_c^*\left(\kappa, \psi^0, \tilde{f}\right)^{m_{\kappa,CO}} \sim \overline{Y^*_{CO}}\left(\kappa, \psi^0, \tilde{f}, \tilde{c}\right) \tag{4.7}$$

are valid. Direct modeling of these relations is difficult. Hence, the assumption is introduced that the proportionality between the peak value of CO and the corresponding flame speed does not change due to PDF integration. Note that this assumption was also used in the Equations 3.8 and 3.9.

$$s_c^*\left(\kappa^0, \psi, \tilde{f}\right)^{m_{\psi,CO}} \sim Y^*_{CO,max}\left(\kappa^0, \psi, \tilde{f}\right) \tag{4.8}$$

$$\text{and} \quad s_c^*\left(\kappa, \psi^0, \tilde{f}\right)^{m_{\kappa,CO}} \sim Y^*_{CO,max}\left(\kappa, \psi^0, \tilde{f}\right) . \tag{4.9}$$

Finally, the proportionality exponents read

$$m_{\psi,\mathrm{CO}} \sim \frac{log\left(Y^*_{\mathrm{CO},max}\left(\kappa^0,\psi,\tilde{f}\right)\right)}{log\left(s^*_c\left(\kappa^0,\psi,\tilde{f}\right)\right)} \tag{4.10}$$

$$\text{and} \quad m_{\kappa,\mathrm{CO}} \sim \frac{log\left(Y^*_{\mathrm{CO},max}\left(\kappa,\psi^0,\tilde{f}\right)\right)}{log\left(s^*_c\left(\kappa,\psi^0,\tilde{f}\right)\right)}\,. \tag{4.11}$$

Both proportionality exponents can be interpreted as the gradients of a functional correlation between $\log(Y_{\mathrm{CO},max})$ and $\log(s_c)$ as plotted in Figure 4.3. The data points are determined by a set of premixed counterflow flamelets that equal in reactants temperature T_u, pressure p, and equivalence ratio ϕ and solely differ in strain (left hand side) or in heat loss (right hand side). Note that the used boundary conditions of the flamelets are based on values that are averaged over the turbulent flame brush of a validation case that will be introduced in Section 4.6.1 (cf. Table 4.1). The import conclusion of Figure 4.3 is that the connection of $\log(Y^*_{\mathrm{CO},max})$ as a function of $\log(s^*_c)$ has a linear character and $m_{\kappa,\mathrm{CO}}$ as well as $m_{\psi,\mathrm{CO}}$ is hence constant for varying strain rates or heat losses. Due to the linear proportionalities, the exponents can be evaluated as the gradient of a fitted linear equation.

4.3. Modeling Post-Flame CO

As mentioned above, flamelets cannot be used to describe chemistry behind the turbulent flame brush. As shown in the following, the employment of detailed chemistry is not necessarily needed due to the simplicity of CO burnout chemistry. The burnout of CO can be described using a single reaction equation as mentioned by Turns [82]:

$$\mathrm{CO} + \mathrm{OH} \longrightarrow \mathrm{CO_2} + \mathrm{H}\,. \tag{4.12}$$

Reaction rates that are obtained from a zero-dimensional reactor simulation are shown in Figure 4.4 at three different constant pressure conditions for an equivalence ratio of $\phi = 0.3$. Note that the reaction analysis is repeated for an equivalence ratio of $\phi = 0.5$ in the Appendix B. Note that only the late burnout is plotted. As one can see, $\mathrm{CO} + \mathrm{OH} \rightarrow \mathrm{CO_2} + \mathrm{H}$

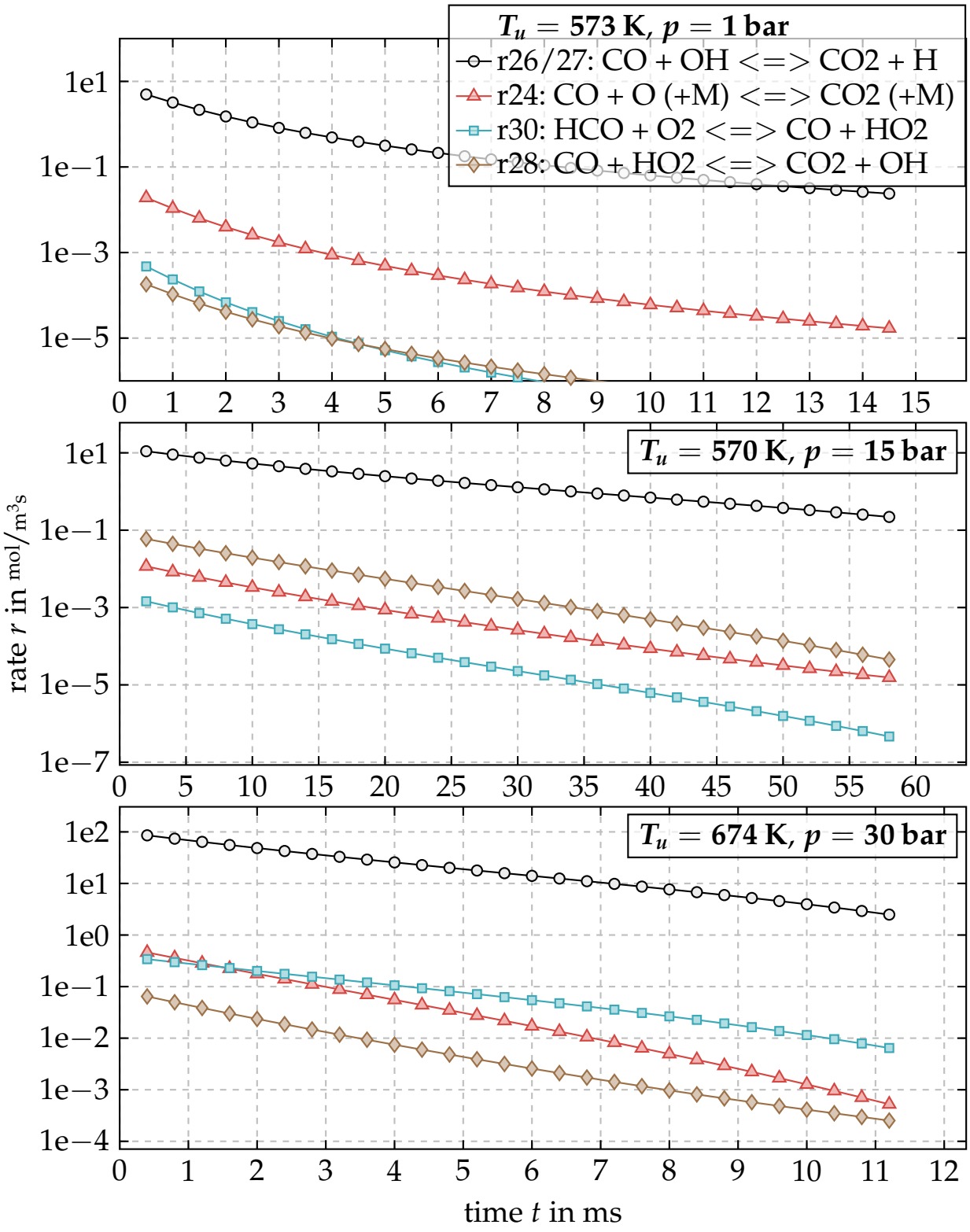

Figure 4.4.: Four most relevant CO reactions in the late burnout (constant pressure reactor at $\phi = 0.3$, calculated using GALWAY 1.3 [38] and CANTERA [34]).

(–o–) is always about two orders of magnitude greater than the second strongest reaction (–△–). Using Equation 4.12 to close $\overline{\dot{\omega}_{CO}}$ requires knowledge of the concentration of CO and OH as well as the non-adiabatic temperature. Temperature and the concentration of CO are known from their corresponding transport equations. OH is unknown and need to be modeled. The use of a kinetic mechanism to evaluate OH would require to transport all participating species, leading to a tremendous increase in computational effort. Fortunately, OH kinetic mechanisms are not required, as discussed in the following.

It is frequently reported in literature that OH is in equilibrium during the burnout of CO. For instances, Connors et al. [83] assumes OH to be in equilibrium for the development of a semi-empirical model to globally predict CO emissions in gas turbines. Using this assumption, the post-flame source term of CO can be evaluated using

$$-\frac{d\,[CO]}{dt} = k_{arr,for}\,(T)\,[CO]\,[OH]_{eq}\,. \tag{4.13}$$

In the present work, the equilibrium of OH is determined using GALWAY 1.3 [38] kinetics. Furthermore, $k_{arr,for}$ is calculated using Arrhenius parameters from Joshi and Wang [84] that are also included in GALWAY 1.3.

The model simplifications are further discussed and validated in the following. Flagan and Seinfeld [85] compared time scales of different approaches for treating OH and $k_{arr,for}$. For this purpose, a characteristic time scale for the burnout of CO is defined:

$$\tau_{CO} = \frac{[\mathrm{CO}]}{k_{arr,for}[\mathrm{CO}][\mathrm{OH}]} = \frac{1}{k_{arr,for}[\mathrm{OH}]}\,. \tag{4.14}$$

τ_{CO} as a function of ϕ is plotted in Figure 4.5. Several models are reprinted and compared to the proposed post-flame model (–o–). The second model (–△–) equals the approach in this work, as OH is assumed to be in equilibrium and $k_{arr,for}$ is based on shock tube experiments. Note that deviations between the first two approaches (–o– and –△–) may be related to different Arrhenius parameters for the evaluation of $k_{arr,for}$ (cf. Equation 2.9). Moreover, the third profile (–□–) represents a model by Fristrom and West-

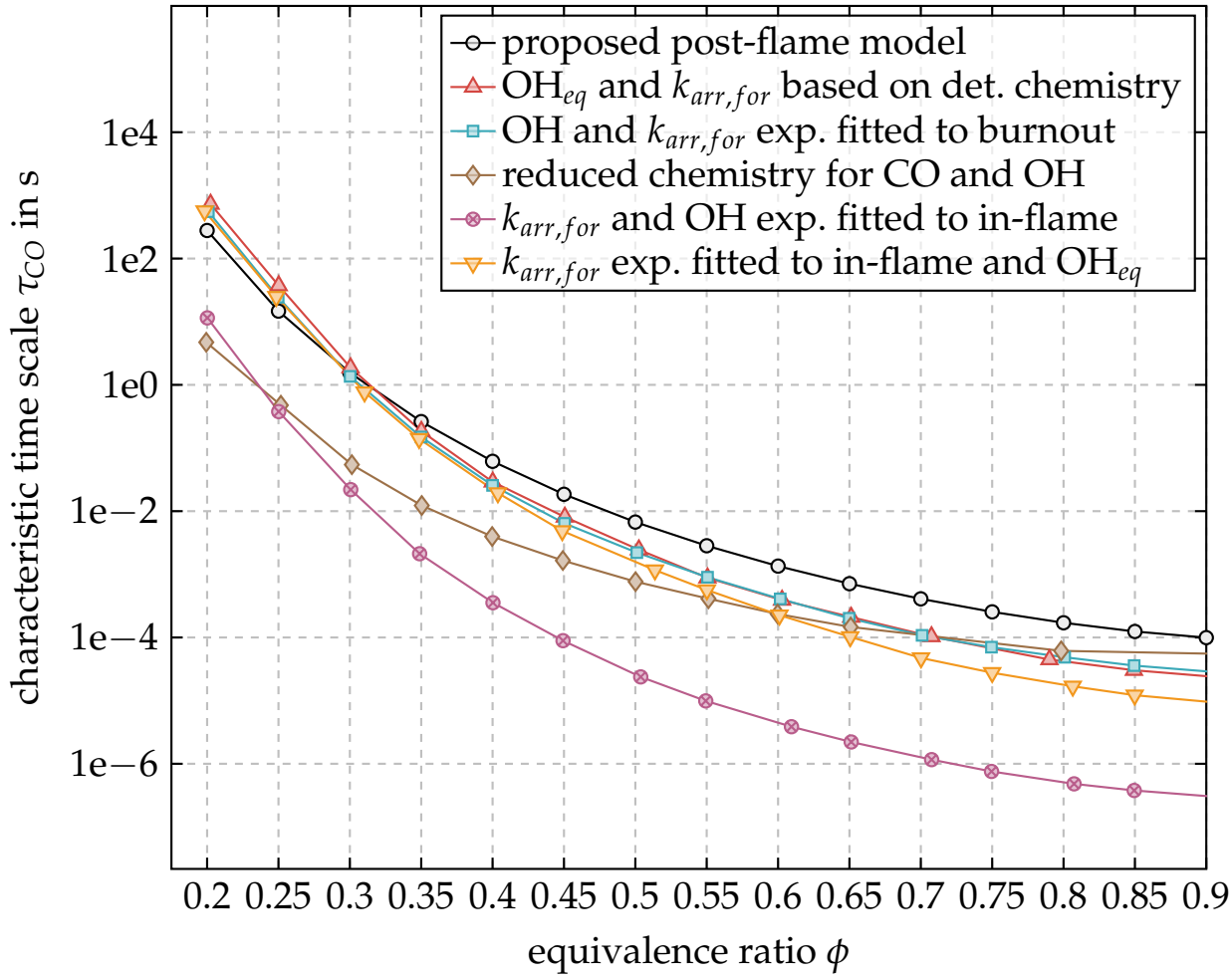

Figure 4.5.: CO burnout time scales for different strategies of considering OH (reprinted and adapted from Flagan and Seinfeld [85]).

enberg [86], which uses OH and $k_{arr,for}$ that are fitted to experimental data. Note that this is in good agreement with the first two models indicating the validity of these approaches. The fourth model (—◈—) was published by Howard et al. [87] and uses reduced OH kinetics in combination with measured $k_{arr,for}$. A significant underestimation of the CO burnout time in lean conditions by the fourth approach is evident. This indicates that the development of a reduced model may not lead to more accuracy than using OH in equilibrium. Note that it is obvious that the reduced OH model is responsible for this inaccuracy as it is already proven by the first three models that a reduced CO model is able to achieve accurate results. The reason for this observation is that the OH chemistry is vast and cannot be reduced to a small set of equations without loosing significant accuracy.

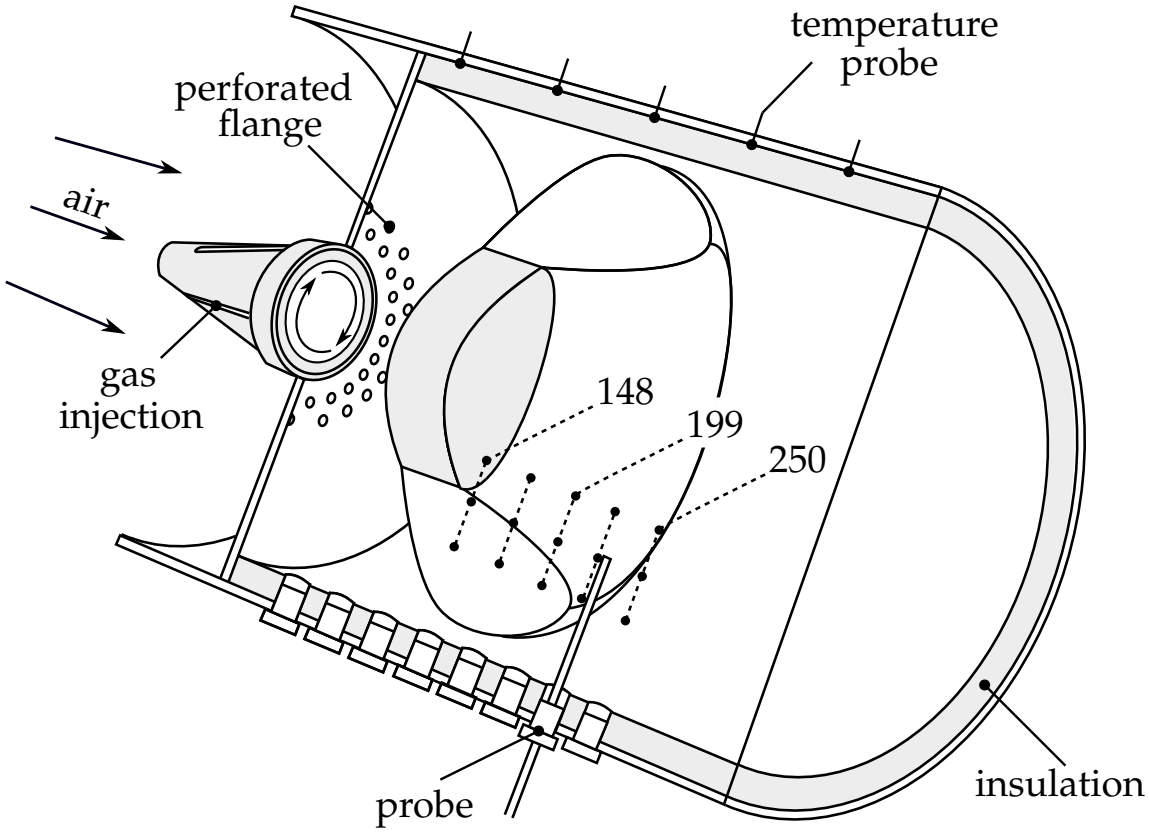

Figure 4.6.: Illustration of the atmospheric single-burner test rig with indicated post-flame measurement locations.

Dryer and Glassman [88] published a further strategy whereat OH and $k_{arr,for}$ are measured within the turbulent flame brush (⊸). Estimation of the burnout time scale of CO by using in-flame OH leads to a significant underestimation by one to two orders of magnitude. This model can significantly be improved by replacing the in-flame OH with equilibrium OH (▽). It can be concluded that the in-flame chemistry of CO is solely faster due to elevated OH. Note that this is the reason why flamelets or reactors cannot be used for the tabulation of CO burnout rates. A further finding is that $k_{arr,for}$ seems to be valid, regardless if it is obtained in the in- or post-flame zone.

Atmospheric experiments are conducted in order to prove the validity of the proposed post-flame model. The geometry is depicted in Figure 4.6. Note that the experiments are part of the study that is introduced in Section 4.6.1 where further details regarding the conditions can be found (cf Table 4.1). CO is measured by using a water-cooled probe at the locations

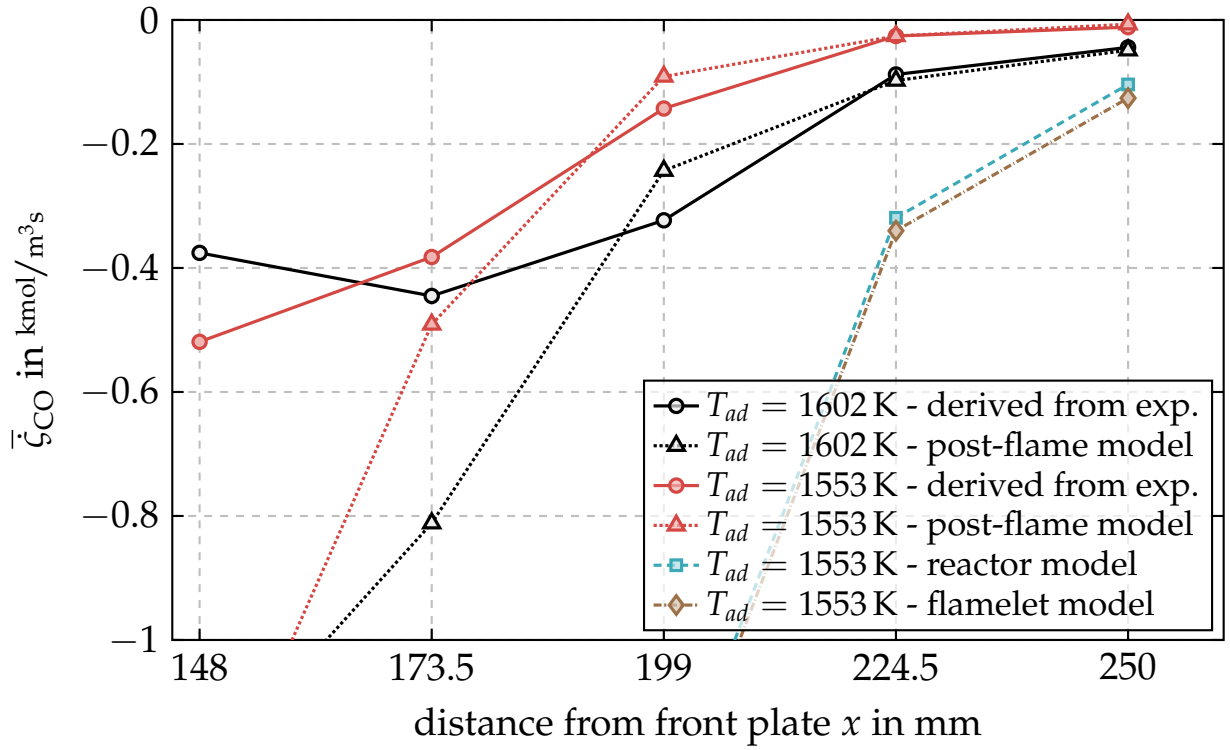

Figure 4.7.: Comparison of experimental with modeled source terms of CO.

that are indicated in Figure 4.6. Note that CO is measured and averaged at three different radii for each distance. The CO concentrations are used to derive source terms by using residence times between each distance that are retrieved from a corresponding CFD simulation. Figure 4.7 plots the resulting experimental CO source terms as a function of distance to the front plate. Moreover, experimental and numerical source terms are compared for two different adiabatic flame temperatures. The numerical CO source terms are calculated by using the proposed post-flame model (cf. Equation 4.13). After reaching a distance of 224.5 mm, the post-flame model prediction and the experiments are in good agreement. It is apparent that the transition from the in- to the post-flame zone should be predicted to occur between 199 mm and 224.5 mm.

In addition, Figure 4.7 shows CO source terms from a constant pressure reactor (-▫-) and from a freely-propagating flamelet (-◇-) at the corresponding reaction progress. Note that the experimental reaction progress source term can be derived from the measured CO_2 and CO concentra-

tions (cf. Equation 2.39) Both simulations drastically underestimate the source term due to the already discussed situation of elevated OH that is able to quickly burn out CO.

4.4. Modeling the Transition to Post-Flame

Models for closing CO within the flame and downstream of the turbulent flame brush are introduced in the previous sections. An additional model is needed to predict the reaction progress at which the transition from in- to post-flame occurs. A transition model is proposed by Wegner et al. [27] in which CO is set to the maximum value of CO occurring in the flame front at a predefined reaction progress. This idea is simple and robust but has a major simplification as it neglects the potential oxidation of CO within the turbulent flame brush before decoupling occurs. As demonstrated in the previous section, the flamelet-based oxidation of CO is usually significantly stronger than the burnout chemistry. Hence, a transition model is proposed that allows a fully flamelet-based closure in conditions in which the flamelet assumption is continuously valid during CO burnout. A suitable model for predicting the transition event needs to be based on a single criterion that unambiguously evaluates the validity of both the in- and the post-flame model. The criterion that is proposed in the following is modeled by comparing time scales. The in-flame model uses the assumption that all chemical time scales are faster than turbulent time scales. Furthermore, the post-flame zone is dominated by the slow burnout chemistry. The transition model in the present work is thus based on a Damköhler number that compares turbulent and chemical time scales:

$$Da_{\mathrm{CO}} = \frac{\tau_t}{\tau_{ox,\mathrm{CO}}} \ . \tag{4.15}$$

Both time scales are specified in the following. A reasonable choice for the chemical scale is the burnout time of CO within the turbulent flame brush. It is approximated by assuming a bimolecular reaction (cf. Turns [82]):

$$\tau_{ox,\mathrm{CO}} = \frac{\ln\left(\frac{[\mathrm{CO}]}{[\mathrm{CO}_{eq}]} + \left(1 - \frac{[\mathrm{CO}]}{[\mathrm{CO}_{eq}]}\right)\frac{[\mathrm{OH}]}{[\mathrm{CO}]}\right)}{([\mathrm{CO}] - [\mathrm{OH}])\, k_{arr,for}} \ . \tag{4.16}$$

The turbulent time scale can be interpreted as a characteristic time for micro-mixing and reads

$$\tau_t = \frac{l_{int}}{u'} \propto \frac{k}{\epsilon} \ . \tag{4.17}$$

In the context of RANS simulations, k and ϵ can be derived from the turbulence model. The decoupling event is assumed to take place when Da_{CO} drops below a critical value. In this work, $Da_{CO,crit}$ is unity as this value marks the transition point when chemical time scales start to exceed turbulent time scales.

4.5. Modeling Lean Quenching

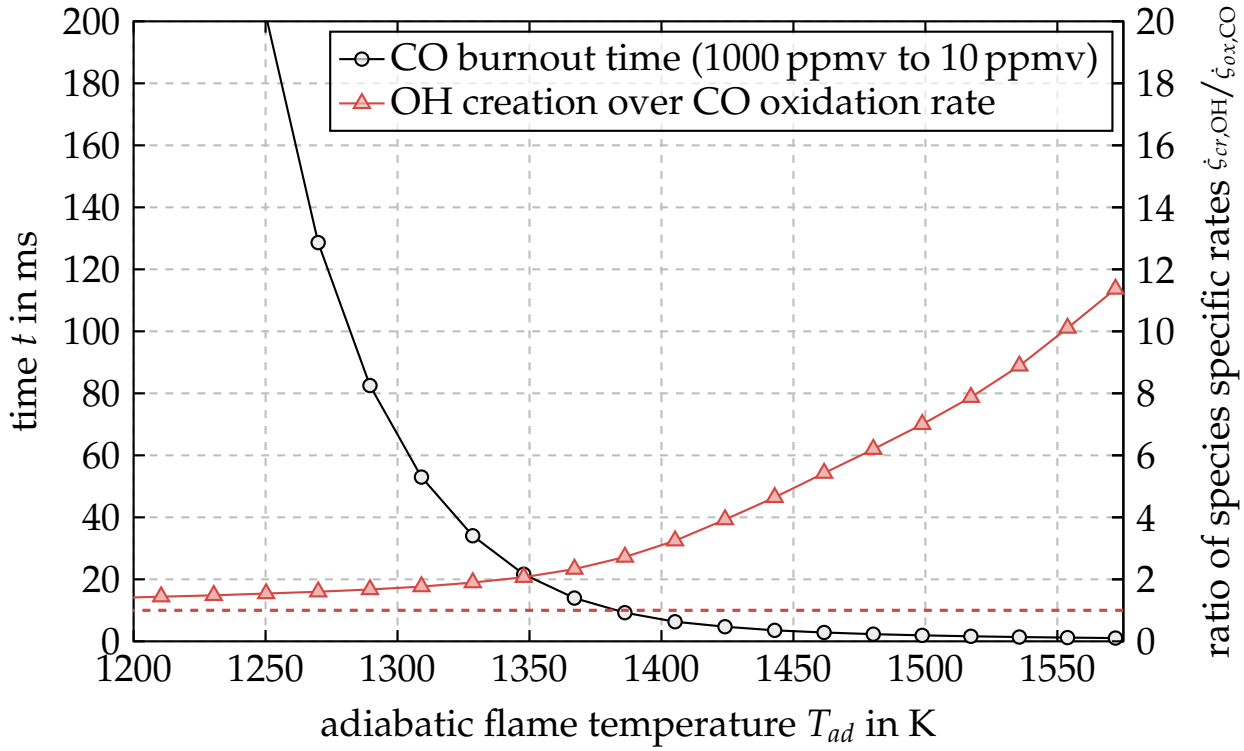

Figure 4.8.: Temperature dependent burnout time and ratio of OH creation to CO oxidation (constant pressure reactor at $p = 15\,\text{bar}$, calculated using GALWAY 1.3 [38] and CANTERA [34]).

In order to guarantee low emissions at part load, gas turbines usually employ fuel staging concepts. Lean streaks may occur due to inactive burners, leakage air from sealings, and cooling air from liners. The mechanism of diluting the reactive flow to a level in which the reaction rates decrease

to zero is denoted as lean quenching. Note that the combustion model, and consequently the in-flame model, are inherently able to consider lean quenching effects, as premixed counterflow flamelets can be calculated even for mixture fractions that are close to zero.

The post-flame model that was proposed in Section 4.3 is based on the assumption that OH is in equilibrium during burnout. This implies that the recreation of OH is always faster than the burnout of CO. A numerical analysis of this simplification is demonstrated in Figure 4.8. The left y-axis shows the burnout time as a function of adiabatic flame temperature T_{ad} (–o–). For lean conditions, the burnout time steeply increases to values that are far above gas turbine combustor residence times. The ratio of OH creation to CO oxidation is plotted using the second y-axis (–△–). For high adiabatic flame temperatures, the creation rate of OH is substantially higher than the oxidation rate of CO, and the hypothesis that the equilibrium of OH can be reached is apparently valid. As the adiabatic flame temperature decreases, the ratio approaches unity (indicated by ·····). A ratio of unity implies that every produced OH molecule is used for the oxidation of CO, as the creation of OH becomes the limiting factor. As mentioned before, the chemistry of OH is complex and hence difficult to model. Furthermore, the tabulation on the basis of detailed chemistry seems to be a potential solution. However, as it is discussed above, neither reactors nor flamelets are suitable downstream of the turbulent flame brush due to strongly increased OH.

A model for the prediction of the quenching event that is based on time scales is introduced in the following. Figure 4.9 shows the five most relevant reactions in which OH is involved for three different pressures for an equivalence ratio of $\phi = 0.3$. Note that the reaction analysis is repeated for an equivalence ratio of $\phi = 0.5$ in the Appendix B. The dominant reaction for all pressure conditions is the already introduced CO burnout reaction. Moreover, the creation of OH is mainly based on three reactions:

$$\begin{aligned} \mathrm{H} + \mathrm{O_2} &\longleftrightarrow \mathrm{O} + \mathrm{OH}, \\ \mathrm{HO_2} + \mathrm{OH} &\longleftrightarrow \mathrm{H_2O} + \mathrm{O_2}, \\ \text{and } \mathrm{H_2O} + \mathrm{O} &\longleftrightarrow 2\,\mathrm{OH}\ . \end{aligned} \tag{4.18}$$

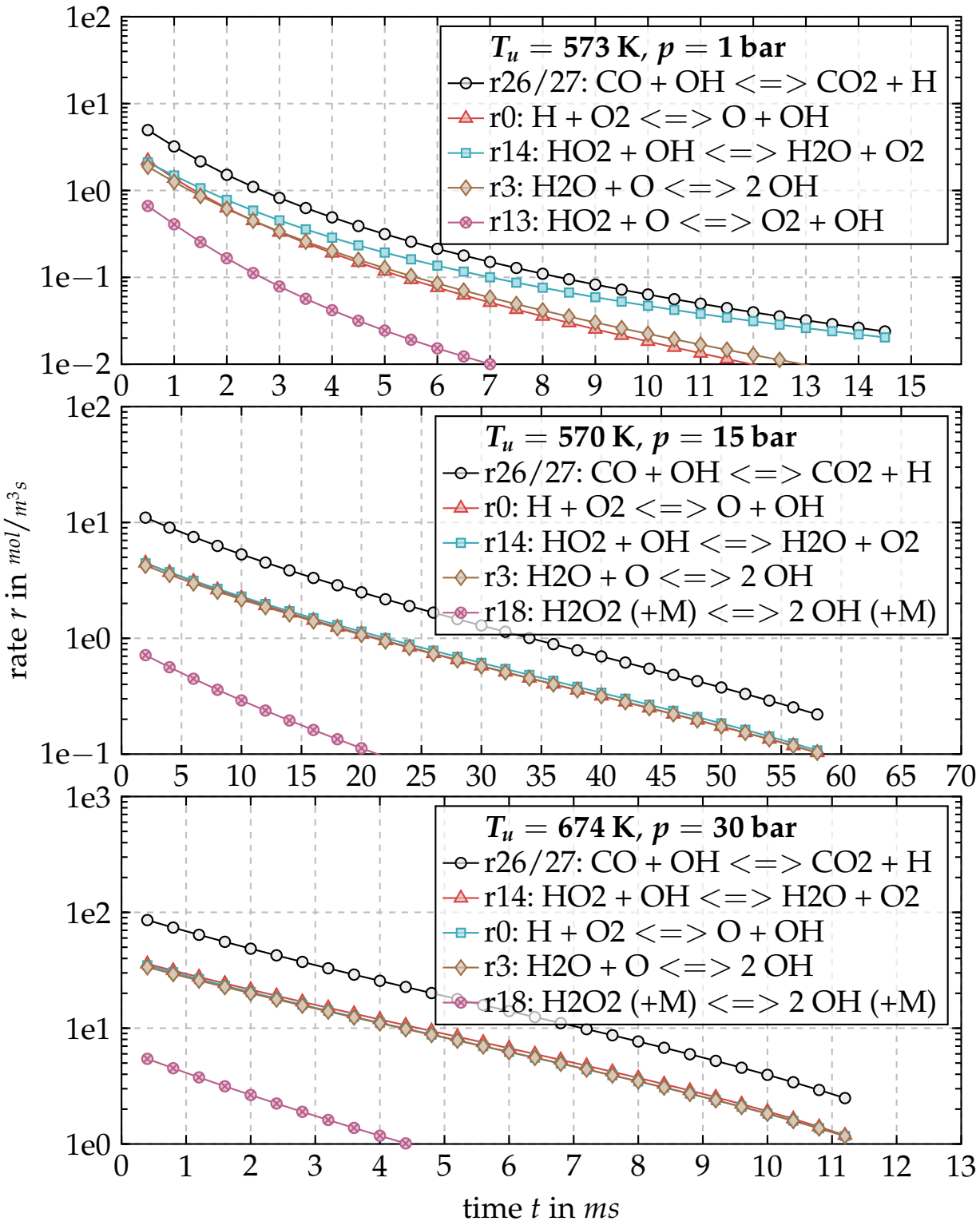

Figure 4.9.: Five most relevant OH reactions in the late burnout (constant pressure reactor at $\phi = 0.3$, calculated using GALWAY 1.3 [38] and CANTERA [34]).

In the following, it is assumed that all reactants on the left hand side of this set of equations are in equilibrium. The burnout of CO does not significantly alter O_2 and water (H_2O) as both species are available in abundance. Fast time scales can be assumed for the following radicals: Hydrogen (H), oxygen (O), and hydroperoxyl (HO_2). This leads to a model that allows to tabulate the OH creation rate $\dot{\zeta}_{cr,\mathrm{OH}}$ prior to the CFD simulation and to evaluate the OH creation time scale by using:

$$\tau_{cr,\mathrm{OH}} = \frac{[\mathrm{OH}]}{\dot{\zeta}_{cr,\mathrm{OH}}} \,. \tag{4.19}$$

$\tau_{cr,\mathrm{OH}}$ is the built-up time for the equilibrium value of OH assuming the simplified creation rate. Furthermore, a dimensionless identifier is employed that describes the relationship between the time scales for OH creation and CO oxidation:

$$\zeta_{\mathrm{OH}} = \frac{\tau_{cr,\mathrm{OH}}}{\tau_{ox,\mathrm{CO}}} \,. \tag{4.20}$$

A critical value of unity is used throughout the present work as this value implies the point at which CO oxidation exceeds OH creation.

4.6. Application and Validation

The CO modeling strategy is implemented in the software presented in Appendix A in addition to the combustion model. The model-specific flow of information is shown in Figure 4.10.

In the following, the application of the proposed CO model is shown. In the first Section 4.6.3, the model's capability of dealing with specific situations that are relevant for gas turbines at part load are demonstrated. For this purpose, a generic geometry featuring annularly distributed jet flames is employed. In addition, experiments in an atmospheric single-burner test rig have been carried out. The test rig has an unique combustion chamber design that allows the measurement of locally resolved CO distributions. Validation of the atmospheric test rig is presented in Section 4.6.1. The last Section 4.6.2 shows the application of the model to the GT11N's silo combustor that comprises 37 burners. Two cases are

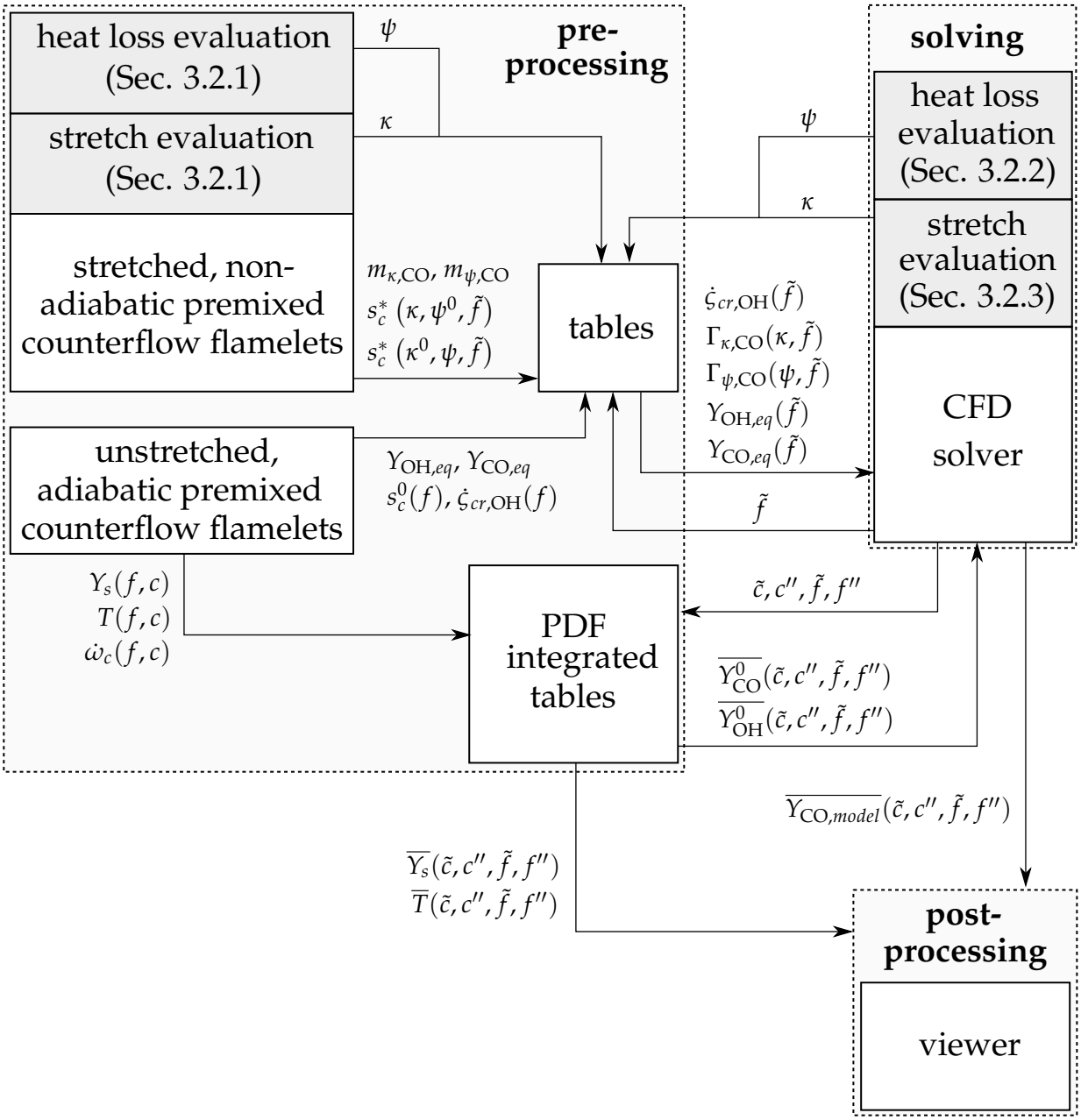

Figure 4.10.: Simplified overview of the CO model.

validated that differ in pressure and size. Moreover, both cases employ different concepts of fuel staging.

4.6.1. Atmospheric Single-Burner Test Rig

A novel combustion chamber design has been developed that allows the local measurement of CO. Note that locally resolved CO distributions are

a great benefit for this work as they allow to validate all models individually and are not limited to the validation of global quantities. An example for the individual validation of a submodel can be found in Section 4.3 in which the CO source terms that are calculated by the post-flame model are compared to the experimental source terms. Figure 4.11 illustrates the geometry of the combustion chamber. Preheated air flows through the burner into the combustion chamber. Swirl is induced by a downscaled version of the A^{2}EV burner that has already been introduced in Section 3.3. Natural gas is supplied by injectors that are located within the four burner slots. Moreover, a fraction of the preheated air bypasses the burner and flows directly into the combustion chamber through 48 holes ($d = 2.5\,\mathrm{mm}$) that are drilled in the front plate close to the burner exit. The ratio between primary to secondary air is passively controlled by the ratio of friction factors of the primary and secondary air paths. While the friction factor of the burner (primary air path) can be measured by a differential pressure measurement, the friction factor of the secondary air path is a design parameter. The proposed geometry results in a primary to secondary air split of $\dot{m}_{0,sec}/\dot{m}_{0,pri} = 43\,\%$ that could be verified in a CFD simulation. Within the combustion chamber, the swirling flow breaks down and generates a recirculation zone in the center. The turbulent flame brush stabilizes at the stagnation point near the burner exit. The conditions in the strongly diluted outer regions of the turbulent flame brush lead to CO emissions. Ceramic insulation is employed in order to avoid significant heat losses. Furthermore, local measurements are conducted using a water-cooled probe. A gas analyzer determines the mole fractions of CO_2, O_2, NO_x, and CO from the extracted gas samples. The probe can be attached to multiple ports that differ in axial distance to the front plate. In addition, the probe can be traversed radially. These two degrees of freedom allow the measurement of two-dimensional distributions. As the chamber is rotational symmetric, a two-dimensional plane sufficiently represents the three-dimensional topology.

Table 4.1 summarizes the numerical setup. Simulations are conducted in a periodic quarter of the chamber without the complex burner geometry. Profiles at the burner exit are retrieved from a simulation of the full geometry that comprises plenum, burner, and chamber. The thermal boundary condition of the wall is modeled by FLUENT. The heat flux is evaluated by

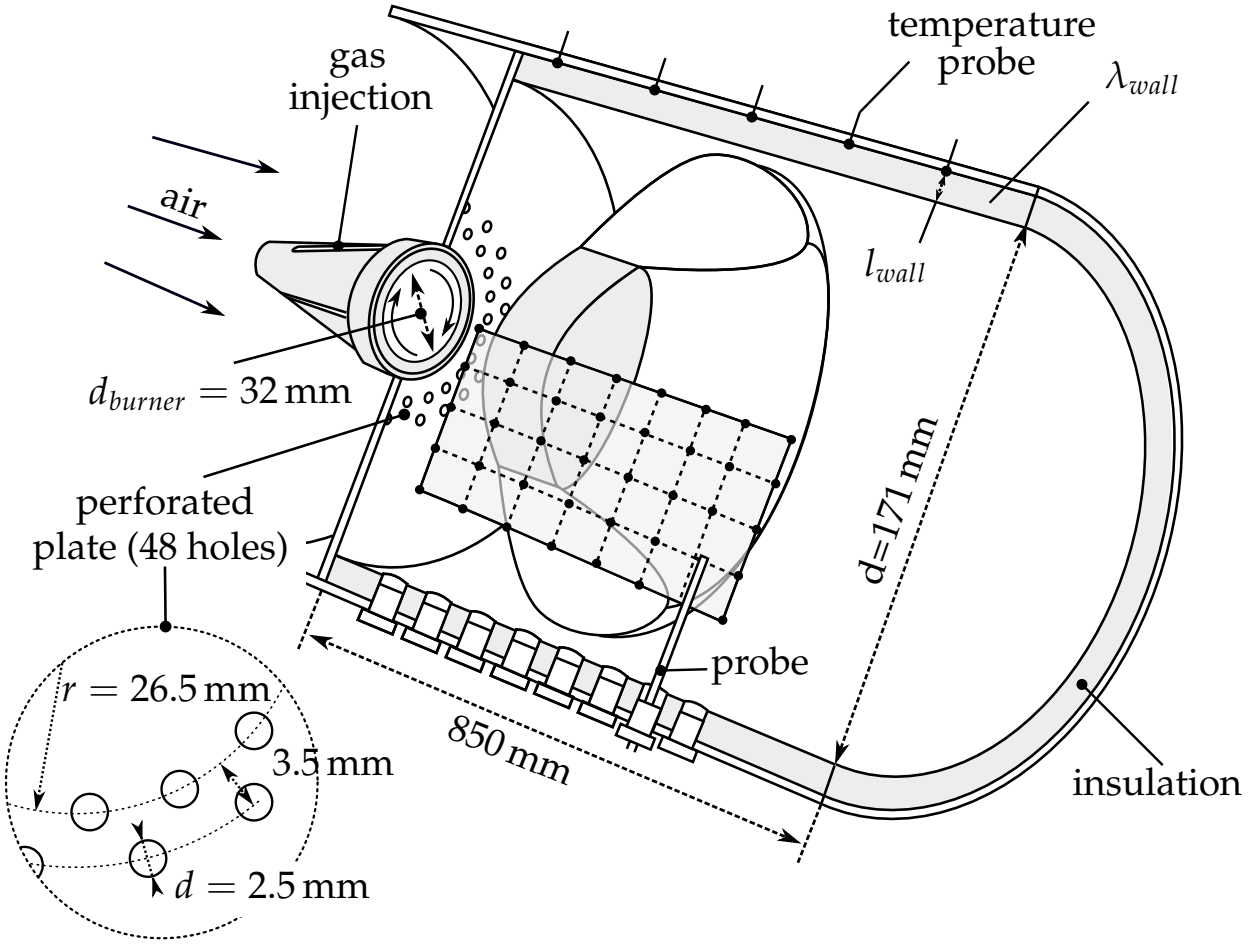

Figure 4.11.: Illustration of the atmospheric single-burner test rig.

considering the thermal conductivity of the insulation ($\lambda_{wall} = 0.15\,\text{W/mK}$) and the distance to the temperature measurement probes ($l_{wall} = 2.8\,\text{cm}$) that are attached as depicted in Figure 4.11. Figure 4.12 shows the velocity $\tilde{u}$ in the upper half. The velocity distribution indicates that the secondary air jets are able to penetrate the burner flow. The mixture fraction $\tilde{f}$ is shown in the lower half of Figure 4.12. The significant dilution by secondary air is evident. Numerically predicted CO distributions are shown in Figure 4.13. Moreover, the corresponding model zones are illustrated in Figure 4.14. Results for five different adiabatic flame temperatures T_{ad} are shown. Reactivity reduces for decreasing adiabatic flame temperature and the turbulent flame brush (▫) moves downstream. CO emissions clearly rise as the adiabatic flame temperature T_{ad} decreases. The model describes the rise in CO emissions by the following three mechanisms:

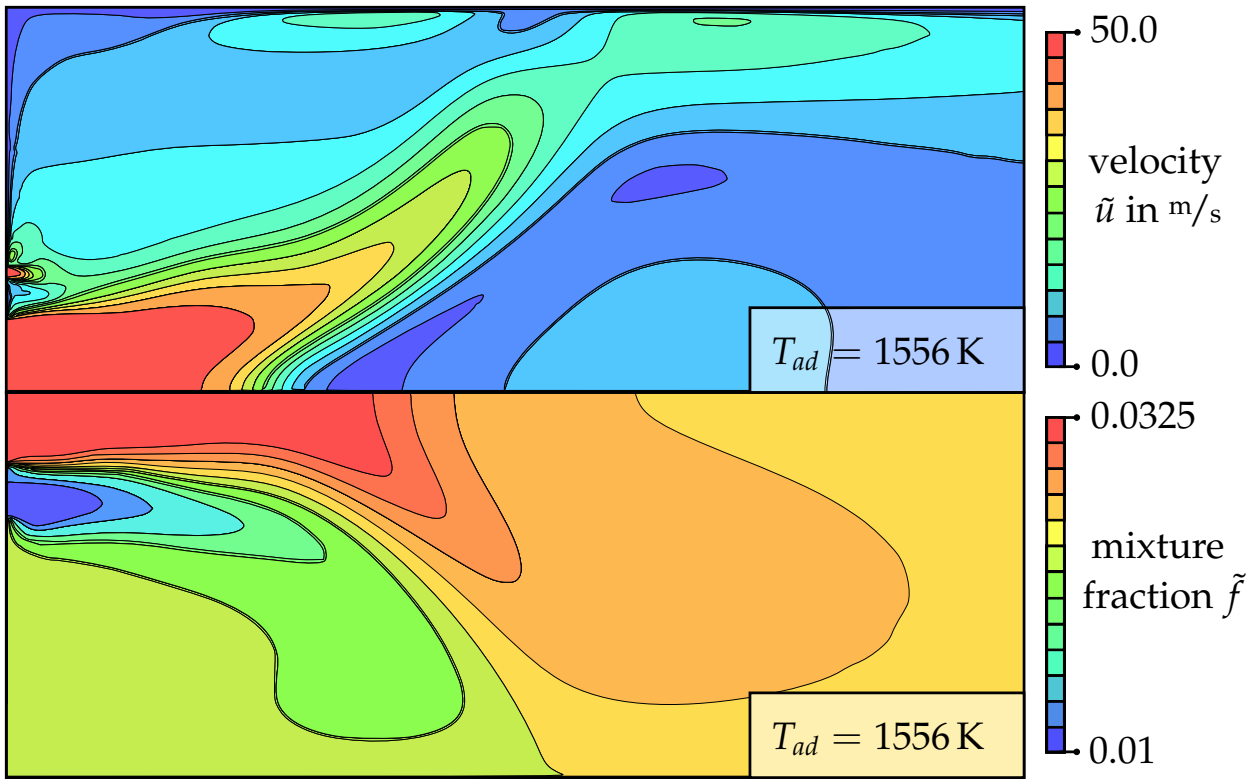

Figure 4.12.: Contour plots of velocity $\tilde{u}$ (upper half) and mixture fraction $\tilde{f}$ (lower half) of the atmospheric single-burner test rig.

1. In the post-flame zone (▫), the temperature-dependent CO burnout rates are reduced for decreasing adiabatic flame temperatures (cf. Equation 4.13).

2. The transition from the in- to the post-flame model occurs at higher CO due to an increased characteristic chemical time scale for CO oxidation $\tau_{ox,\mathrm{CO}}$ (cf. Equations 4.15, 4.16, and 4.17).

3. Quenching (▫) becomes more dominant with decreasing adiabatic flame temperature T_{ad}. This proves that the time scale for OH creation $\tau_{cr,\mathrm{OH}}$ (cf. Equation 4.19) increases faster than the time scale for CO burnout $\tau_{ox,\mathrm{CO}}$ (cf. Equation 4.16) for colder conditions (cf. Equation 4.20).

In the following, the numerically predicted CO emissions are validated with the experimentally obtained data. It is reasonable to compare surface-averaged quantities as probe positions at high radii represent

Table 4.1.: Summary of the numerical setup for the atmospheric single-burner test rig.

boundary conditions	
T_∞	341 K
T_u	573.15 K
λ_{wall}, l_{wall}	0.15 $^{\mathrm{W}}/_{\mathrm{mK}}$, 2.8 cm
$\dot{m}_0$ (air)	32 $^{\mathrm{g}}/_{\mathrm{s}}$
$\dot{m}_{0,sec}$ (air)	30.2 % of $\dot{m}_0$
T_{ad}	1521-1676 K
CFD setup	
software	FLUENT v. 18.0 [77]
turbulence model	k-ϵ realizable
$Sc_t / Da_{\mathrm{CO},crit} / \zeta_{\mathrm{OH},crit}$	0.7/1/1
mesh type	polyhedral
mesh size (chamber only)	2.4e5 cells
table generation	
kinetic	GALWAY 1.3 [38]
discrete points of $c/f/\psi/\kappa$	50/50/5/$\approx$5
m_κ / m_ψ	2.38/0.38
$m_{\kappa,\psi}$	1.87

larger surfaces than locations at low radii. Thus, each measured value of CO is multiplied with the surface of its corresponding annulus. Furthermore, the products of all radii are summed up and divided by the total surface:

$$\langle X_{\mathrm{CO},dry} \rangle = \frac{\sum_{an} A_{an} \langle X_{\mathrm{CO},dry} \rangle_{an}}{\sum_{an} A_{an}}. \tag{4.21}$$

Figure 4.15 shows the plot of measured CO mole fractions X_{CO} (–o–) as a function of adiabatic flame temperature T_{ad} for three different residence times. Residence times are estimated in a corresponding CFD simulation. For this purpose, Lagrangian observers are simulated in order to create streamlines. Moreover, the corresponding residence times of fluid particle (represented by the Lagrangian observers) can be analyzed as a function of the location.

Using the CO model proposed in this chapter (–△–) leads to good agreement with the experimental data. The model performance apparently decreases for cold conditions. Note that the proposed model assumes that all intermediate species are in equilibrium and solely CO decreases during burnout. This assumption may be invalid for adiabatic temperatures that are below a critical limit. An example to this mechanism is given by the frequently observed occurrence of unburnt hydrocarbon emissions near the lean blowout limit. This model deficiency is not a major drawback as the numerical prediction of CO emissions is solely relevant for operating points that show emissions that are in the technically relevant range. Note that emission legislations are usually below 100 ppmv. In addition, Figure 4.15 shows the predictions by an adiabatic version of the CO model (–□–) in order to characterize the influence of heat loss on CO. Even though the ceramic insulation is able to avoid major heat losses, a significant decrease of CO is evident when non-adiabatic effects are not considered.

As it is discussed above, flamelet-based combustion models are not able to predict CO. This is argued by the assumption of infinitely thin reaction zones that cannot be used to describe the burnout of CO. Consequently, the combustion model (–◇–) wrongly predicts fully burnt out CO as the turbulent flame brush is located upstream of the measurement locations.

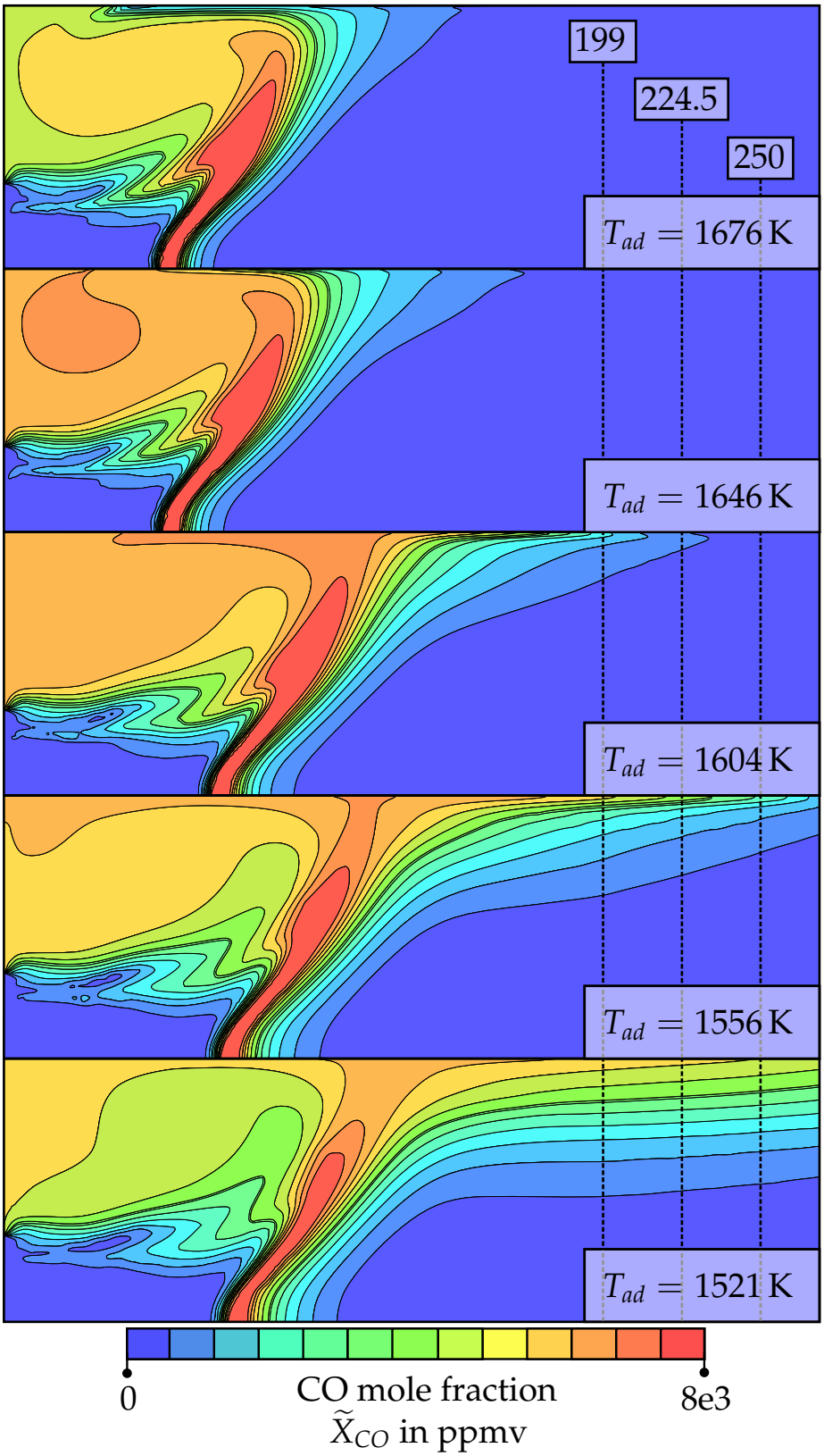

Figure 4.13.: Contour plots of CO mole fraction $\widetilde{X}_{CO}$ of the atmospheric single-burner test rig.

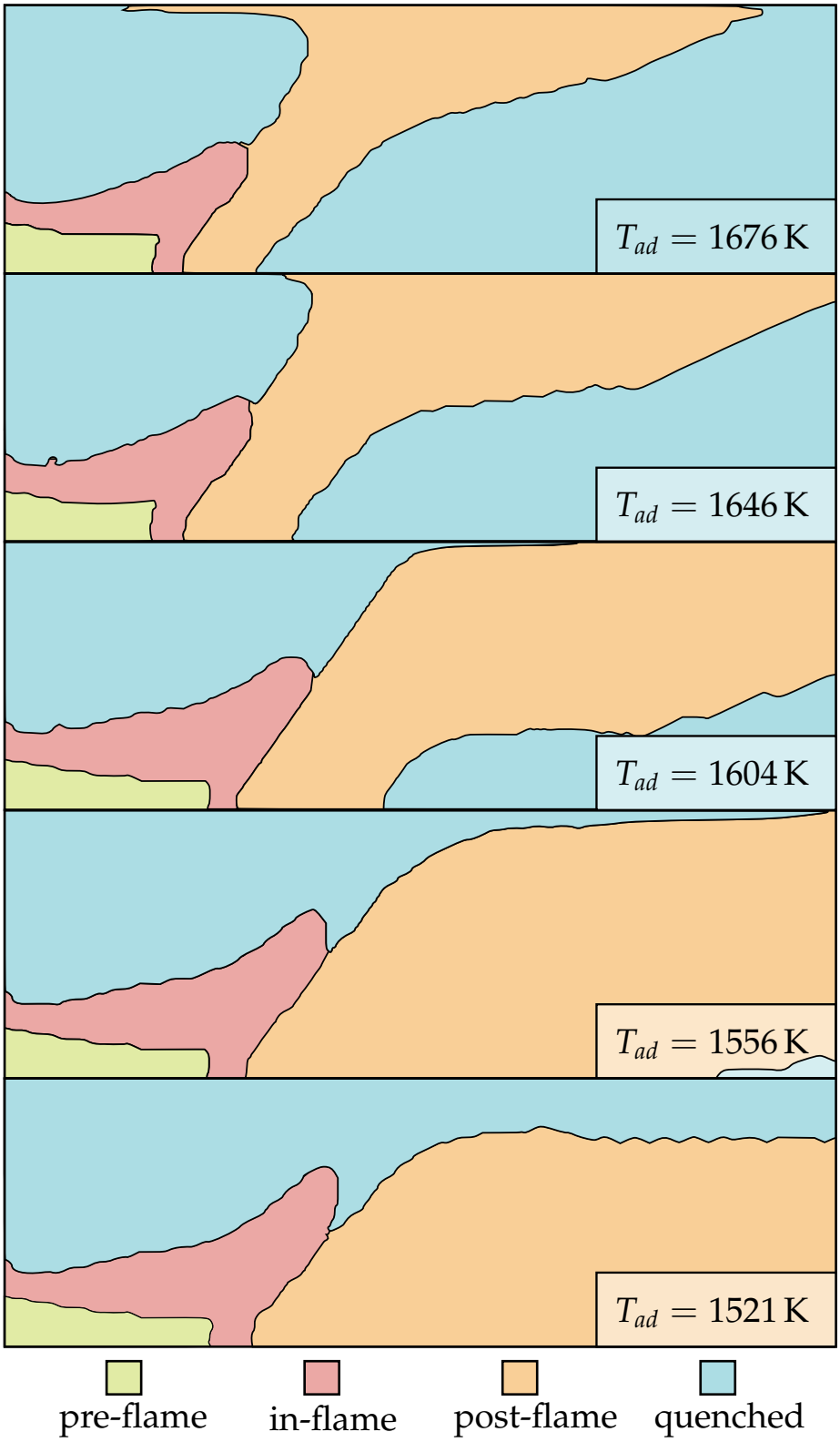

Figure 4.14.: Contour plots of the modeling zones of the atmospheric single-burner test rig.

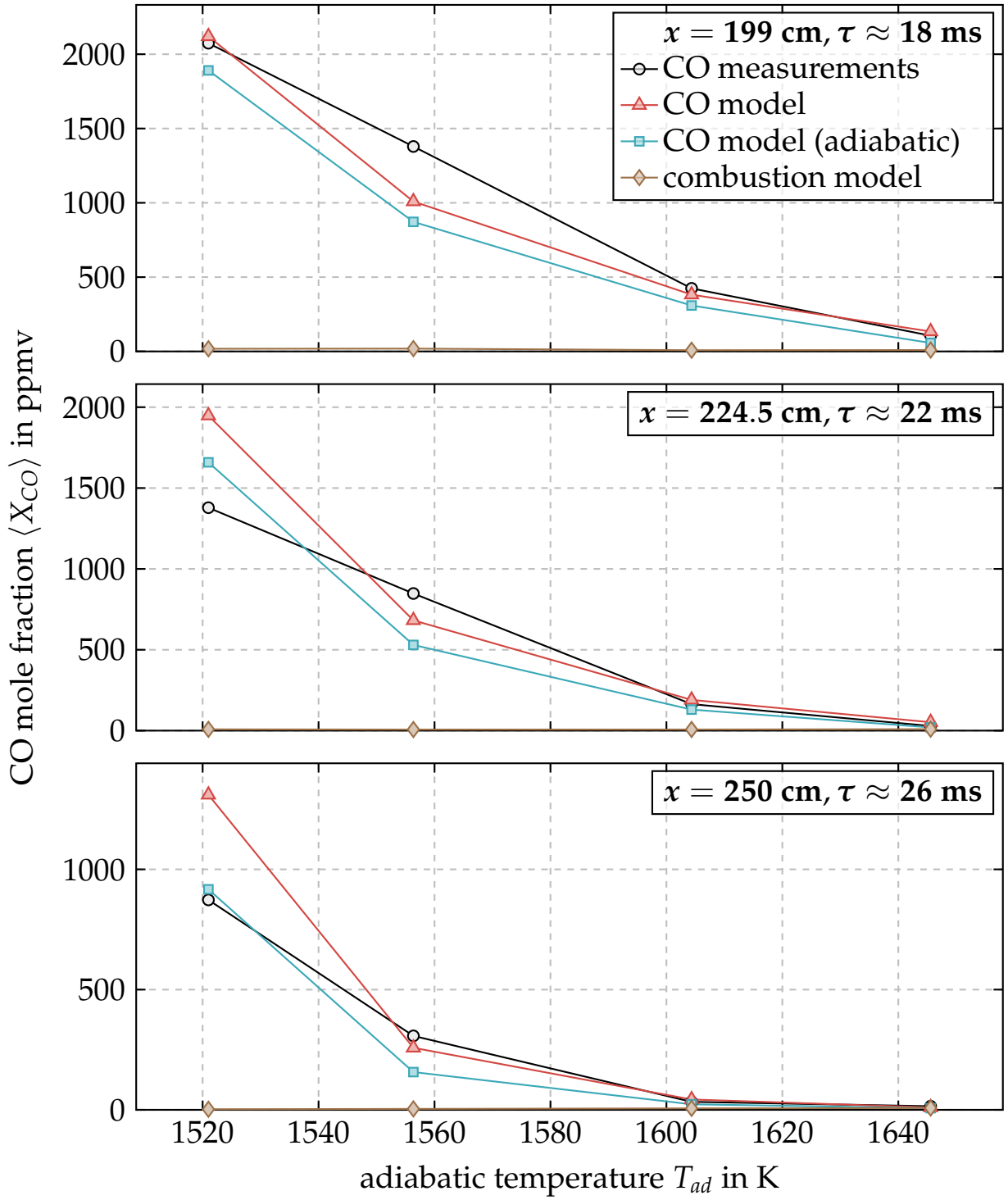

Figure 4.15.: Temperature dependent CO emissions of the atmospheric single-burner test rig, which is illustrated in Figure 4.11.

4.6.2. Multi-Burner Cases

Two multi-burner cases that employ fuel staging concepts are presented in the following. Both cases use the GT11N silo combustor geometry that comprises 37 burners, which is illustrated in Figure 4.16. In addition, the fuel staging concept of the atmospheric model is depicted. The first validation case is a down-scaled, atmospheric model of the GT11N. In addition, validation of a full-scale GT11N in field operation is presented. An overview of the numerical setups is given in Table 4.2. Both cases operate under part-load conditions in which solely a part of the total amount of burners is active. Multiple stages exist that differ in their number of active burners. A specified group of burners is switched off during the transition to a colder stage. By reducing the power to part load, several stages are passed and the number of burners is successively reduced. The decisive difference between both cases is the way fuel is reduced before a group of burners is switched off:

- **Atmospheric GT11N model:** A group of burners is ramped down from reference conditions to pure air. Variation of load during a stage is conducted by solely changing the fuel supply of the specific group that is intended to get switched off.

- **High-pressure GT11N in field operation:** The reduction of load is accomplished by decreasing the fuel supply for all active burners. This can be done until CO emissions increase to a specific limit. When this limit is reached, a group of burners that operates at stable conditions is abruptly switched off. The fuel surplus from the switched off burners is redistributed to the remaining group of active burners leading to a drop in CO emissions.

4.6.2.1. Atmospheric Model of the GT11N

The validation of a down-scaled, atmospheric model of the GT11N is presented in the following. The experimental data are retrieved from an unpublished, company-internal measurement study that was conducted in order to find reasonable fuel staging strategies for silo combustors. In the report, the optimal concept for part-load operation is investigated

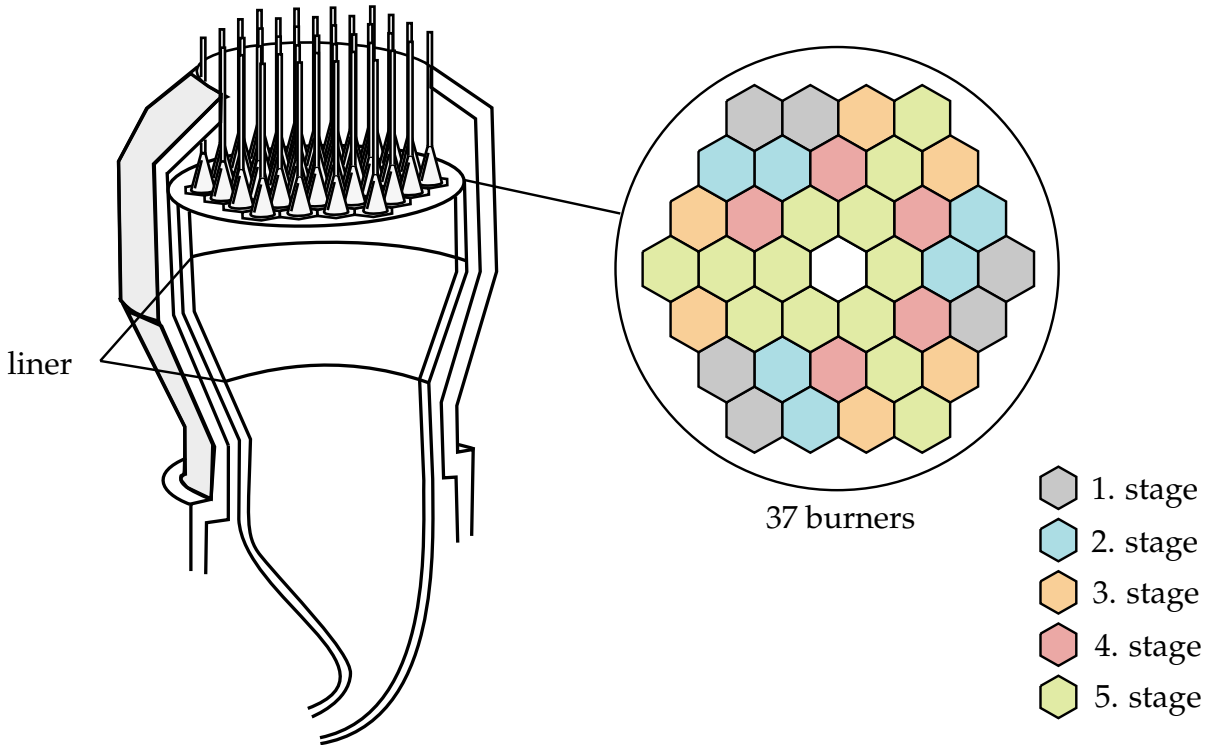

Figure 4.16.: Illustration of of the GT11N (inspired by Vorontsov et al. [22]) with fuel staging concept of the atmospheric GT11N model.

in terms of how the burners should be grouped and in which order the groups should be phased out when reducing the load. The burner grouping is depicted in Figure 4.16. It is important to note that this burner grouping is not a reasonable strategy for real gas turbines and should be interpreted as a benchmark test in terms of CO emissions. For example, the last group of burners that remains active for the coldest conditions (stage 5) is the most critical group. A reasonable strategy would be to locate the active burners of stage 5 in a way that the number of cold neighbors is minimized. However, the burners of stage 5 are relatively distributed, have many cold neighbors, and are hence not optimal in terms of CO emissions in part load.

Unfortunately, the exact geometry of the atmospheric model of the GT11N is not available. However, the geometry of the full-size GT11N is employed and geometrically scaled down to fit the combustion cham-

ber's diameter of the atmospheric model. The geometry comprises the plenum, all burners, the combustion chamber, and the transition piece.

CO mole fraction X_{CO} as a function of adiabatic flame temperature T_{ad} is plotted in Figure 4.17. Four stages are indicated. In each stage, a specified group of burners is ramped down from reference conditions to pure air. The hot conditions of the first stage lead to fast CO burnout. Hence, measured CO (–o–) as well as modeled CO (–△–) are close to equilibrium. In the second stage, CO emissions rise by reducing the fuel supply of the specified group of burners (⊠) from 100 % to 50 %. This mechanism is shown by the first two contour plots of Figure 4.18. Moreover, reducing the fuel supply from 50 % to 0 % leads to a decrease of CO emissions. Here, the specified group of burners operates below lean blowout limit and are piloted by the active group (⊠). This mechanism is shown in the third contour plot of Figure 4.18. The decline in CO with decreasing fuel supply is based on the mechanism that the amount of carbon atoms decreases with fuel supply. The third stage also shows an increase of CO emissions when the burners are reduced in fuel supply. A decisive difference between the second and the third stage is that the global CO emissions do not decline after the specified group of burners is phased out. At this point, the burnout of the active burners cannot be achieved anymore. In the fourth stage, the typical rise and fall of CO emissions during the process of phasing out a group of burners is shown. The proposed CO model strategy is capable of meeting the global CO measurements of the second and third stage. In the fourth stage, experimental CO declines after a local maximum was reached. The experimental profile of the fourth stage cannot be predicted by the proposed modeling strategy as CO proceeds rising instead of dropping as it is observed in the experiments. CO predicted by the combustion model (–□–) is again tremendously underestimating global CO.

Table 4.2.: Summary of the numerical setup for the multi-burner cases.

CFD setup	
software	FLUENT v. 18.0 [77]
turbulence model	k-ϵ realizable
$Sc_t / Da_{CO,crit} / \zeta_{OH,crit}$	0.7/1/1
mesh type	tetrahedral
mesh size	1.9e7 cells
table generation for the atmospheric model	
kinetic	GALWAY 1.3 [38]
discrete points for $c/f/\psi/\kappa$	50/40/10/≈6
m_κ / m_ψ	2.35/0.37
$m_{\kappa,\psi}$	1.86
table generation for the GT11N in field operation	
kinetic	GALWAY 1.3 [38]
discrete points of $c/f/\kappa$	50/40/≈19
m_κ	2.94
$m_{\kappa,\psi}$	1.84

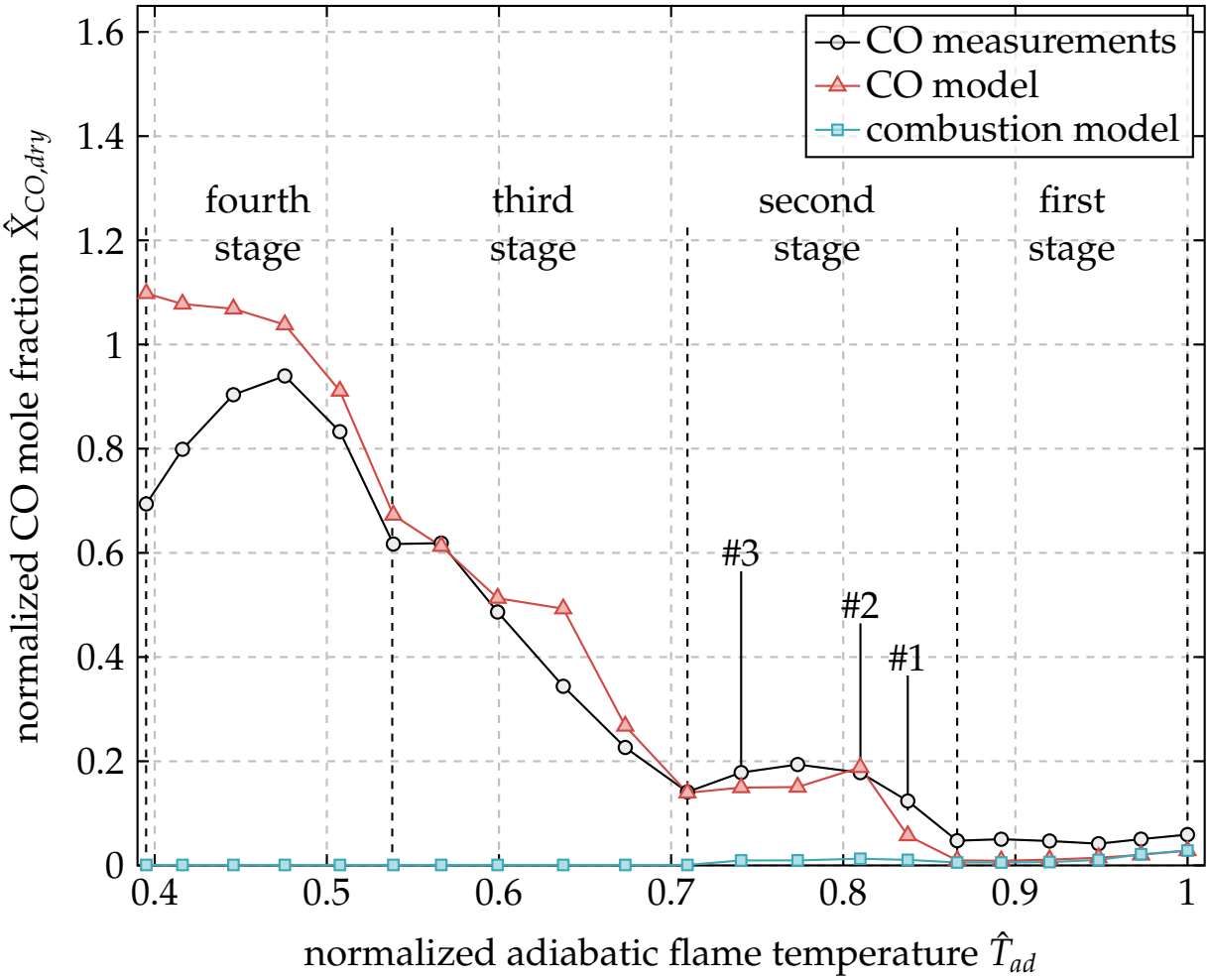

Figure 4.17.: Temperature dependent CO emissions of the atmospheric GT11N model.

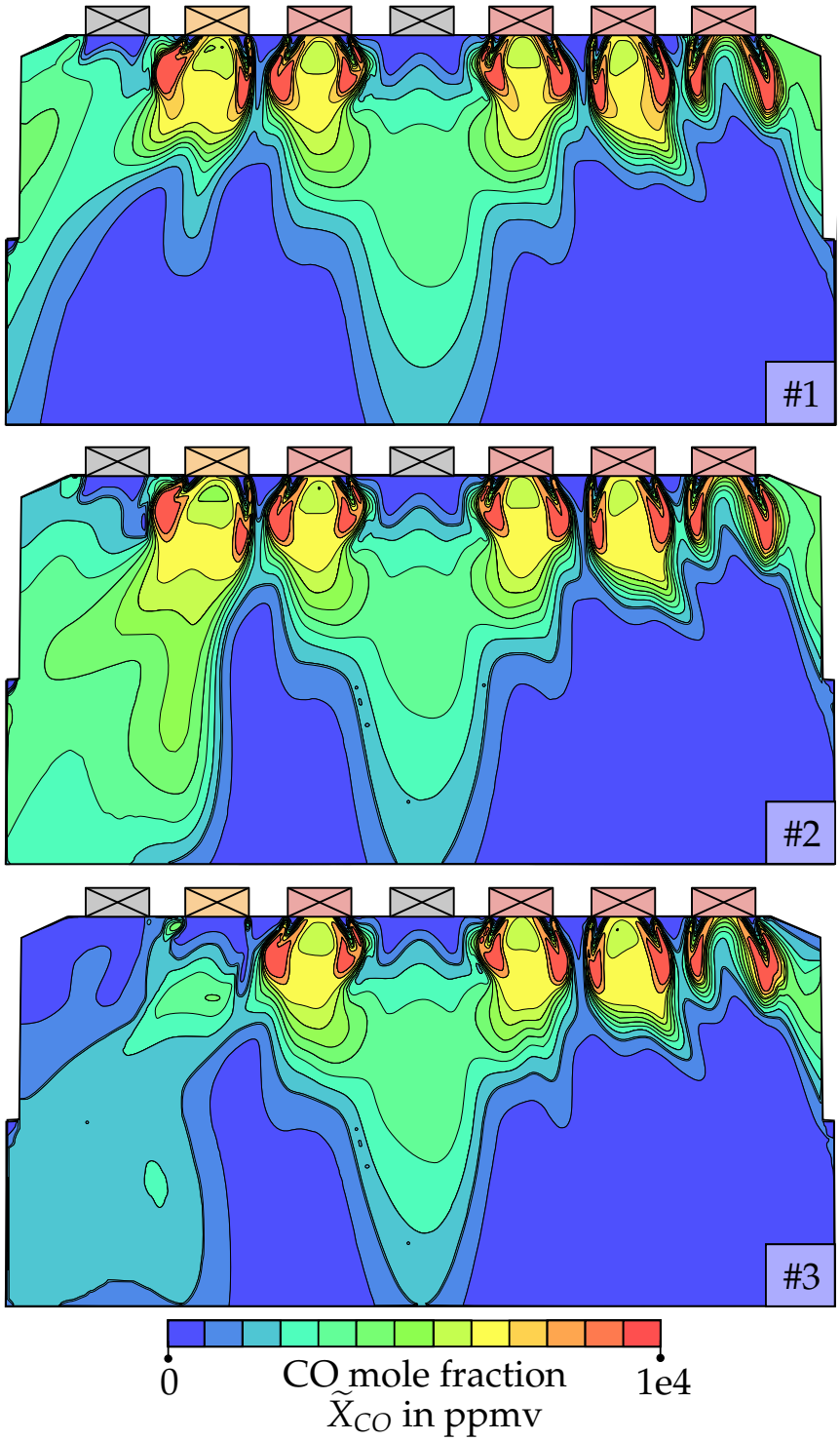

Figure 4.18.: Contour plots of CO mole fractions $\widetilde{X}_{CO}$ of three characteristic loads of the atmospheric GT11N model.

4.6.2.2. High-Pressure GT11N in Field Operation

The burner layout that is used in the high-pressure case is illustrated in Figure 4.19. 31 single switchable burners are belonging to the main group (⬢). The central burner is not active for the operating points that are considered in this study. Burners of the piloted group (⬢) are located in each corner. Piloted burners are supplied with substantially less fuel than burners that belong to the main group. Figure 4.21 demonstrates the interaction between the two groups. The first contour plot shows the laminar flame velocity s_l. It can be seen that burners of the piloted group (⊠) are operated with laminar flame velocities that are close to zero and are thus not able to provide a stable flame. Nevertheless, burnout can be achieved as adjacent active burners from the main group (⊠) are able to burnout the cold flow of the piloted group. The second contour plot of Figure 4.21 shows the interaction of active burners with an inactive burner (⊠) that is located in the center. It is apparent that the cold central burner has a strong impact on the CO emissions. The third contour plot shows the result when the quenching model is deactivated in order to demonstrate its significant impact on CO oxidation.

Validation is performed by comparing modeled with measured CO emissions as function of adiabatic flame temperature T_{ad} in Figure 4.20. Numerical results (–△–) are in good agreement with the measured data (–○–). The proposed modeling strategy is apparently able to quantitatively predict the absolute CO emissions, as well as the influence of burner switch-off events on CO. A decreased model accuracy can be observed in very lean conditions that was already discussed above. Additionally, predictions from the flamelet-based combustion model are plotted (–□–). As expected, the flamelets do not reach the combustor's outlet and CO is drastically underestimated.

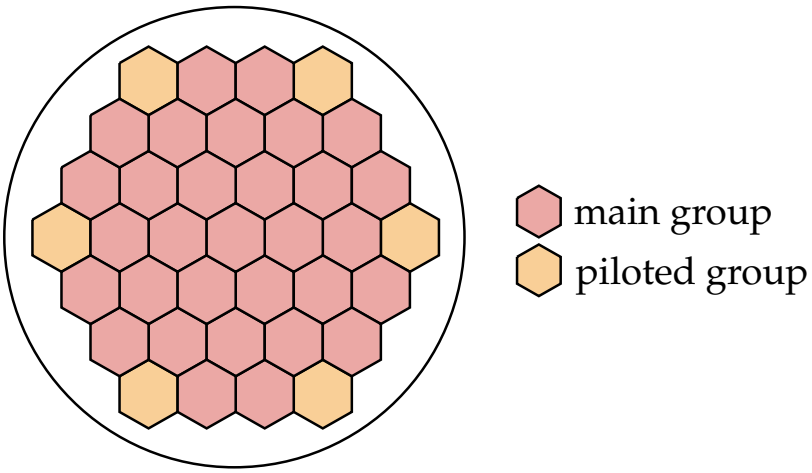

Figure 4.19.: Burner layout of the high-pressure GT11N in field operation.

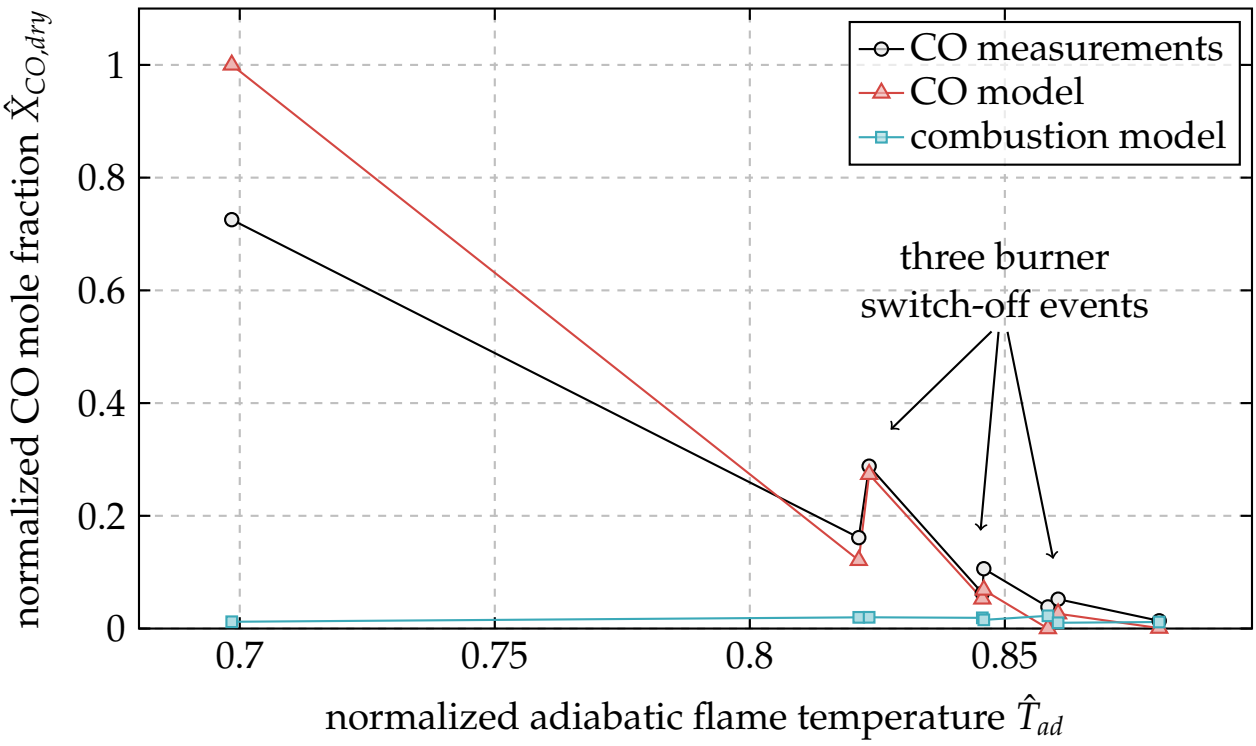

Figure 4.20.: Temperature dependent CO emissions of the high-pressure GT11N in field operation.

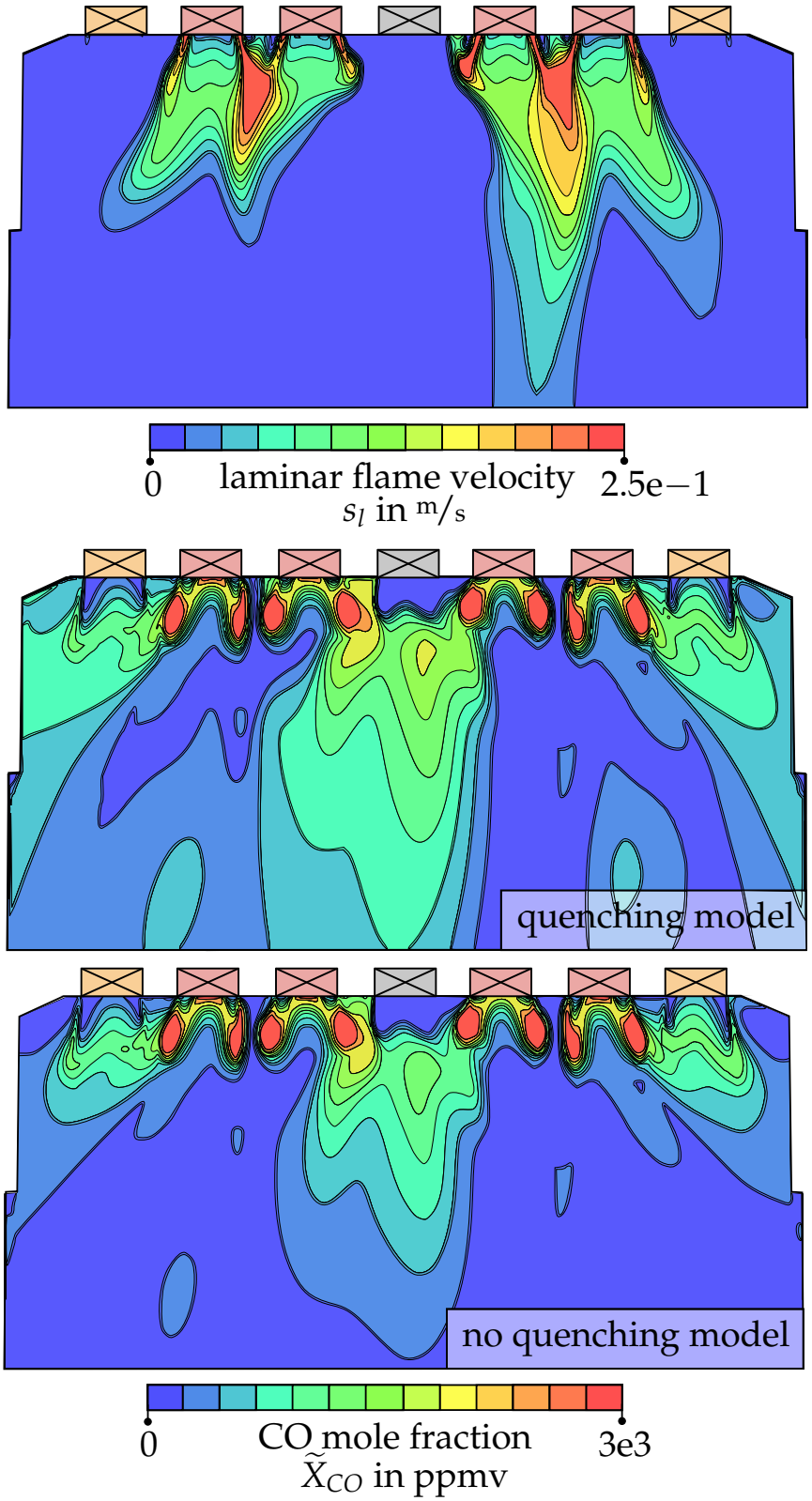

Figure 4.21.: Contour plots of the high-pressure GT11N in field operation.

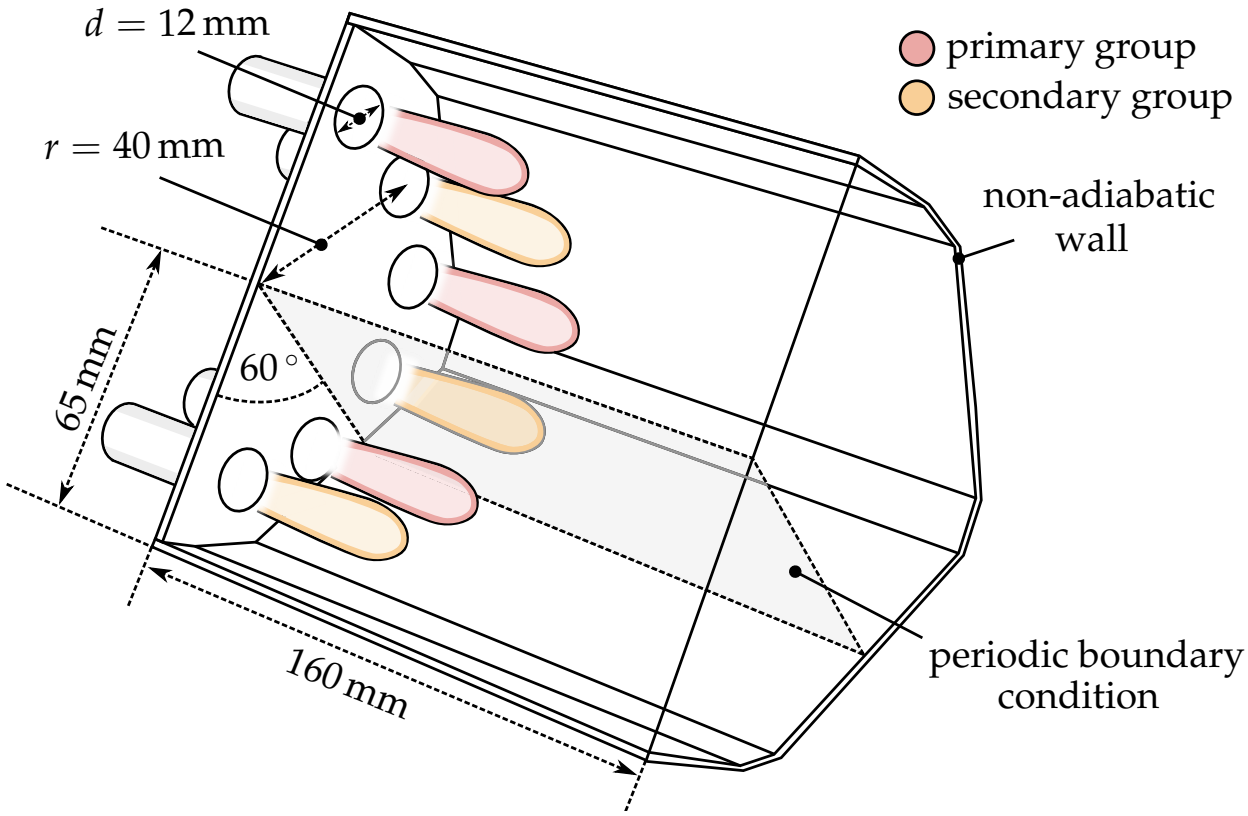

Figure 4.22.: Illustration of the novel combustor concept that is inspired by Lammel et al. [90]).

4.6.3. Application to a Novel Combustor Concept

Figure 4.22 illustrates the in this section used geometry that is inspired by Lammel et al. [89]. Annularly distributed inlets supply jet flames that are close enough to each other to feature intense flame interaction. All nozzles have a diameter of 12 mm and are located at an distance to the combustor center of 40 mm. The combustor's diameter is 130 mm and has a length of 160 mm. Note that the boundary conditions are retrieved from Lammel et al. [90]. The combustor is operated at a reference pressure of $p = 8\,\text{bar}$. Moreover, fuel is a mixture of CH_4 ($X_{CH_4,1} = 0.6$) and dihydrogen (H_2) ($X_{H_2,1} = 0.40$). Heat loss is imposed by considering an infinitely thin wall, an outer heat loss coefficient of $\alpha = 50\,\text{W/m}^2\text{K}$ and an ambient temperature of $T_\infty = 300\,\text{K}$. Further details of the boundary conditions and the numerical setup are summarized in Table 4.3.

Table 4.3.: Summary of the numerical setup for the novel combustor concept.

boundary conditions	
p	8 bar
$X_{H_2,1}$	0.4
$X_{CH_4,1}$	0.6
$T_{u,0}$	725 K
$T_{u,1}$	373 K
T_∞	300 K
α	50 $^{W}/_{m^2K}$
u_{jet}	105 $^{m}/_{s}$
T_{ad}	1333-1907 K
CFD setup	
software	FLUENT v. 18.0 [77]
turbulence model	k-ϵ realizable
$Sc_t / Da_{CO,crit} / \zeta_{OH,crit}$	0.7/1/1
mesh type	tetrahedral
mesh size	3.7e6 cells
table generation	
kinetic	GALWAY 1.3 [38]
discrete points of $c/f/\psi/\kappa$	50/38/10/≈10
m_κ / m_ψ	-0.19/0.3
$m_{\kappa,\psi}$	1.38

4.6.3.1. The Influence of Swirl on CO Emissions

The influence of swirl on CO emissions is investigated by comparing jet flames with swirl flames. Swirl is imposed by using profiles of the A_2EV burner that are scaled down to the nozzle's diameter. It is worth noting that the axial velocity component of the swirled flow equals the jets in order to realize the same mass flows in both configurations. In Figure 4.23, the resulting distributions of CO mole fraction X_{CO} is shown for both configurations. The flow topology substantially changes when swirl is imposed. While the jet flames show a heat release zone that is located in the center of the combustor, the turbulent flame brush of the swirled case stabilizes close to the burner exit. It is evident that the swirled case is beneficial in terms of burnout as the residence time behind the flame is higher in comparison to the jet flames. In order to investigate CO emissions as a function of adiabatic flame temperature T_{ad}, fuel mass flow is decreased evenly for all burners. The corresponding results are plotted in Figure 4.24. A sharp increase in CO emissions occurs for both cases after the adiabatic temperature has fallen below a critical level. In both configurations, the residence time behind the flame is not long enough to fully burnout CO. The jet flame configuration (–o–) shows elevated CO when the adiabatic flame temperature T_{ad} drops below 1677 K. The swirl flames (–△–) show global CO that is in equilibrium for adiabatic flame temperature above 1620 K. Remarkably, CO emissions rise for both cases with a similar slope, although the flow topology differs significantly.

4.6.3.2. The Influence of Colder Neighbors on CO Emissions

As shown in the previous section, the unstaged jet configurations cannot be operated below a critical flame temperature of about 1600 K. In the following, the advantages of fuel staging are demonstrated by using the jet configuration. As mentioned before, lower global adiabatic flame temperatures can be realized by applying fuel staging concepts when a stable flame act as a premixed pilot in order to burn out flames that a reduced in fuel supply. This case aims to study the situation in multi-burner systems in which active burners interact with adjacent, colder burners. Two groups of burners are specified as shown in Figure 4.22. The secondary

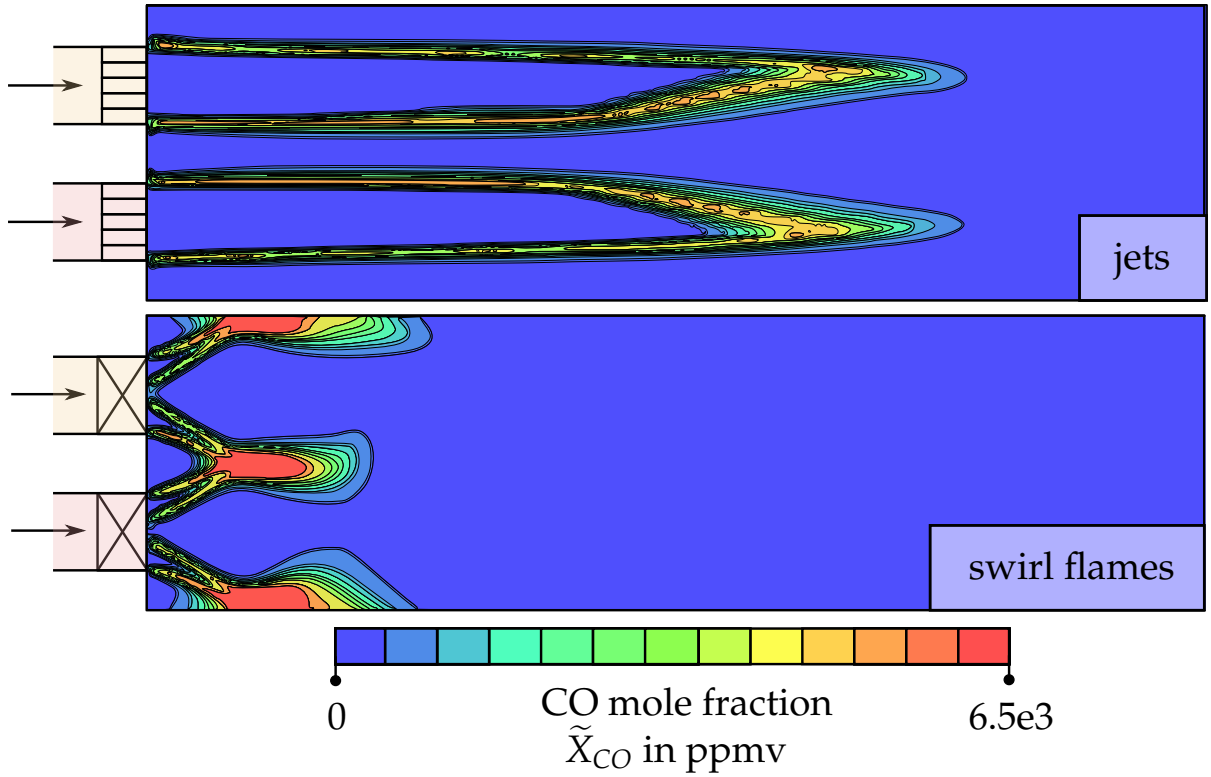

Figure 4.23.: Comparison of jet with swirl flames at an adiabatic temperature of $T_{ad} = 1620\,\mathrm{K}$ of the novel combustor concept.

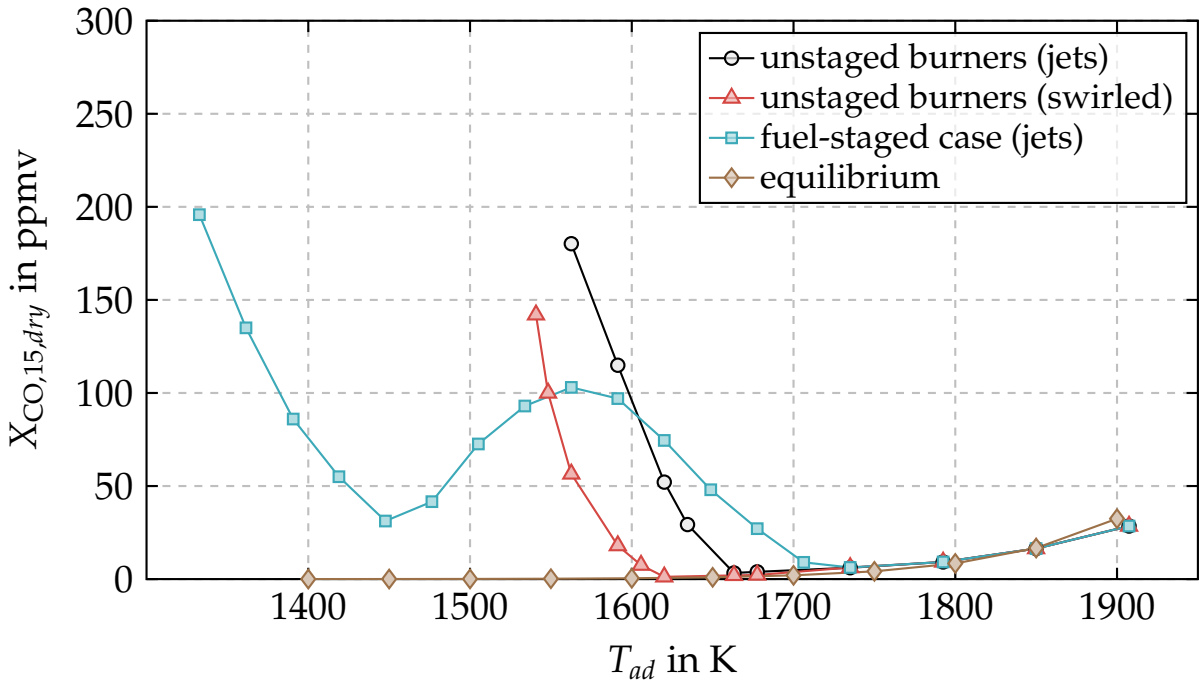

Figure 4.24.: Temperature dependent CO emissions of the novel combustor concept.

group (●) is ramped down from reference conditions to pure air. Note that the reference jets (●) that are not ramped down, operate at reference conditions at an mixture fraction that corresponds to an adiabatic flame temperature of 1907 K. Figure 4.24 shows a plot of the corresponding CO emissions (–□–). Moreover, the fuel-staged case is compared to the reference case in which both groups are evenly decreased in fuel (–○–). Complete burnout can be achieved in both cases for adiabatic flame temperatures above $T_{ad} = 1735\,\mathrm{K}$. Between 1605 K and 1735 K, the fuel-staged case shows moderately higher CO emissions than the reference case. CO emissions of the fuel-staged case rise faster due to a strongly increased flame length of jets from the secondary group. This mechanism is demonstrated by the second contour plot of Figure 4.25. Below an adiabatic flame temperature of $T_{ad} = 1605\,\mathrm{K}$, the strategy of fuel staging is beneficial over the reference case. The advantage is based on lean jets that operate below the lean blowout limit and are ignited by the fuel-rich jets that act as premixed pilots. Furthermore, the fuel-staged case has a minimum at 1447 K. The minimum develops due to a decreased amount of carbon atoms that need to be oxidized as shown by the third contour plot in Figure 4.25. Further reducing the fuel supply of the secondary group leads to lean quenching of the neighboring jets that belong to the primary group. The lean quenching leads to a steep increase in CO emissions as shown by the fourth contour plot in Figure 4.25.

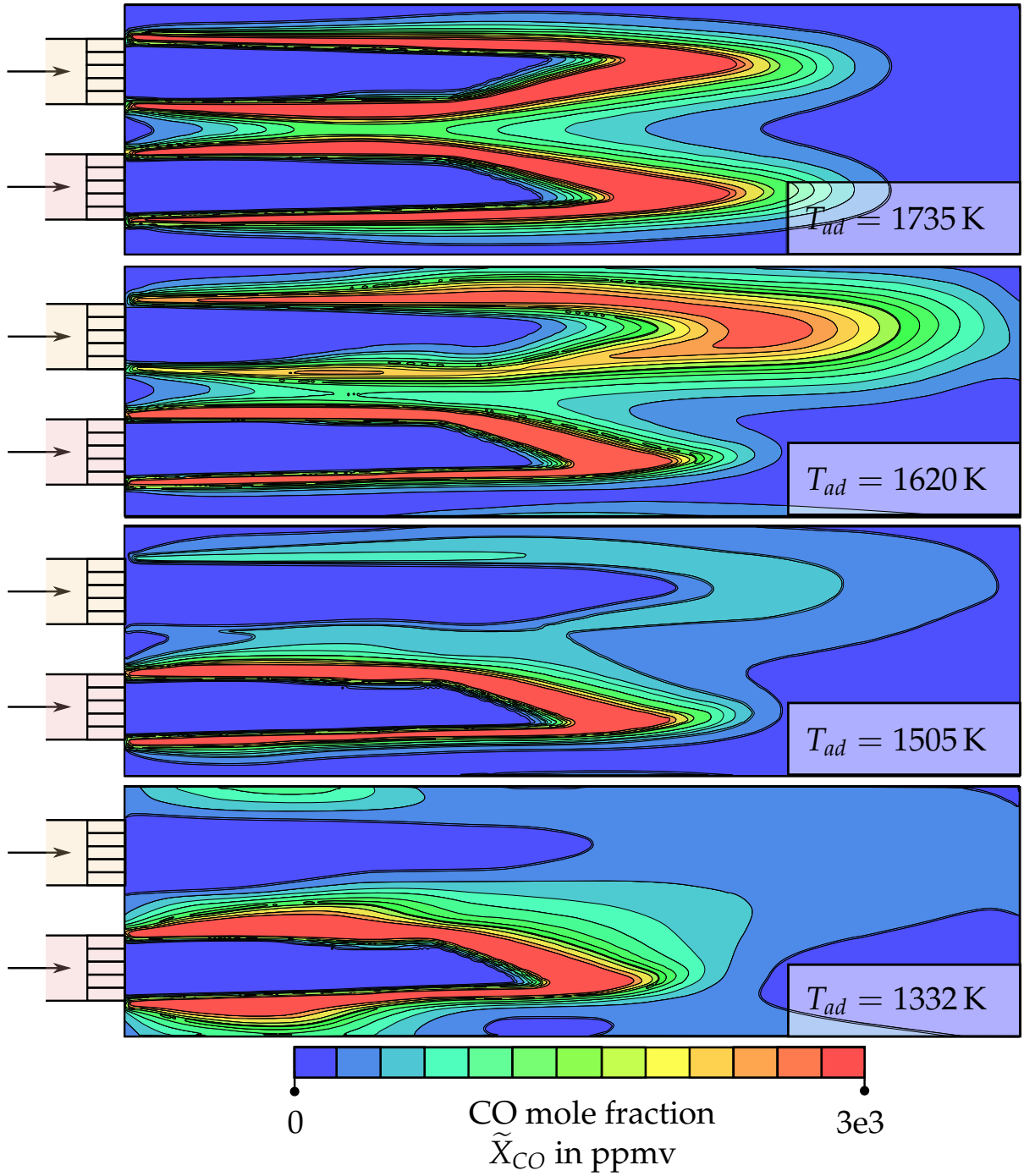

Figure 4.25.: Contour plots of CO mole fraction $\widetilde{X}_{CO}$ showing the interaction of jet flames with colder neighbors of the novel combustor concept.

5 Summary

This study investigates combustion and CO emissions in cold conditions that occur in gas turbines that operate at part load conditions. Although the prediction of CO emissions is a fundamental problem with many practical applications, no satisfying model has been published so far. As shown in this work, the inability of existing models to predict CO is based on two reasons:

- Combustion models often lack accuracy in cold conditions.
- In order to successfully predict CO emissions, a wide range of underlying time scales need to be considered.

The solution that is proposed in this work, solves both problems individually and hence comprises the following two parts:

Combustion modeling in turbulent, partially-premixed conditions is covered in the first part. The FGM theory is adopted in this work by employing manifolds that are generated by freely-propagating flamelets. The combustion process at cold conditions is demonstrated to be particularly susceptible for flame stretch and heat loss. An approach to efficiently consider both effects in the context of FGM is presented. For this purpose, an additional manifold is introduced that tabulates premixed counterflow flamelets at various enthalpy levels. The novel combustion modeling strategy is validated using experimental data from an atmospheric single-burner test rig. Key findings can be summarized by the following:

- Significant improvement in terms of flame shape and position is achieved by considering flame stretch and heat loss.

- The performance of the presented methodology is compared to the numerical predictions by EDM and TFC. Both standard combustion models and the original FGM formulation significantly overestimate chemical rates in regions that feature high flame stretch rates and/or heat loss.

The second part of this study investigates the formation and oxidation of CO. CO chemistry occurs in a wide spectrum of time scales leading to major challenges for the modeling approach. While the radical-driven chemistry within the turbulent flame brush occurs at short time scales, the burnout behind the heat release zone is based on significantly longer time scales. A novel strategy is presented that divides the domain in multiple zones by identifying the critical time scale that dominates CO chemistry. For each zone, a new model is developed to close CO:

- **In-flame zone:** A model is introduced that employs CO profiles from one-dimensional flamelet calculations and considers the influence of heat loss and flame stretch.

- **Post-flame zone:** Reduced chemistry is employed to close CO for kinetically-limited conditions.

- **Quenching zone:** The reasons for quenching are identified and modeled on the basis of chemical time scales.

The developed methodology is applied to various cases which lead to the following key findings:

- **Atmospheric single-burner test rig:** A test rig is introduced that was built to carry out experiments of a single swirl flame, which strongly interacts with secondary air. The test rig facilitates the measurement of locally resolved CO distributions, which allows to validate the in- and post-flame zone individually. The results of the validation can be summarized as follows:

  - The predicted CO is in good agreement with the experiments.

  - A decrease of the model's accuracy is observed for conditions that are close to the lean blowout limit.

  - CO predicted by the flamelet-based combustion model is shown to tremendously underestimate the experimental data.

- **Multi-burner systems with fuel staging concepts:** The modeling strategy is applied to two different multi-burner cases. In the first case, a down-scaled, atmospheric model of the GT11N silo combustor is employed. Moreover, the second case is a high-pressure, full-scale GT11N in field operation. Both cases employ fuel-staging strategies but differ in the way fuel is reduced before a group of burners is switched off. The main findings are summarized as follows:

  - The combustion model is not able to predict CO emissions.

  - The CO model's ability to meet global emissions is shown.

  - Characteristics from the fuel staging concepts are well captured.

- **Novel Combustor Concept:** The application of the proposed modeling strategy to a novel combustor concept is demonstrated. The test rig comprises twelve annularly distributed nozzles that supply strongly interacting flames. The model's capability to capture the following phenomena is shown:

  - The influence of swirl on CO emissions is investigated by comparing jet with swirl flames.

  - Advantages of fuel staging are discussed by comparing an unstaged with a staged case.

This work shows the first modeling strategy that is able to successfully predict CO emissions in a way that it can be practically used for the development of new combustors in the industry. Moreover, the following two key messages can be concluded from this work:

- Neglecting flame stretch and heat loss in cold conditions may significantly decrease the combustion model's accuracy.

- Modeling CO requires to develop models that are beyond the assumption of infinitely thin reactions zones.

A Software Implementation

A software package is written in order to provide a convenient solution for users to apply the models that are introduced in Chapter 3 and 4. In the following, details to the implementation are provided. Note that the model-specific flow of information was shown in the Figures 3.6 and 4.10. Figure A.1 provides a simplified overview of the two elements the software implementation consists of:

1. **Table Generator:** The proposed models are based on flamelet calculations that are performed by the Table Generator prior to the CFD simulation. Moreover, the solution of the flamelet simulations is stored in tables. An introduction to the Table Generator is provided in Section A.

2. **User Defined Function:** C-based User Defined Functions can be employed to extend the functionality of the commercial CFD software FLUENT [77]. During runtime, the solver executes the code in order to calculate the proposed modeling strategy. Details to the implementation of the User Defined Functions are provided in Section A.

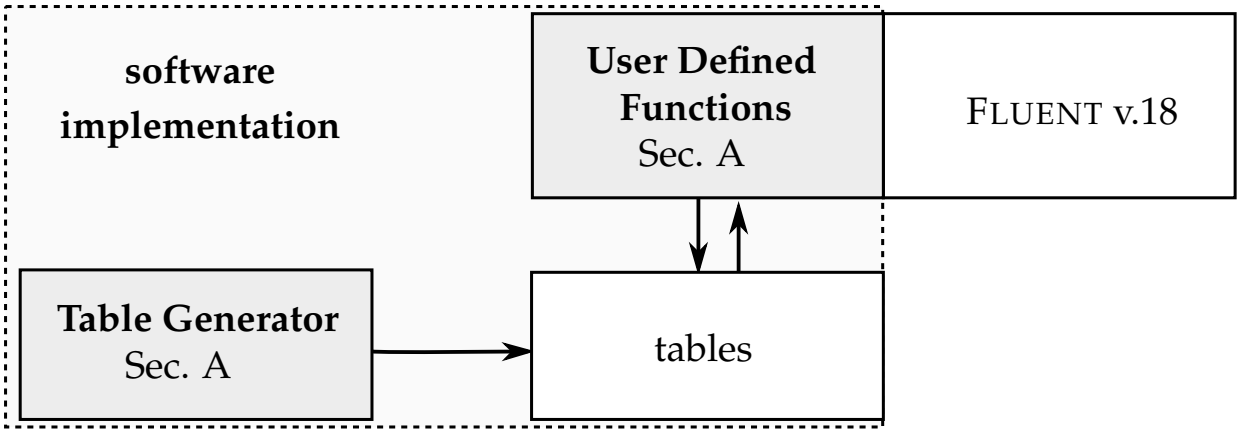

Figure A.1.: Overview of the software implementation.

A.1. Table Generator

The Table Generator creates libraries with up to three dimensions to account for different mixture fractions f, heat losses ψ, and strain rates κ. All libraries are based on premixed counterflow flamelets that are simulated with CANTERA by Goodwin et al. [34]. Parallelization is achieved by defining a number of work packages that are calculated individually as illustrated in Figure A.2. Each work package is responsible for a specific mixture fraction and processes the following three steps:

1. **Calibration:** Prior to the tabulation process, it is necessary to calibrate the domain length and the momentums of reactants and products in order to start the tabulation process at a strain rate that is negligibly small. For this purpose, a non-linear optimization method is implemented.

2. **Solving:** After the domain properties are calibrated, the flamelet simulations are performed for a two-dimensional grid of varying strain rates and enthalpy levels.

3. **Analysis & Tabulation:** Quantities are derived from the flamelet solutions and stored in thread-specific sub tables. After the last thread is finished, a merging routing is called in order to create the final tables.

The platform-independent Table Generator software is written in Python. A documentation is provided that comprises an installation guide as well as a tutorial. Moreover, a graphical user interface is created that is depicted in Figure A.3. In the upper half, the user can define the boundaries. First of all, the pressure needs to be set at which the flamelet calculations are performed. Furthermore, the temperatures of both oxidizer (mixture fraction f=0) and fuel (mixture fraction f=1) need to be specified. The user can choose from a set of predefined kinetic mechanisms. In addition, the selection can be extended by adding further mechanisms as described in the corresponding manual that is provided in the software's documentation. In the second column, the mass fractions of oxidizer and fuel can be defined. Furthermore, the tabulation process is adjustable by changing the solver's options that are listed in the third column. For in-

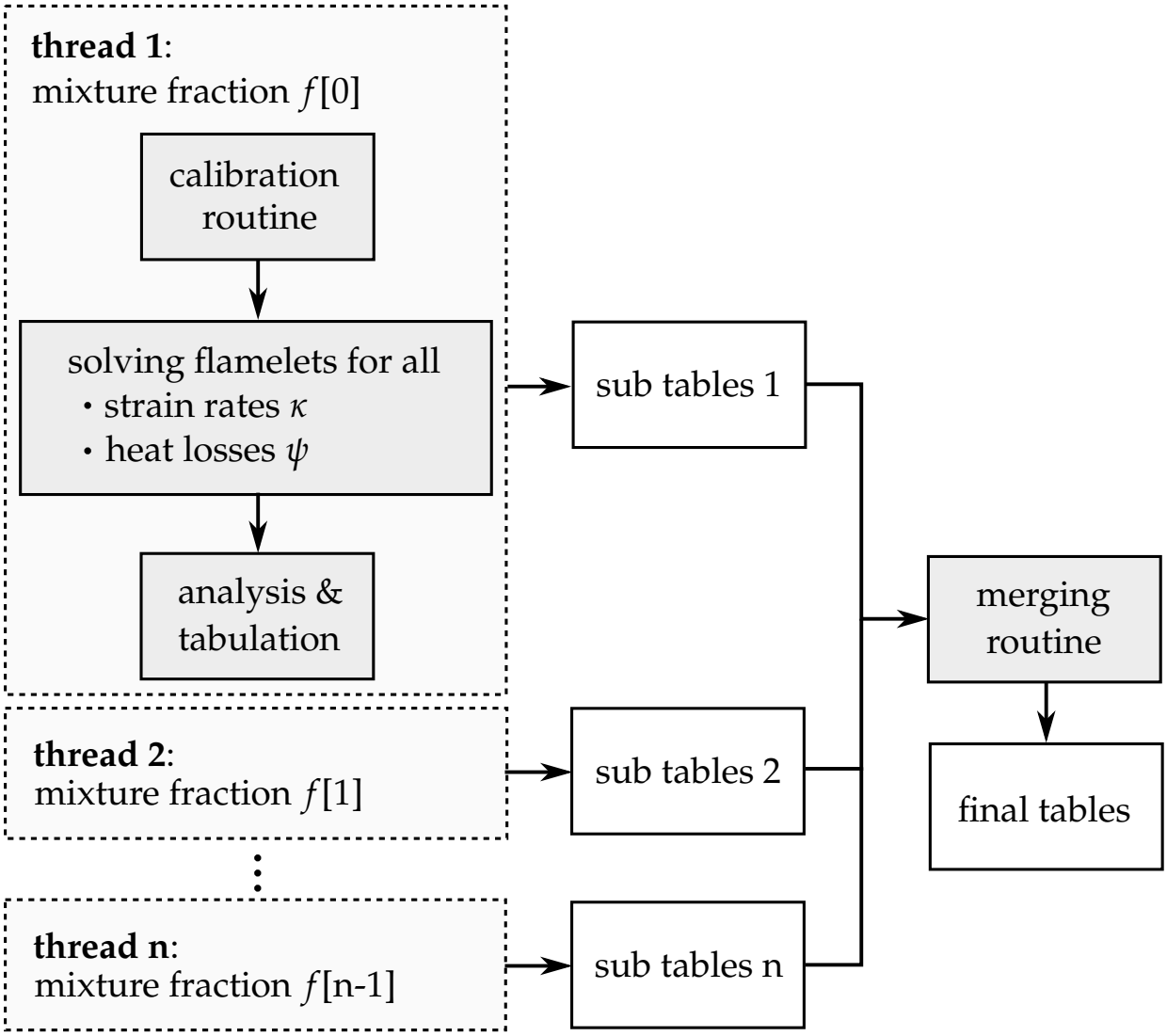

Figure A.2.: The work is divided in multiple threads that can be calculated in parallel.

stance, the number of points that are used to discretize the mixture fraction and the enthalpy defect can be changed. Moreover, a characteristic mixture fraction needs to be specified that defines the mixture fraction at which the exponential factors m (cf. Equation 3.7, 4.5, and 4.7) should be evaluated. Note that it is best practice to specify a characteristic mixture fraction that corresponds to the expected average mixture fraction of the turbulent flame brush. In addition, the maximum values for strain and enthalpy can be changed by setting the corresponding entries. The refine-

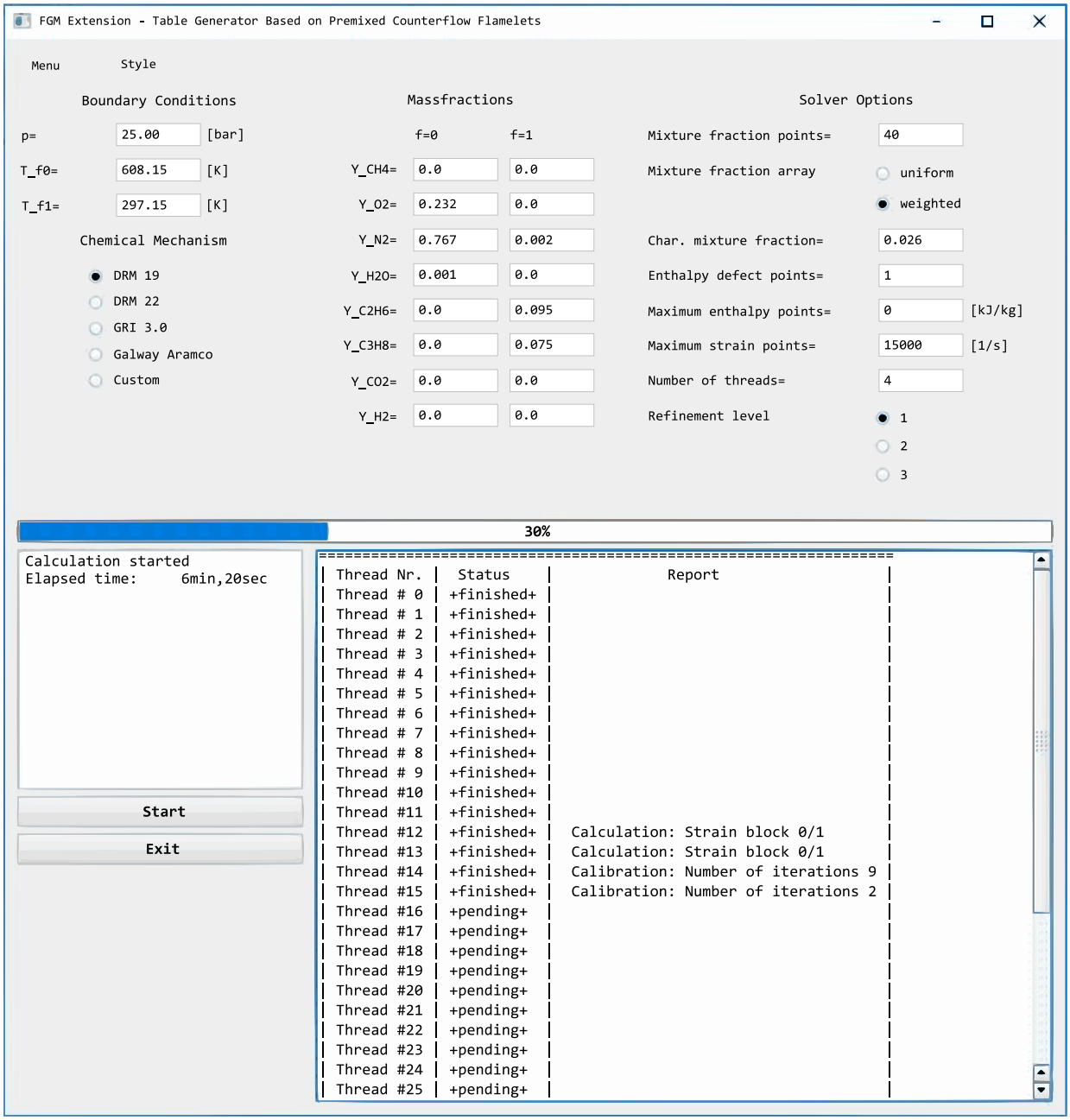

Figure A.3.: Graphical user interface of the Table Generator.

ment level of the flamelet simulation is adjustable by selecting one of the three predefined levels. In order to significantly speed up the calculation, a number of threads should be allocated in order to distribute the work packages. In the lower half of the graphical user interface that is depicted in Figure A.3, different information is provided during run time in order to inform the user of the actual progress. Besides the elapsed time and a progress bar, one can find detailed information for each thread.

A.2. User Defined Function

The C-based User Defined Function can be interpreted as a model layer that is located between the tables and the FLUENT [77] solver. The FLUENT extension consists of three modules that can be described as follows:

1. **Reading module:** This module is called before the solving process starts. It loads the data that is stored in tables into memory. This is necessary in terms of efficiency, as costly file operations during run time are avoided.

2. **Model module:** All models that are proposed in this work are evaluated by executing this module. It is hence necessary to call this part in every cell and for every iteration/time step. The module manipulates the source terms of the reaction progress variable and closes the transport equation for CO according to the proposed modeling strategy.

3. **Interpolation module:** In this module, the discrete in-memory data is interpolated. The interpolation routines are called several times for every cell and for every iteration as a number of interpolated quantities are required to calculate the models. Even though the interpolation routine has the highest computational effort, the overhead is usually negligible.

B Additional Reaction Analysis

The CO model that was proposed in Chapter 4 is based on the analysis of reactions in the late burnout of CO at an equivalence ratio of $\phi = 0.3$. In Figure 4.4, the most relevant reactions for CO are plotted in order to show that the post-flame model can be reduced to Equation r26/27. Moreover, Figure 4.9 shows the five most relevant reaction equations that describe OH to argue that solely r0, r3, and r14 can be used to describe the OH creation source term.

In the following, both studies are repeated for an equivalence ratio of $\phi = 0.5$ in Figure B.1 and B.2.

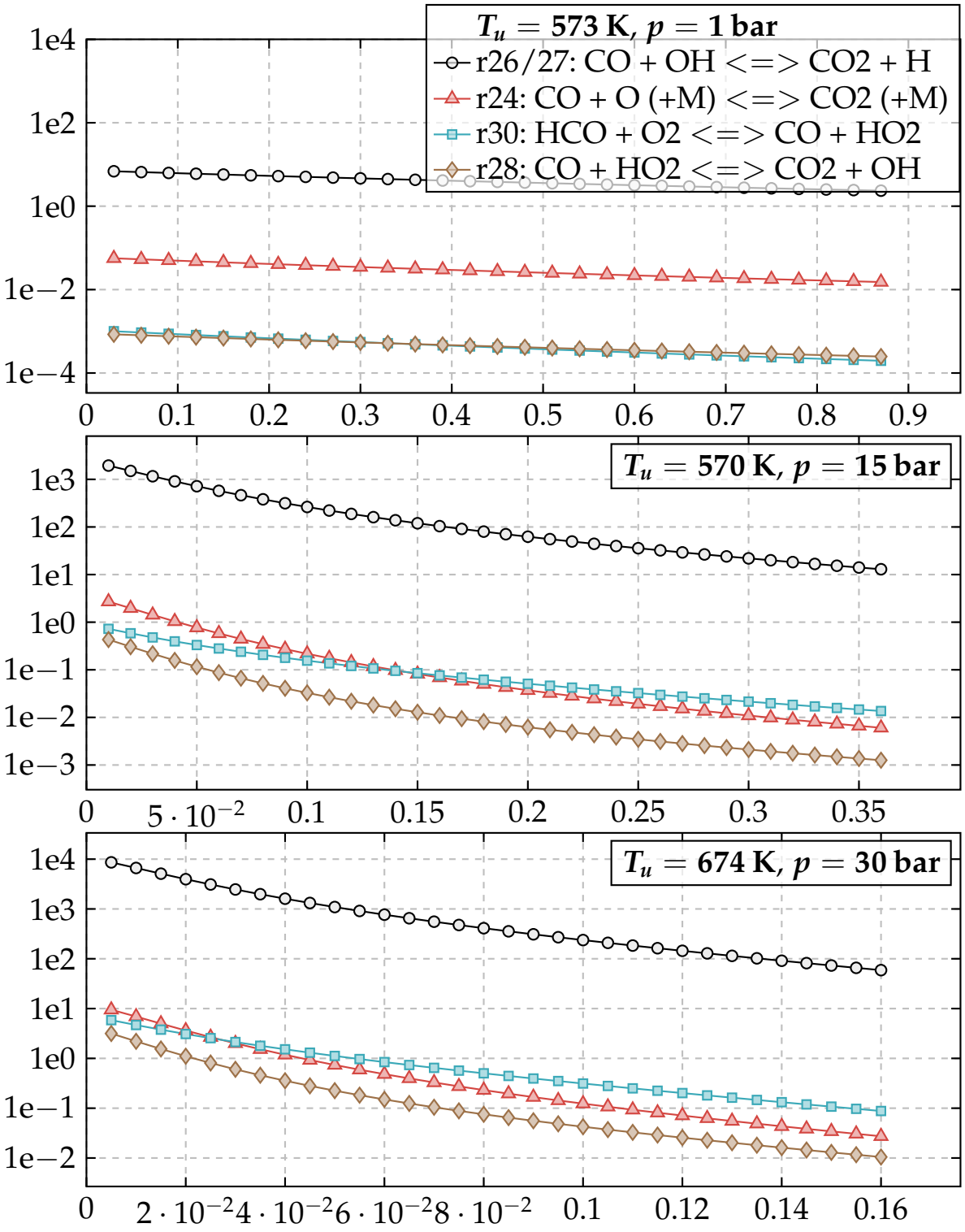

Figure B.1.: Four most relevant CO reactions in the late burnout (constant pressure reactor at $\phi = 0.5$, calculated using GALWAY 1.3 [38] and CANTERA [34]).

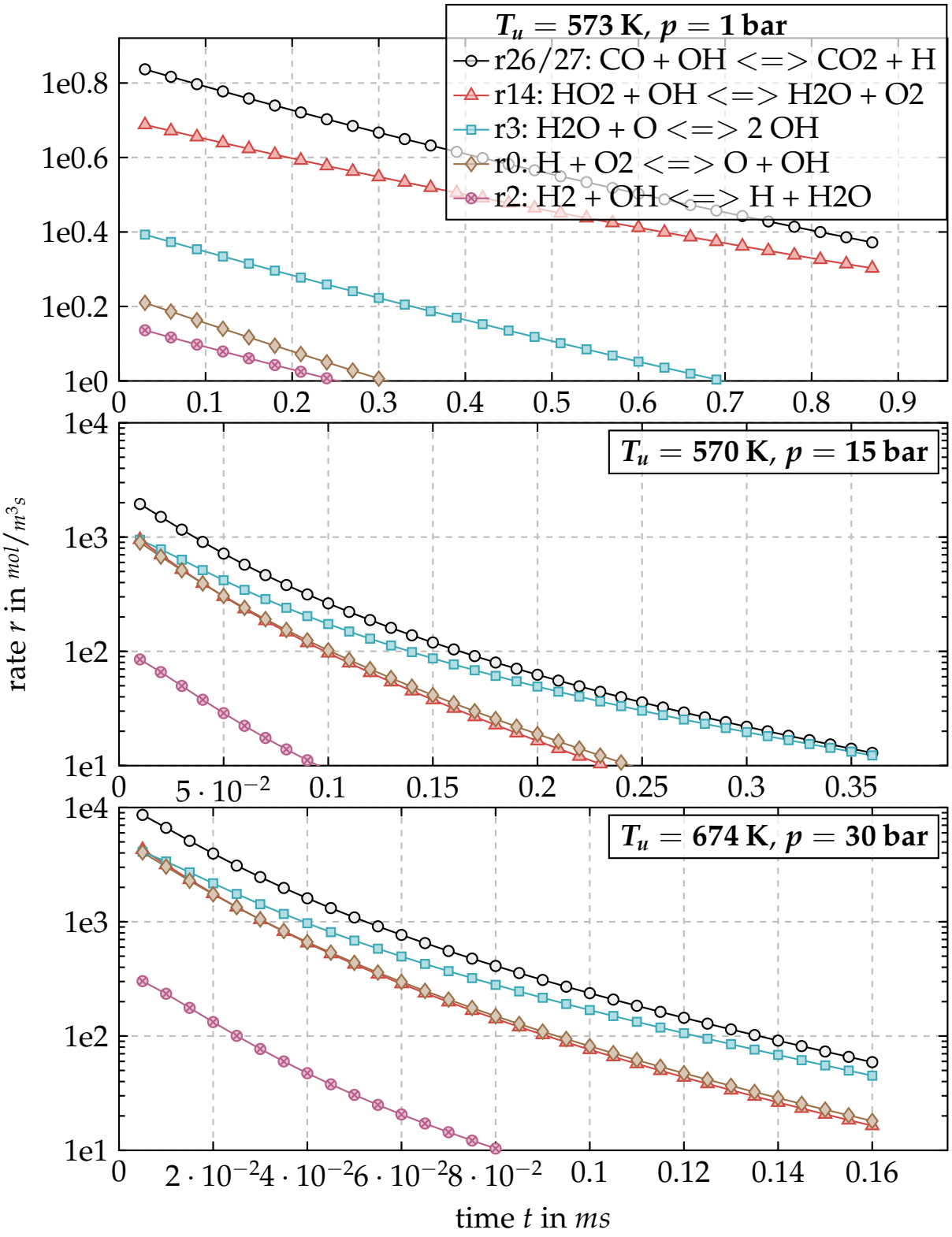

Figure B.2.: Five most relevant OH reactions in the late burnout (constant pressure reactor at $\phi = 0.5$, calculated using GALWAY 1.3 [38] and CANTERA [34]).

Bibliography

[1] Intergovernmental Panel on Climate Change (IPCC), 2013. "Klimaänderung 2013 - Naturwissenschaftliche Grundlagen". pp. 1–28.

[2] International Energy Agency (IEA), 2014. "World Energy Outlook 2014 - Factsheet". pp. 1–5.

[3] International Energy Agency (IEA), 2017. "World Energy Outlook 2017 - Executive Summary". pp. 1–13.

[4] British Petroleum (BP), 2018. "Energy Outlook". pp. 1–125.

[5] United Nations (UN), 2015. "Paris Agreement under the United Nations Framework Conventions on Climate Change". In 21st Conference of the Parties, pp. 1–25.

[6] United Nations (UN), 1998. "Kyoto Protocol to the United Nations Framework Conventions on Climate Change". In International Climate Summit in Kyoto, pp. 1–20.

[7] Wiedermann, A., 2010. "Gasturbinentypen - eine Übersicht". In *Stationäre Gasturbinen*, 2nd ed. Springer-Verlag Berlin Heidelberg, Berlin, ch. 1, pp. 1–11.

[8] Union for the Coordination of Transmission of Electricity (UCTE), 2004. "Operation Handbook - Appendix 1 - Load-Frequency Control and Performance". pp. 1–27.

[9] Sinn, H. W., 2017. "Buffering Volatility: A Study on the Limits of Germany's Energy Revolution". *European Economic Review,* ***99***, pp. 130–150.

[10] BMWi - Bundesministerium für Wirtschaft und Energie, 2016. "Die Energie der Zukunft - Fünfter Monitoring-Bericht zur Energiewende - Berichtsjahr 2015". pp. 1–154.

[11] FNB-Gas - Die Fernleitungsbetreiber, 2016. "Netzentwicklungsplan Gas 2018-2028". pp. 1–204.

[12] Bundesnetzagentur, 2017. "Monitoringbericht 2017". pp. 1–489.

[13] Sattelmayer, T., 2010. "Grundlagen der Verbrennung in stationären Gasturbinen". In *Stationäre Gasturbinen*, 2nd ed. Springer-Verlag Berlin Heidelberg, Berlin, ch. 9, pp. 397–453.

[14] Möning, R., and Waltke, U., 2010. "Verdichter". In *Stationäre Gasturbinen*, 2nd ed. Springer-Verlag Berlin Heidelberg, Berlin, ch. 7, pp. 313–369.

[15] Lefebvre, A. H., and Ballal, D. R., 2010. *Gas Turbine Combustion - Alternative Fuels and Emissions*, 3rd ed. Taylor & Francis Group, Boca Raton.

[16] Steinbach, C., Ulibarri, N., Garay, M., Lübcke, H., Meeuwissen, T., Haffner, K., Aubry, J., and Kodim, D., 2006. "Combustion Optimization for the Alstom GT13E2 Gas Turbine". In Proceedings of the ASME Turbo Expo 2006, GT2006-90943, pp. 1–7.

[17] Guyot, D., Meeuwissen, T., and Rebhan, D., 2012. "Staged Premix EV Combustion in Alstom's GT24 Gas Turbine Engine". In Proceedings of the ASME Turbo Expo 2012, GT2012-70102, pp. 1–9.

[18] Koff, B., 1993. "Aircraft Gas Turbine Emissions Challenge". In International Gas Turbine and Aeroengine Congress and Exposition, pp. 1–5.

[19] Döbbeling, K., Hellat, J., and Koch, H., 2007. "25 Years of BBC/ABB/Alstom Lean Premix Combustion Technologies". *Journal of Engineering for Gas Turbines and Power,* ***129***(2), pp. 1–12.

[20] Hiddemann, M., Hummel, F., and Schmidli, J., 2011. "The Next Generation Alstom GT26 - The Pioneer in Operational Flexibility". In Power-Gen Europe, pp. 1–16.

[21] Güthe, F., Hellat, J., and Flohr, P., 2009. "The Reheat Concept: The Proven Pathway to Ultralow Emissions and High Efficiency and Flexibility". *Journal of Engineering for Gas Turbines and Power,* ***131***(2), pp. 021503–1–7.

[22] Vorontsov, S., Irmisch, S., Karelin, A., and Rocha, M., 2009. "Alstom GT11N2 M Expansion Turbine Design Modification and Operation Experience". In Proceedings of the ASME Turbo Expo 2009, GT2009-59268, pp. 1–9.

[23] Tripod, B., Doebelling, K., Pfeiffer, C., and Heimerl, R., 2012. "Increasing Power Generation Efficiency in Russia and CIS Countries through Further Development of the Alstom GT13E2 Gas Turbine". In Russia Power, pp. 1–24.

[24] Moore, G., 1965. "Cramming More Components Onto Integrated Circuits". *Electronics,* ***38***(8), pp. 1–4.

[25] Goldin, G., Ren, Z., Forkel, H., Lu, L., Tangirala, V., and Karim, H., 2012. "Modeling CO With Flamelet-Generated Manifolds: Part 1 - Flamelet Configuration". In Proceedings of the ASME Turbo Expo 2012, GT2012-69528, pp. 1–11.

[26] Goldin, G., Ren, Z., Forkel, H., Lu, L., Tangirala, V., and Karim, H., 2012. "Modeling CO With Flamelet-Generated Manifolds: Part 2 - Application". In Proceedings of the ASME Turbo Expo 2012, GT2012-69546, pp. 1–8.

[27] Wegner, B., Gruschka, U., Krebs, W., Egorov, Y., Forkel, H., Ferreira, J., and Aschmoneit, K., 2011. "CFD Prediction of Partload CO Emissions Using a Two-Timescale Combustion Model". *Journal of Engineering for Gas Turbines and Power,* ***133***(7), pp. 071502–1–7.

[28] Poinsot, T., and Veynante, D., 2005. *Theoretical and Numerical Combustion*, 2nd ed. Edwards, Philadelphia.

[29] Kuo, K., 1985. *Principles of Combustion*, 2nd ed. John Wiley & Sons, Hoboken.

[30] Williams, F. A., 1985. *Combustion Theory*, 2nd ed. Addison-Wesley series in engineering sciences. Taylor & Francis Group, Boca Raton.

[31] Peters, N., 2004. *Turbulent Combustion*, 1st ed. Cambridge University Press, Cambridge.

[32] Patankar, S., 1980. *Numerical Heat Transfer and Fluid Flow*, 1st ed. McGraw-Hill, New York City.

[33] Chapman, S., Cowling, T. G., and Park, D., 1990. *The Mathematical Theory of Non-Uniform Gases*, 3rd ed. Cambridge University Press, Cambridge.

[34] Goodwin, D., Malaya, N., Moffat, H., and Speth, R., 2015. "Cantera: An Object-Oriented Software Toolkit for Chemical Kinetics, Thermodynamics, and Transport Processes retrieved from code.google.com/p/cantera".

[35] Kazakov, A., and Frenklach, M., 2014. "DRM19 retrieved from http://combustion.berkeley.edu/drm/".

[36] Kazakov, A., and Frenklach, M., 2014. "DRM22 retrieved from http://combustion.berkeley.edu/drm/".

[37] Smith, G. P., Golden, D. M., Frenklach, M., Moriarty, N. W., Eiteneer, B., Goldenberg, M., Bowman, T. C., Hanson, R. K., Song, S., Gardiner, W. C., Lissianski, V. V., and Qin, Z., 2014. "GRI3.0 retrieved from combustion.berkeley.edu/gri-mech/version30".

[38] Metcalfe, W. K., Burke, S. M., Ahmed, S. S., and Curran, H. J., 2013. "A Hierarchical and Comparative Kinetic Modeling Study of C1- C2 Hydrocarbon and Oxygenated Fuels". *International Journal of Chemical Kinetics,* ***45***(10), pp. 638–675.

[39] Keromnes, A., Metcalfe, W. K., Heufer, K. A., Donohoe, N., Das, A. K., Sung, C. J., Herzler, J., Naumann, C., Griebel, P., Mathieu,

O., Krejci, M. C., Petersen, E. L., Pitz, W. J., and Curran, H. J., 2013. "An Experimental and Detailed Chemical Kinetic Modeling Study of Hydrogen and Syngas Mixture Oxidation at Elevated Pressures". *Combustion and Flame,* ***160***(6), pp. 995–1011.

[40] Pope, S., 2000. *Turbulent Flows*, 1st ed. Cambridge University Press, Cambridge.

[41] Richardson, L. F., 1922. *Weather Prediction by Numerical Process*, 1st ed. Cambridge University Press, Cambridge.

[42] Kolmogorov, A. N., 1941. "The Local Structure of Turbulence in Incompressible Viscous Fluid for Very Large Reynolds Numbers". *Proceedings: Mathematical and Physical Sciences,* ***434***(1890), pp. 9–13.

[43] A.Favre, 1992. *Formulation of the Statistical Equations of Turbulent Flows with Variable Density*. Springer-Verlag New York, New York City.

[44] Boussinesq, J., 1877. "Théorie de l'écoulement tourbillant". In Mémoires Présentés par Divers Savans à l'Académie Royaledes Sciences de l'Institut de France 23.

[45] Jones, W. P., and Launder, B. E., 1972. "The Prediction of Laminarization with a Two-Equation Model of Turbulence". *International Journal of Heat and Mass Transfer,* ***15***(2), pp. 301–314.

[46] Veynante, D., Trouvé, A., Bray, K. N. C., and Mantel, T., 1997. "Gradient and Counter-Gradient Scalar Transport in Turbulent Premixed Flames". *Journal of Fluid Mechanics,* ***332***, pp. 263–293.

[47] Borghi, R., 1985. "On the Structure and Morphology of Turbulent Premixed Flames". In *Recent Advances in the Aerospace Sciences*. Plenum Press, New York, ch. 3.7, pp. 117–138.

[48] Spalding, D. B., 1971. "Mixing and Chemical Reaction in Steady Confined Turbulent Flames". *Symposium (International) on Combustion,* ***13***(1), pp. 649–657.

[49] Spalding, D. B., 1977. "Development of the Eddy-Break-up Model of Turbulent Combustion". *Symposium (International) on Combustion,* ***16***(1), pp. 1657–1663.

[50] Magnussen, B., and Hjertager, B., 1977. "On Mathematical Modeling of Turbulent Combustion with Special Emphasis on Soot Formation and Combustion". *Symposium (International) on Combustion,* ***16***(1), pp. 719–729.

[51] Zimont, V., 1979. "Theory of Turbulent Combustion of a Homogenous Fuel Mixture at High Reynolds Numbers". *Combustion Explosion and Shock Waves,* ***15***, pp. 305–311.

[52] Zimont, V., Polifke, W., Bettelini, M., and Weisenstein, W., 1998. "An Efficient Computational Model for Premixed Turbulent Combustion at High Reynolds Numbers Based on a Turbulent Flame Speed Closure". *Journal of Engineering for Gas Turbines and Power,* ***120***(3), pp. 526–532.

[53] van Oijen, J. A., and de Goey, L. P. H., 2000. "Modelling of Premixed Laminar Flames using Flamelet-Generated Manifolds". *Combustion Science and Technology,* ***161***(1), pp. 113–137.

[54] van Oijen, J. A., 2002. "Flamelet-Generated Manifolds : Development and Application to Premixed Laminar Flames". PhD thesis, Technische Universiteit Eindhoven.

[55] Maas, U., and Pope, S., 1992. "Simplifying Chemical Kinetics: Intrinsic Low-Dimensional Manifolds in Composition Space". *Combustion and Flame,* ***88***(3), pp. 239–264.

[56] Ramaekers, W. J. S., Albrecht, B. a., van Oijen, J. A., de Goey, L. P. H., and Eggels, R. G. L. M., 2005. "The Application of Flamelet Generated Manifolds in Modelling of Turbulent Partially-Premixed Flames". In Proceedings of the Fluent Benelux User Group Meeting, pp. 1–16.

[57] Liu, F., Guo, H., Smallwood, G. J., Gülder, Ö. L., and Matovic, M. D., 2002. "A Robust and Accurate Algorithm of the β-PDF Integration

and its Application to Turbulent Methane-Air Diffusion Combustion in a Gas Turbine Combustor Simulator". *International Journal of Thermal Sciences,* ***41***(8), pp. 763–772.

[58] Marosky, A., 2014. "Einfluss der Kühllufteindüsung auf das Betriebsverhalten von Drallbrennern". PhD thesis, Technische Universität München.

[59] Peters, N., 1991. "Length Scales in Laminar and Turbulent Flames". In *Numerical Approaches to Combustion Modeling*, Progress in Astronautics and Aeronautics. American Institute of Aeronautics and Astronautics, ch. 6, pp. 155–182.

[60] van Oijen, J. A., and de Goey, L. P. H., 2002. "Modelling of Premixed Counterflow Flames Using the Flamelet-Generated Manifold Method". *Combustion Theory and Modelling,* ***6***(3), pp. 463–478.

[61] Donini, A., Bastiaans, R. J. M., van Oijen, J. A., and de Goey, L. P. H., 2015. "A Five Dimensional Implementation of the Flamelet Generated Manifolds Technique for Gas Turbine Application". In AIP Conference Proceedings 1648, pp. 030012–1–4.

[62] Donini, A., Bastiaans, R. J. M., van Oijen, J. A., and de Goey, L. P. H., 2015. "The Implementation of Five-Dimensional FGM Combustion Model for the Simulation of Gas Turbine Model Combustor". In Proceedings of the ASME Turbo Expo 2015, GT2015-42037, pp. 1–10.

[63] Tay Wo Chong, L., Komarek, T., Zellhuber, M., Lenz, J., Hirsch, C., and Polifke, W., 2009. "Influence of Strain and Heat loss on Flame Stabilization in a Non-Adiabatic Combustor". In Proceedings of the 4th European Combustion Meeting, pp. 1–6.

[64] Tay Wo Chong, L., Zellhuber, M., Komarek, T., Im, H. G., and Polifke, W., 2016. "Combined Influence of Strain and Heat Loss on Turbulent Premixed Flame Stabilization". *Flow, Turbulence and Combustion,* ***97***(1), pp. 263–294.

[65] Tay Wo Chong, L., Scarpato, A., and Polifke, W., 2017. "LES Combustion Model with Stretch and Heat Loss Effects for Prediction of

Premix Flame Characteristics and Dynamics". In Proceedings of the ASME Turbo Expo 2017, GT2017-63357, pp. 1–12.

[66] Hindmarsh, A., Brown, P., Grant, K., Lee, S., Serban, R., Shumaker, D., and Woodward, C., 2005. "SUNDIALS: Suite of Nonlinear and Differential/Algebraic Equation Solvers". *ACM Transactions on Mathematical Software,* ***31***(3), pp. 363–396.

[67] Poinsot, T., Echekki, T., and Mungal, M. G., 1992. "A Study of the Laminar Flame Tip and Implications for Premixed Turbulent Combustion". *Combustion Science and Technology,* ***81***(1), pp. 45–73.

[68] Fiorina, B., Baron, R., Gicquel, O., Thevenin, D., Carpentier, S., and Darabiha, N., 2003. "Modelling Non-Adiabatic Partially Premixed Flames Using Flame-Prolongation of ILDM". *Combustion Theory and Modelling,* ***7***(3), pp. 449–470.

[69] Wetzel, F., Habisreuther, P., and Zarzalis, N., 2006. "Numerical Investigation of Lean Blow Out of a Model Gas Turbine Combustion Chamber Using a Presumed JPDF-Reaction Model by Taking Heat Loss Processes Into Account". In Proceedings of the ASME Turbo Expo 2006, GT2006-90064, pp. 1–9.

[70] Frank, G., Pohl, S., and Pfitzner, M., 2014. "Heat Transfer in Reacting Cooling Films, Part II: Modelling Near-Wall Effects in Non-Premixed Combustion With Openfoam". In Proceedings of ASME Turbo Expo 2014, GT2014-25215, pp. 1–9.

[71] Veynante, D., Duclos, J. M., and Piana, J., 1994. "Experimental Analysis of Flamelet Models for Premixed Turbulent Combustion". *Symposium (International) on Combustion,* ***25***(1), pp. 1249–1256.

[72] Veynante, D., Piana, J., Duclos, J. M., and Martel, C., 1996. "Experimental Analysis of Flame Surface Density Models for Premixed Turbulent Combustion". *Symposium (International) on Combustion,* ***26***(3), pp. 413–420.

[73] Katragadda, M., Malkeson, S. P., and Chakraborty, N., 2011. "Modelling of the Tangential Strain Rate Term of the Flame Surface Den-

sity Transport Equation in the Context of Reynolds Averaged Navier-Stokes Simulation". *Proceedings of the Combustion Institute,* ***33***(1), pp. 1429–1437.

[74] Meneveau, C., and Poinsot, T., 1991. "Stretching and Quenching of Flamelets in Turbulent Premixed Combustion". *Combustion and Flame,* ***86***(4), pp. 311–332.

[75] Bray, K. N. C., 1990. "Studies of the Turbulent Burning Velocity". *Proceedings of the Royal Society of London A: Mathematical, Physical and Engineering Sciences,* ***431***(1882), pp. 315–335.

[76] Veynante, D., and Vervisch, L., 2002. "Turbulent Combustion Modeling". *Progress in Energy and Combustion Science,* ***28***(3), pp. 193–266.

[77] ANSYS Inc., 2014. "ANSYS Fluent Academic Research, Relase 18.0".

[78] Sangl, J., 2011. "Erhöhung der Brennstoffflexibilität von Vormischbrennern durch Beeinflussung der Wirbeldynamik". PhD thesis, TU-München.

[79] Mayer, C., 2012. "Konzept zur Vorgemischten Verbrennung wasserstoffhaltiger Brennstoffe in Gasturbinen". PhD thesis, TU-München.

[80] Ferziger, J. H., and Peric, M., 2002. *Computational Methods for Fluid Dynamics*, 3rd ed. Springer, Berlin.

[81] ANSYS Inc., 2014. "ANSYS Academic Research, Release 15.0, Theory Guide".

[82] Turns, S. R., 2000. *An Introduction to Combustion - Concepts and Applications*, 2nd ed. McGraw-Hill, Singapore.

[83] Connors, C. S., Barnes, J. C., and Mellor, A. M., 1996. "Semiempirical Predictions and Correlations of CO Emissions from Utility Combustion Turbines". *Journal of Propulsion and Power,* ***12***(5), pp. 926–932.

[84] Joshi, A. V., and Wang, H., 2006. "Master Equation Modeling of Wide Range Temperature and Pressure Dependence of CO + OH to Prod-

ucts". *International Journal of Chemical Kinetics,* ***38***(1), pp. 57–73.

[85] Flagan, R., and Seinfeld, J., 1988. *Fundamentals of Air Pollution Engineering*, 1st ed. Prentice Hall, New Jersey.

[86] Fristrom, R., and Westenberg, A., 1965. *Flame Structure*, 1st ed. McGraw-Hill, New York City.

[87] Howard, J., Williams, G., and Fine, D., 1973. "Kinetics of Carbon Monoxide Oxidation in Postflame Gases". *Symposium (International) on Combustion,* ***14***(1), pp. 975–986.

[88] Dryer, F., and Glassman, I., 1973. "High-temperature oxidation of CO and CH4". *Symposium (International) on Combustion,* ***14***(1), pp. 987–1003.

[89] Lammel, O., Rödiger, T., Stöhr, M., Ax, H., Kutne, P., Severin, M., Griebel, P., and Aigner, M., 2014. "Investigation of Flame Stabilization in a High-Pressure Multi-Jet Combustor by Laser Measurement Techniques". In Proceedings of the ASME Turbo Expo 2014, GT2014-26376, pp. 1–12.

[90] Lammel, O., Severin, M., Ax, H., Lückerath, R., Tomasello, A., Emmi, Y., Noll, B., Aigner, M., and Panek, L., 2017. "High Momentum Jet Flames at Elevated Pressure - A: Experimental and Numerical Investigation for Different Fuels". In Proceedings of the ASME Turbo Expo 2017, GT2017-64615, pp. 1–13.